Politecnico di Torino

ScuDo
Scuola di Dottorato ~ Doctoral School
WHAT YOU ARE, TAKES YOU FAR

Doctoral Dissertation
Doctoral Program in Electrical, Electronics and Communications Engineering
(34^{th}cycle)

Multiphysics Simulation of Electro-optic Modulators Based on Plasmonic Waveguides

By

Mohammadamin Ghomashi

******

Supervisor(s):
Prof. Giovanni Ghione, Supervisor
Prof. Francesco Bertazzi Co-supervisor
Dr. Alberto Tibaldi Co-supervisor

Politecnico di Torino
2022

Declaration

I hereby declare that, the contents and organization of this dissertation constitute my own original work and does not compromise in any way the rights of third parties, including those relating to the security of personal data.

Mohammadamin Ghomashi
2022

* This dissertation is presented in partial fulfillment of the requirements for **Ph.D. degree** in the Graduate School of Politecnico di Torino (ScuDo).

I would like to dedicate this thesis to my beloved wife, Sara, who always supports me.

Acknowledgements

First, I want to acknowledge my supervisor, Prof. Giovanni Ghione, for his constant guidance and patience during these years. Also, I would like to acknowledge Prof. Michele Goano, Prof. Francesco Bertazzi and Dr. Alberto Tibaldi for their great help and advice. Finally, I would like to acknowledge the Fondazione Cassa di Risparmio di Torino, which supported this Ph.D. program through its 2017 program of research scholarships for post-graduate international candidates.

Abstract

Optical modulation is one the most important elements in optical telecommunication systems. Due to the increasing usage of internet and social media at every place in the world, the demand on modulator performance is dramatically increasing. In other words, to meet the need for the telecommunication systems of the future, modulators with higher speeds and bandwidths must be developed, possibily compliant with low-cost silicon-based plaftorms. Several structures and technologies can be used to create an optical modulator. Among these, plasmonic modulator have great potential to be responsive to the needs of future demands. In this study, the modeling of modulators based on plasmonic waveguides is investigated. The two types of Mach-Zehnder and directional coupler modulators are the main focus of the study. The devices contain nonlinear polymers exhibiting the Pockels effect as an active material. This kind of polymer can be grown on silicon photonics chips. The modulator operating wavelengths considered is 1550 nm, which is typical of data center and long-haul telecommunication systems. Chapter 1 covers the review of the modulation of light and nonlinear optical effects. Also, the models of phase modulators and Mach-Zehnder modulators are recalled and the plasmonic modulators are introduced. In chapter 2, the modeling of the plasmonic modulator is addressed both through analytical techniques and by means of commercailly available simulation codes. The introduced analytical methods are very helpful to have a better insight on the intrinsic physics of plasmonic devices. But such simplified models are not enough to simulate and design actual devices. To this aim, more complex methods such as the finite-difference eigenmode method (FDE), the Finite Element Method (FEM) and the Finite-Difference Time-Domain (FDTD) method should be adopted. The FDE and FEM methods are very fast but they can be used in waveguide-level simulations only. For 3D analysis of a full device, FDTD is required, which is very accurate. However, the FDTD method is very computationally demanding in terms of memory and CPU. On the other hand, accurate numerical optimization is an indispensable tool

for device design, and cannot be practically performed, dut to its huge computational intensity, through FTDT. To overcome this limitation, the modal-FDTD method developed in this study can be used. This technique is much faster than FDTD and exhibits the same degree of accuracy. Chapter 3 is dedicated to the modeling of plasmonic Mach-Zehnder modulator and the modal-FDTD is adopted on the reference structure. In Chapter 4, a novel geometry for directional coupler modulator is introduced, and the required simulation and device design are perfomed. Some conclusions are drawn in Chapter 5.

Contents

List of Figures

List of Tables

Chapter 1

Introduction

In this chapter, after reviewing the modulation of light, nonlinear optical effects (which are necessary for electro-optic modulation) are discussed. Also, the phase modulator and Mach-Zehnder modulator are reviewed. At the end of the chapter, the plasmonic modulators are introduced.

1.1 Modulation of light

In the telecommunication systems, information can be transmitted by changing the properties of the light source (intensity, amplitude, phase and frequency); this is called modulation [1]. Two types of modulation are used: field modulation and intensity modulation. In field modulation, the amplitude (or phase, or frequency) of the optical wave is changed according to the information signal (Fig.1.1). In the intensity modulation, the optical power or intensity is varied according to the information signal (Fig.1.2). Since most commercialized fiber communication are designed based on intensity modulation, we only consider here intensity modulation.

The modulation systems can be classified in internal (direct) modulation and external (indirect) modulation. Internal modulation consists in varying the instantaneous bias point of the light source by changing the voltage (or current) applied to it. Conversely, in the external modulation the bias point of the light source is fixed and, for modulation, the optical wave enters another component, called the modulator. Based on the structure and on the physical mechanism exploited, modulators can divided into Electro-optic modulators (EOM) and Electro-absorption modulators

(EAM). Internal modulation is more compact than external modulation, but has lower extinction ratio (defined as the power ratio between the ON state and OFF state), narrower modulation bandwidth and worse chirp (defined as the spurious phase modulation following intensity modulation of light).

External optical modulation systems, are based on the interaction between the electric field and the material optical properties. To achieve this goal, the material of the modulator has nonlinear optical behavior. Hence, the next section is dedicated to a discussion of the main nonlinear optical effects.

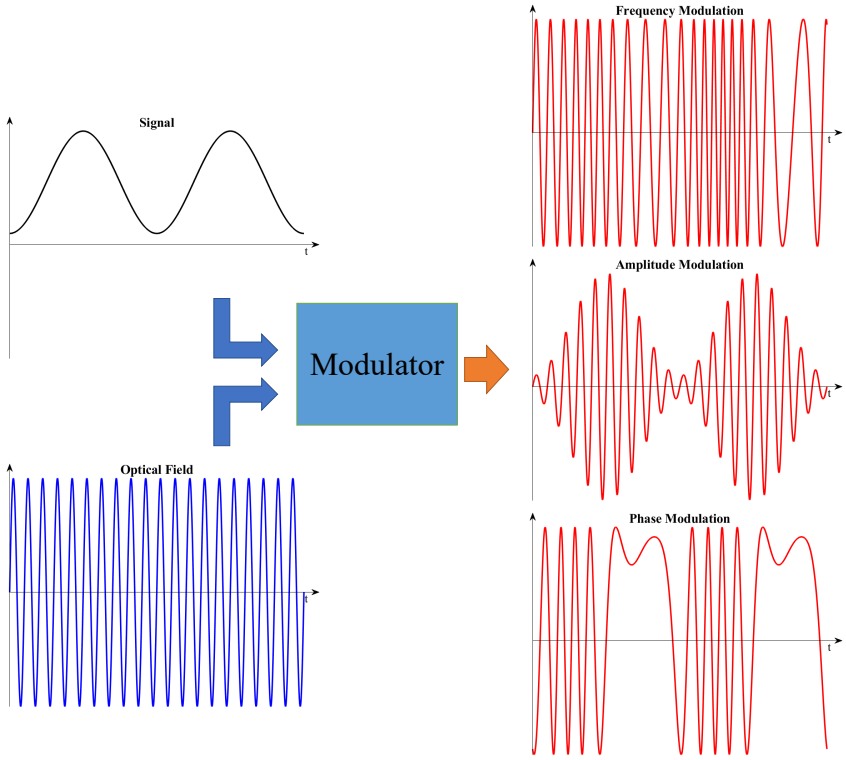

Fig. 1.1 Different types of field modulation[1].

1.2 Nonlinear optical effects

Before the middle of the 20th century, optical components were based on linear materials [1]. In linear material, the refractive index and permittivity are assumed to be independent from the optical intensity. Another consequence of linearity is that the frequency of optical waves remains unchanged when they pass through

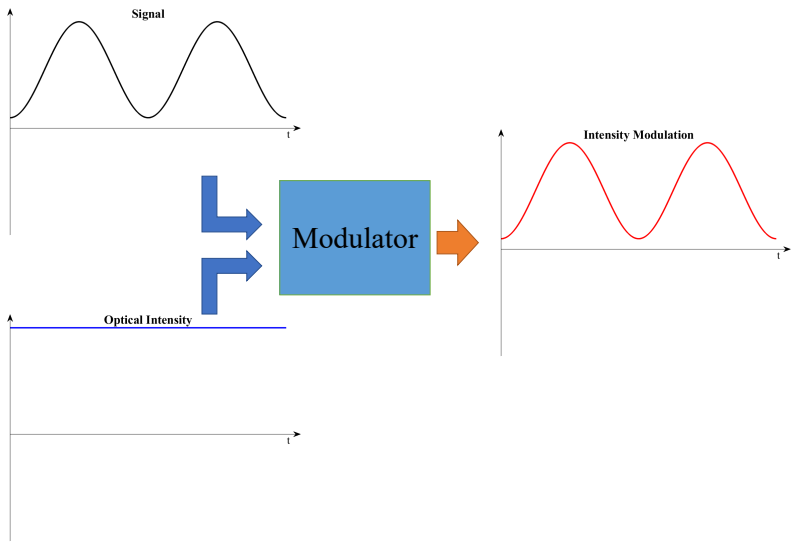

Fig. 1.2 Different types of intensity modulation[1].

a linear material, i.e., no new frequencies are generated, such as harmonics or mixing products. The nonlinear optical effects attracted attention after the successful experiment of second harmonic generation by Peter Franken *et al.* in 1961 [2]. In this experiment, since the nonlinear optical coefficient are very small, a very intense optical wave with wavelength $\lambda = 694.3$ nm was used on the crystalline quartz and a second harmonic was observed at wavelength $\lambda = 347.2$ nm. Four Wave Mixing, Phase Conjugate Mirror, Raman Scattering, Brillouin Scattering are other examples of non-linear optical interactions [1].

In linear, dispersionless materials, the relation between electric field (E) and polarisation (P) satisfies the following equation [1]:

$$P = \varepsilon_0 \chi E \tag{1.1}$$

where ε_0 is the vacuum permittivity and χ is susceptibility of material. However, in nonlinear material this relation becomes [1]:

$$P = \varepsilon_0 \left(\chi^{(1)} + \chi^{(2)} \cdot E + \chi^{(3)} \cdot E \cdot E + ... \right) \cdot E \tag{1.2}$$

where $\chi^{(1)}$ is the first order susceptibility, $\chi^{(2)}$ is the second order susceptibility, and so on. Usually, the value of susceptibilities with order larger than three are very small and can be neglected. The nonlinear relation between P and E in (1.2) can

also be described by a field-dependent susceptibility χ, i.e., by a modulation of the material refractive index or permittivity due to an applied electric field. If the applied field is the superposition of a (weak) optical field and of a (strong) slowly varying (radio-frequency, RF) field, we can approximately assume that the optical refractive index is modulated by the RF field.

In the following subsections, the most commonly used nonlinear effects in modulators are reviewed.

1.2.1 Pockels effect

In some crystals, $\chi^{(2)}$ is much larger than $\chi^{(3)}$, and $\chi^{(3)}$ (and the higher order terms) can be neglected. In these types of crystal, the change in refractive index is proportional to the electric field and the refractive index is obtained as follows [1]:

$$n = n_0 - \frac{1}{2} r n_o^3 E \tag{1.3}$$

where n_0 is the refractive index of the material at zero applied field and r is the Pockels coefficient. Asymmetric crystals such as CdTe, $LiTaO_3$ and $LiNbO_3$ exhibit the Pockels effect and are used in optical modulators.

1.2.2 Kerr effect

The Kerr effect is related to the third-order nonlinear susceptibility $\chi^{(3)}$ [1], that is dominant in crystals (like Si) where $\chi^{(2)} = 0$ for reasons related to the crystal symmetry. The refractive index of the material changes by applying an external electric field like the field square or intensity I. In the materials exhibiting the Kerr effect, the refractive index changes according to the following equation:

$$n = n_0 + n_2 I \tag{1.4}$$

where n_2 is the nonlinear Kerr coefficient and I is the intensity of the input field.

1.2.3 Charge-carrier (plasma) effect

In semiconductors, the optical refractive index depends on the free carrier (electron and/or hole) density, that can be varied by orders of magnitude for example by injection or depletion in a forward- or reverse-biased *pn* junction. The charge-carrier effect (also called the plasma effect) is present in all semiconductors, but it is particularly important in Si, where the Pockels effect vanishes because of the crystal symmetry.

The following formulas represent the variation of refractive index and absorption due to the charge-carrier effect in Si [3]:

$$\Delta n = -(e^2\lambda^2/8\pi^2c^2\varepsilon_0 n_0)[\Delta N_e/m^*_{ce} + \Delta N_h/m^*_{ch}] \tag{1.5}$$

$$\Delta\alpha = (e^3\lambda^2/4\pi^2c^3\varepsilon_0 n_0)[\Delta N_e/m^{*2}_{ce}\mu_e + \Delta N_h/m^{*2}_{ch}\mu_h] \tag{1.6}$$

where e is is the electron charge, λ is the wavelength, ΔN_e is the variation of electron concentration, ΔN_h is the variation of hole concentration, m^*_{ce} is the conduction effective mass of electrons, m^*_{ch} is the conduction effective mass of holes, μ_e is the electron mobility, and μ_h is the hole mobility.

1.2.4 Franz-Keldysh effect

The Franz-Keldysh effect is the variation of absorption coefficient (α) due to the applied electric field. In the presence of an applied field, absorption of a photon with an energy slightly lower than the semiconductor energy gap E_G assist the electron tunneling into the conduction band. Due to the Franz-Keldysh effect, the presence of an external electric field has effect on the electron tunneling and therefore shifts the material absorption edge towards lower energies [4]. Because of the Kramers-Kronig relations connecting the variations of the real and imaginary parts of the material refractive index, the Franz-Keldysh effect also implies a variation of the material permittivity.

1.2.5 Quantum-confined Stark effect

While the Franz-Keldish effect typically occurs in bulk materials, the Quantum-confined Stark effect takes place due to the application of an external field to a

quantum well. The change in the quantum-well profile due to the field implies a variation in the conduction and valence band subband energy levels, that finally leads to a red shift of the absorption edge of the well. Further complexities derive from the presence of exciton states whose absorption response is modulated by the field. Also in this case, the variation of the absorption profile near the absorption edge leads to a corresponding variation of the material permittivity and refractive index [5].

1.2.6 Thermo-optic Effect

The Thermo-optic effect is the dependence of refractive index on the material temperature [6]. The refractive index of material can be expressed by the following equation:

$$n = n_0 + \frac{dn}{dT} \cdot T \tag{1.7}$$

where T is the crystal temperature. Since the variation of the refractive index depends on crystal heating in the presence of an applied heat source, the thermo-optic effect is comparatively slow and cannot be used in high-speed modulators. However, it can be exploited to electrically tune the response of phase modulator sections or of resonant components (like optical rings). By improving material processes in the silicon foundry, it is now possible to integrate heaters on optical components in different ways [7].

1.3 Modulator Parameters

In order to compare modulators, we need to define first their characteristic parameters, often used as figures of merit. Similar to other devices, the modulator behavior includes the static and dynamic response. Here, the most useful static and dynamic parameters are listed.

1.3.1 Transmission

The modulator transmission T is the ratio of the optical output power to the optical input power. In cases where the input and output cross section of the modulator are the same, this is equivalent to the ratio of the output intensity (or power density) to

input intensity. Since the modulator output optical power is determined by the input modulator voltage V_{in}, the transmission is a function of the (DC or slowly varying) input voltage:

$$T(V_{in}) = \frac{P_{out}(V_{in})}{P_{in}} \tag{1.8}$$

1.3.2 ON-state and OFF-state voltages

Ideally, the ON-state voltage V_{ON} is the input voltage at which the input power is completely transmitted to the output ($T = 1$). In practice, some ON-state insertion loss is always present, and therefore V_{ON} is defined as the input voltage that gives the maximum transmission. Conversely, the OFF-state voltage (V_{OFF}) is the input voltage for which the input power is not transmitted to the output, or, in practice, the transmission reaches its minimum value. In Mach-Zehnder modulators the OFF-state voltage is also called V_π since in such modulators the OFF state is reached when a π phase difference occurs between the two modulator arms.

1.3.3 Extinction Ratio

The extinction ratio (ER) is the ratio of the transmission at V_{ON} to the transmission at V_{OFF}. A higher extinction ratio leads to a better light modulation. Usually, the ER is expressed in logarithmic units:

$$ER|_{\text{dB}} = 10\log_{10}\left[\frac{T(V_{ON})}{T(V_{OFF})}\right] \tag{1.9}$$

1.3.4 Insertion loss

The insertion loss (IL) is the modulator loss in the ON state, i.e. the inverse of the ON-state transmission. In logarithmic units we have:

$$IL|_{\text{dB}} = 10\log_{10}\left[\frac{1}{T(V_{ON})}\right] = -\,T(V_{ON})|_{\text{dB}} \tag{1.10}$$

1.3.5 Modulation bandwidth

From the electrical standpoint, the input of an electro-optic (lumped) phase modulator is a capacitor. Assuming sinusoidal excitation, the effective input voltage from a real generator of open-circuit voltage V_0 and generator resistance R_G will experience low-pass filtering described, in the simplest case, by a 3 dB cutoff frequency:

$$f_{3\text{dB}} = \frac{1}{2\pi R_G C_{in}}$$

where C_{in} is the modulator capacitance. This parameter is usually defined as the *modulation bandwidth* of the modulator, often expressed as *speed* in terms of the highest bit rate supported by the modulator. In distributed, traveling-wave modulator structure the speed limitation instead depends on the synchronous coupling of the electrical and optical signals, and on the electrical transmission line losses; this case will not be discussed in detail since, due to their extremely small footprint, plasmonic modulators are always electrically concentrated (lumped) rather than distributed.

1.3.6 Optical bandwidth

The optical bandwidth is defined as the wavelength range on which the modulator operates within specifications. Mach-Zehnder modulators based on $LiNbO_3$ or non-nonlinear polymers have a comparatively large optical bandwidth (of the order of 100 nm); the optical bandwidth is narrower in Mach-Zehnder modulators based on the Quantum confined Stark effect or even worse in resonant ring modulators [8].

1.4 Phase Modulator

An optical phase modulator can be simply implemented by an optical waveguide whose core region is realized with a nonlinear material. Fig.1.3 shows an integrated phase modulator on lithium niobate ($LiNbO_3$), a nonlinear anisotropic material with strong Pockels effect. Optical waveguides can be created in lithium niobate by titanium in-diffusion, that leads to a local increase of refactive index and therefore to the creation of a waveguide with a spot size of the order of 10 μm. By applying a voltage to the electrodes, an electric field of proper direction is created in the

optical waveguide and, due to the material nonlinearity, the refractive index is varied and thus the propagation constant (β) of the fundamental mode; this causes the variation on the phase of optical signal with respect to the zero applied field (voltage) condition. The phase variation $\Delta\phi$ is given by the following relation:

$$\Delta\phi = \Delta\beta L = \frac{2\pi\Delta n_{eff}}{\lambda} L \tag{1.11}$$

where $\Delta\beta$ is the variation of propagation constant, L is the length of waveguide, Δn_{eff} is the variation of the mode effective index and λ is wavelength. In a Si-based photonic integrated platform, phase modulators can be implemented by exploiting the charge-carrier (plasma) effect in a *pn* or *pin* junction integrated in the optical waveguide (Fig.1.4) [9]. The variation of effective refractive index due to the charge-carrier effect is proportional to the reverse voltage applied to the junction. By applying different voltages, the electron and hole density vary due to the increase in junction depletion, thus affecting the effective index (Fig.1.5) [9] Since, the variation of refractive index is small, the length of phase modulator would be around one mm.

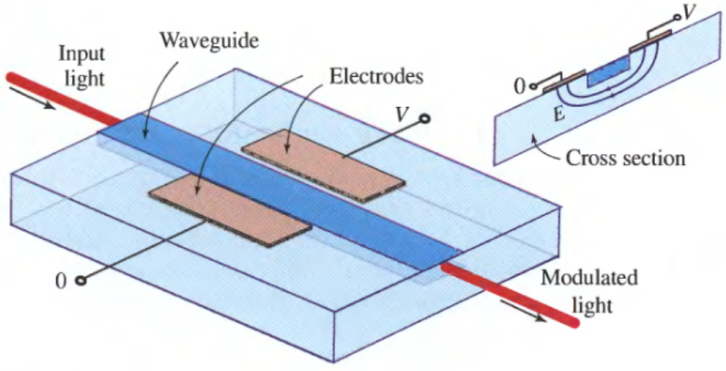

Fig. 1.3 Phase modulator structure[1].

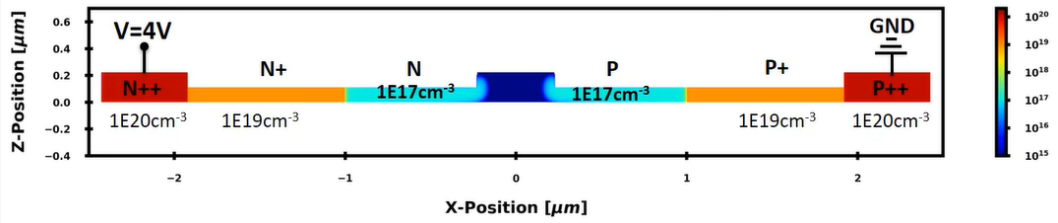

Fig. 1.4 Cross section of a *pin* phase modulator structure[9].

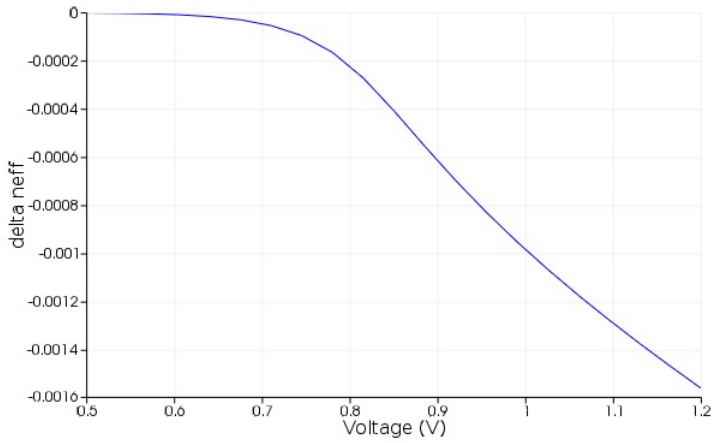

Fig. 1.5 Variation of the mode effective index as a function of the input applied voltage in a *pin* phase modulator structure[9].

1.5 Mach-Zehnder Modulators

The Mach-Zehnder modulator structure, widely used in telecommunication systems, is based on the Mach-Zehnder interferometer (Fig.1.6) [1]. The optical input is split into two arms and in each arm a phase shifter is present. Ideally, if the arms introduce the same phase shift, constructive interference occurs, the output power is maximum and all input power transfers to output. In practice, however, some insertion loss is introduced by the phase shifters, and the maximum output power is lower than the input power. If the phase difference between the arms is $\Delta\phi = \pi$, destructive interference occurs, and the power in the output waveguide is minimum (ideally zero). We express the input intensity (I_i) and electric field (E_i) as:

$$E_i = E_0 e^{i(\omega t - \beta z)} \tag{1.12}$$

$$I_i \propto |E_i|^2. \tag{1.13}$$

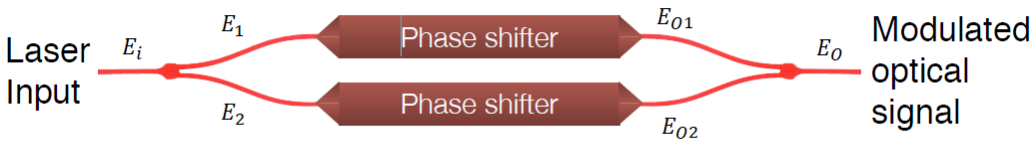

Fig. 1.6 Scheme of the Mach-Zehnder modulator.

The input splitter (assumed as symmetric) divides the input intensity I_i into two equal parts $I_1 = I_2 = 0.5I_i$ so that the input electric fields in the arms (E_1 and E_2) are equal:

$$E_1 = \frac{E_i}{\sqrt{2}} = \frac{E_0 e^{i(\omega t - \beta z)}}{\sqrt{2}} \tag{1.14}$$

$$E_2 = \frac{E_i}{\sqrt{2}} = \frac{E_0 e^{i(\omega t - \beta z)}}{\sqrt{2}}. \tag{1.15}$$

Assuming that the phase shifters have different length (L_1 and L_2, respectively) and diffrent propagation constant (β_1 and β_2, respectively), the electric fields at the phase shifter outputs are:

$$E_{o1} = E_1 e^{-i\beta_1 L_1} = \frac{E_i e^{-i\beta_1 L_1}}{\sqrt{2}} \tag{1.16}$$

$$E_{o2} = E_2 e^{-i\beta_1 L_1} = \frac{E_i e^{-i\beta_2 L_2}}{\sqrt{2}} \tag{1.17}$$

The field E_{o1} and E_{o2} are combined at the end of modulator by the output combiner, and the output intensity (I_o) and electric field (E_o) will be:

$$E_o = \frac{E_{o1} + E_{o2}}{\sqrt{2}} = \frac{E_i}{2}\left(e^{-i\beta_1 L_1} + e^{-i\beta_2 L_2}\right) \tag{1.18}$$

$$I_o = \frac{I_i}{4}\left|e^{-i\beta_1 L_1} + e^{-i\beta_2 L_2}\right|^2 \tag{1.19}$$

If the arms have the same length ($L_1 = L_2$), the I_o can be simplified to the following equation:

$$T = \frac{I_o}{I_i} = \frac{1}{2}\left[1 + \cos(\Delta\beta L)\right] = \frac{1}{2}\left[1 + \cos(\Delta\phi)\right] \tag{1.20}$$

where:

$$\Delta\beta = \beta_1 - \beta_2 \tag{1.21}$$

T is transmission of modulator and $\Delta\phi$ is the phase difference between arms. The Mach-Zehnder modulator can be fabricated by exploiting a *pin* phase shifter in the silicon foundry (Fig.1.7) [10]. The implementation shown has 40 Gbit/s speed and 6 dB insertion loss. The transmission of modulator is presented in Fig.1.8 for two different arm lengths.

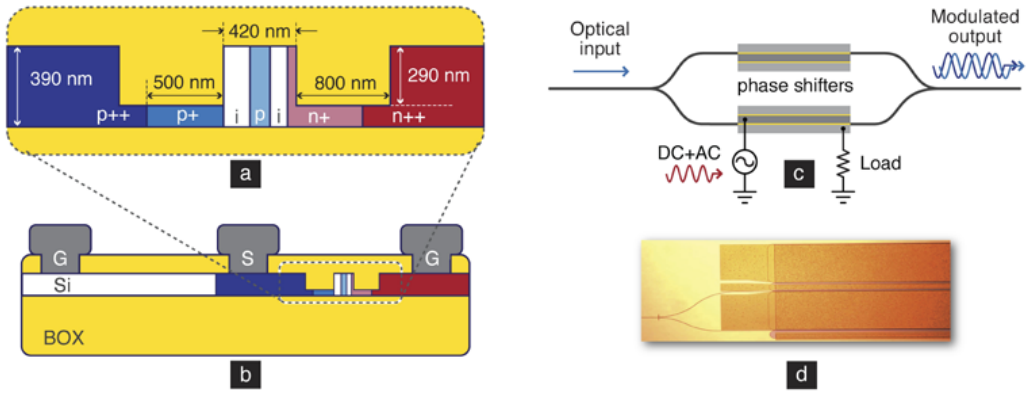

Fig. 1.7 Mach-Zehnder Si-based *pin* modulator structure[10].

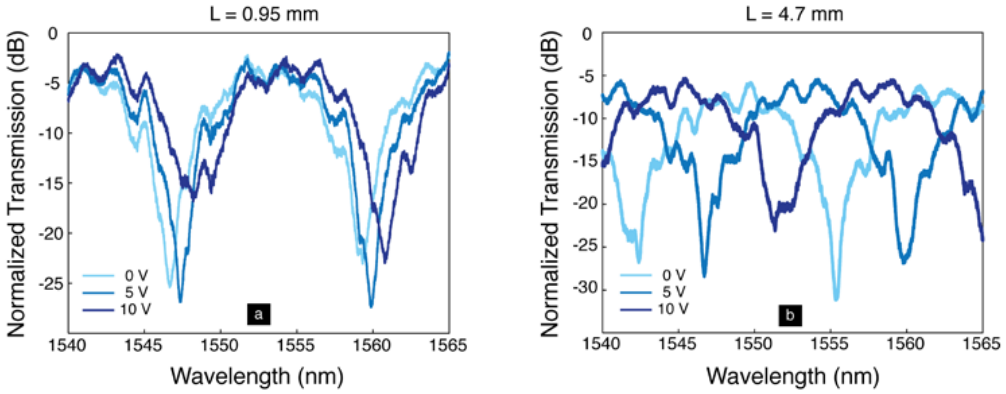

Fig. 1.8 Mach-Zehnder transmission versus wavelength[10].

1.6 Plasmonic Phase and Mach-Zehnder Modulators

Plasmonic modulators operate by exciting a plasmonic mode that is supported by at least one interface between a metal and a dielectric. In comparison with conventional modulators, they work at higher speed (i.e., with a wider modulation bandwidth) due to their extremely compact (a few μm^2) footprint. Thanks to their technological features and small size, plasmonic modulators can be integrated with electronic CMOS circuits in the same chip, a feature that is promising for next generation of integrated photonic platforms based on Si. Disadvantages of the plasmonic modulators are the comparatively high insertion loss and the need to include in the modulator transitions between photonic and plasmonic waveguides. A plasmonic phase modulator can be fabricated as a plasmonic slot by placing a non-linear polymer (DLD-164 in this case [11]) layer between two gold layers, see Fig.1.9

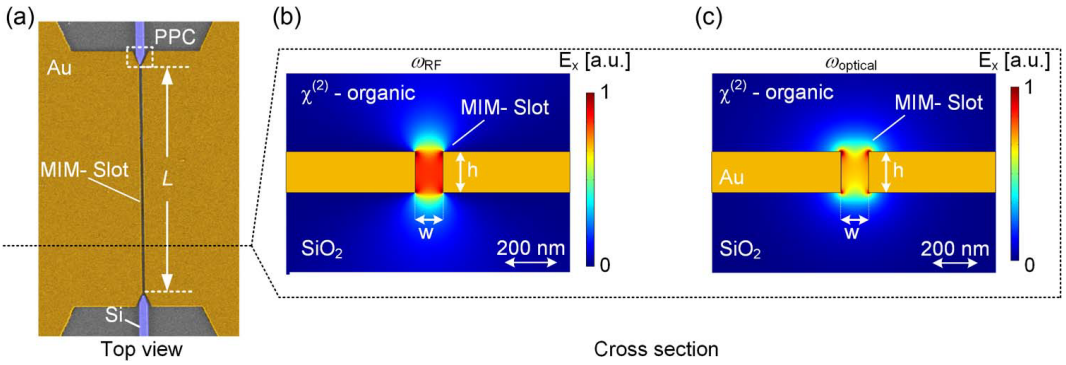

Fig. 1.9 Plasmonic phase modulator: (a) SEM image (b) Simulated E_x at RF (ω_{RF}) (c) simulated E_x at optical frequency ($\omega_{optical}$)[12].

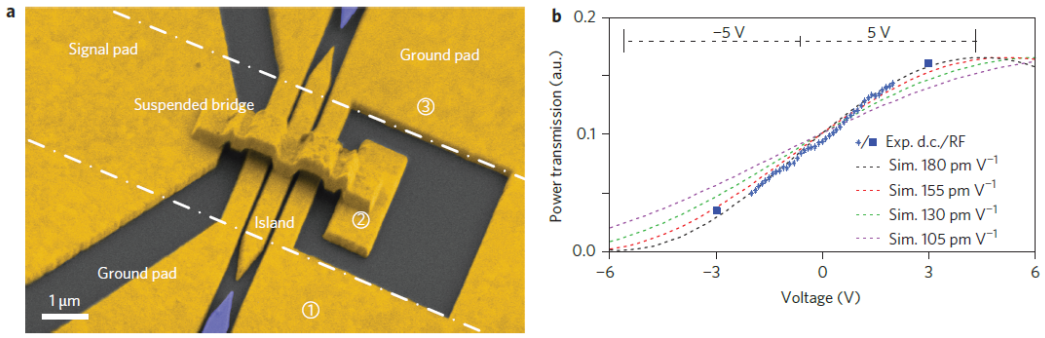

Fig. 1.10 Plasmonic Mach-Zehnder modulator: (a) SEM image (b) Transmission versus applied voltage[12].

[12]. When a voltage is applied to the electrodes, a strong electric field is induced in the nanometer-scale slot, thus changing the refractive index of the non-linear polymer and affecting the phase of the output. This geometry is very compact, and the length of modulator (L) is in the order of few μm. The width (W) and height (H) of slot are in the range of 30 nm-200 nm and 90 nm-600 nm, respectively. This phase modulator design can be exploited in plasmonic Mach-Zehnder modulators, where two slots are excited by a photonic-plasmonic splitter and converter, and the output slot fields are combined and converted to a photonic mode by the output combiner/converter (Fig.1.10). This modulator has an electro-optic bandwidth of about 70 GHz with a length of 10 μm. Low energy consumption of 25 fJ per bit, related to the small footprint and reduced capacitance, is another advantage of this modulator. The insertion loss due to plasmonic and photonic-plasmonic conversion losses is as high as 8 dB.

Chapter 2

Plasmonic Modulators Modeling

The chapter is focused on modeling method and tools of plasmonic structures, presented in [13, 9]. In our study, plasmonic modulators rely on surface plasmon polaritons. Surface plasmon polaritons are electromagnetic propagation modes which exist at the interface between a metal and a dielectric.

2.1 Analytical Method

In general, the interaction of metal and electromagnetic fields can be investigated by a classical framework based on Maxwell's equations. To analyze the behavior of surface plasmon polaritons, the well-known *wave equation* can be used:

$$\nabla^2 E - \frac{\varepsilon}{c^2}\frac{\partial^2 E}{\partial t^2} = 0 \tag{2.1}$$

where ε is the permittivity of the material, c is the speed of light. In practice, for each region with constant ε this equation is solved, and by imposing continuity conditions on the regions' boundaries the final solution is computed. Consider E as a separable function of space (r) and time (t) with the following form:

$$E(r,t) = E(r)e^{-i\omega t} \tag{2.2}$$

By substituting equation (2.2) into (2.2), equation (2.3) is obtained, called the *Helmholtz equation*:

$$\nabla^2 E + k_0^2 \varepsilon E = 0, \qquad k_0 = \frac{\omega}{c} \tag{2.3}$$

If the geometry considered, described in a Cartesian coordinate system, is similar to Fig. 2.1 [13], the permittivity $\varepsilon = \varepsilon(z)$ is a function of z and the electric field propagates waves along the x direction, i.e., if we assume $E(x,y,z) = E(z)e^{i\beta x}$, equation (2.3) is equivalent to two sets of self-consistent equations according to the electric field polarization (TM or TE modes). In the TM mode, the magnetic field in y direction (H_y) is the only component, and the electric field in the x and z directions (E_x and E_z, respectively) is computed from H_y. Similarly, in the TE mode, the electric field in y direction (E_y) is the only component and the magnetic field in the x and z directions (H_x and H_z, respectively) is computed from E_y.

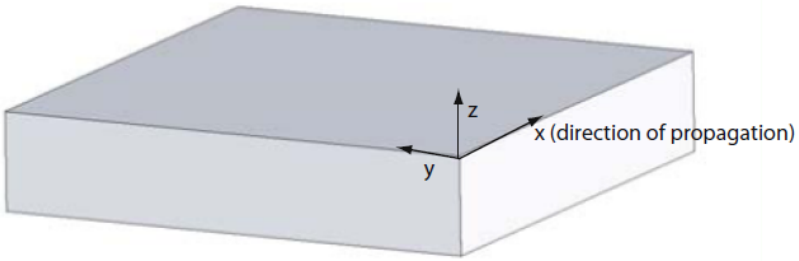

Fig. 2.1 Geometry of the considered structure[13].

For TM propagation, the following set of equations apply:

$$\frac{\partial^2 H_y}{\partial z^2} + (k_0^2 \varepsilon - \beta^2) H_y = 0 \tag{2.4}$$

$$E_x = -i \frac{1}{\omega \varepsilon_0 \varepsilon} \frac{\partial H_y}{\partial z} \tag{2.5}$$

$$E_z = -\frac{\beta}{\omega \varepsilon_0 \varepsilon} H_y \tag{2.6}$$

For TE propagation, the following set of equations results:

$$\frac{\partial^2 E_y}{\partial z^2} + (k_0^2 \varepsilon - \beta^2) E_y = 0 \tag{2.7}$$

$$H_x = i \frac{1}{\omega \mu_0} \frac{\partial E_y}{\partial z} \tag{2.8}$$

$$H_z = \frac{\beta}{\omega \mu_0} E_y \tag{2.9}$$

2.1.1 Plasmonic Single Interface

In this section, the electromagnetic wave is investigated on a single metal-dielectric interface (Fig. 2.2) [13]. The permittivities of metal and dielectric are $\varepsilon_1(\omega)$ and $\varepsilon_2(\omega)$, respectively. The surface plasmon polaritons are generated when the $\mathrm{Re}\,[\varepsilon_1(\omega)] < 0$. In this case, however, the TE set of equations has no non-zero solution, which implies that surface plasmon polaritons are not excited for the TE polarization. Conversely, TM set of equations for a plasmonic single interface yields solutions under the form of an electromagnetic wave with evanescent decay in the perpendicular z direction. An analytical expression of the field components for the TM wave in the metal and dielectric regions is given below:

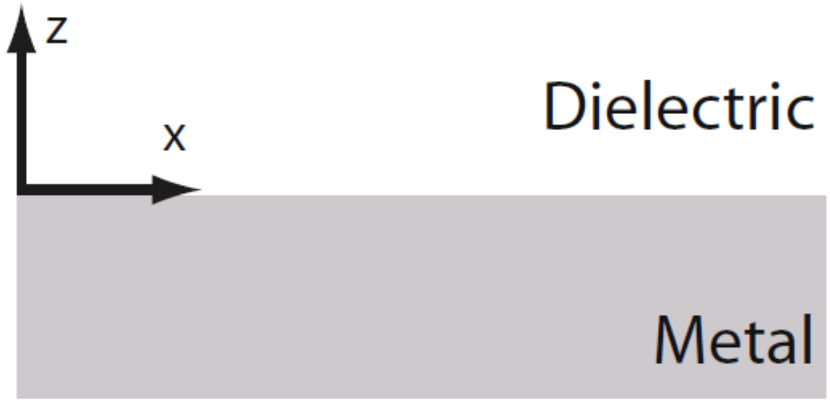

Fig. 2.2 Geometry of single interface between metal and dielectric [13].

- TM wave for $z < 0$ (i.e., in the metal):

$$H_y = Ae^{i\beta x}e^{k_1 z} \tag{2.10}$$

$$E_x = -iA\frac{1}{\omega\varepsilon_0\varepsilon_1}k_1 e^{i\beta x}e^{k_1 z} \tag{2.11}$$

$$E_z = -A\frac{\beta}{\omega\varepsilon_0\varepsilon_1}e^{i\beta x}e^{k_1 z} \tag{2.12}$$

- TM wave for $z > 0$ (i.e., in the dielectric):

$$H_y = Ae^{i\beta x}e^{-k_2 z} \tag{2.13}$$

$$E_x = iA\frac{1}{\omega\varepsilon_0\varepsilon_2}k_2 e^{i\beta x}e^{-k_2 z} \tag{2.14}$$

$$E_z = -A\frac{\beta}{\omega\varepsilon_0\varepsilon_2}e^{i\beta x}e^{-k_2 z} \tag{2.15}$$

In the above equations, A is a constant, k_1 and k_2 are wave vectors having the following relationship with the propagation constant β:

$$k_1^2 = \beta^2 - k_0^2\varepsilon_1 \tag{2.16}$$

$$k_2^2 = \beta^2 - k_0^2\varepsilon_2 \tag{2.17}$$

$$\beta = k_0\sqrt{\frac{\varepsilon_1\varepsilon_2}{\varepsilon_1+\varepsilon_2}} \tag{2.18}$$

For instance, the H_y component for a gold-Silicon dioxide (SiO_2) interface is illustrated in Fig. 2.3. The H_y component decays faster in the metal than in the dielectric since the wave vector is larger.

Suppose now that $\varepsilon_1(\omega) = \varepsilon_m(\omega)$ has negligible imaginary part and $\varepsilon_2(\omega) = \varepsilon_d$ is constant over the frequency range considered. According to the excitation frequency, three propagation regimes exist :

- if $\varepsilon_m > 0 \rightarrow \beta$ is real, but the modes are radiative rather than plasmonic;
- if $\varepsilon_m < 0, \varepsilon_m - \varepsilon_d > 0, \rightarrow \beta$ is imaginary and mode is under cut off;
- if $\varepsilon_m < 0, \varepsilon_m + \varepsilon_d < 0, \rightarrow \beta$ is real and the mode is plasmonic.

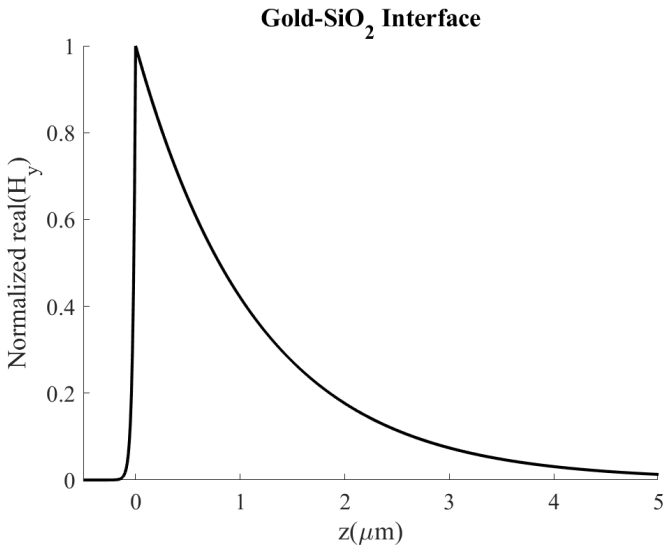

Fig. 2.3 Real part of normalized H_Y for gold-SiO_2 interface at wavelength $\lambda = 1550$ nm.

The transition point form real β (plasmonic mode) to imaginary β is very important. The angular frequency corresponding to the transition point is called the *surface plasmon (angular) frequency* ω_{sp}. The plasmonic mode exists only for $\omega < \omega_{sp}$. In order to find an expression for ω_{sp} and gain a better insight on it, the Drude model is exploited for the metal permittivity:

$$\varepsilon_m(\omega) = 1 - \frac{\omega_p^2}{\omega^2} \tag{2.19}$$

Where ω_p is the plasma frequency, related to the characteristic of the metal. Inserting equation (2.19) into equation (2.18), we obtain:

$$\beta = k_0 \sqrt{\frac{(\omega^2 - \omega_p^2)\varepsilon_d}{(1+\varepsilon_d)\omega^2 - \omega_p^2}}. \tag{2.20}$$

At low frequency ($\omega \to 0$), ε_m is a huge negative number, $\varepsilon_m + \varepsilon_d < 0$; thus, β is real and almost equal to $k_0\sqrt{\varepsilon_d}$. By increasing ω, $|\varepsilon_m|$ decreases and β increases.

At the surface plasmon frequency ($\omega \to \omega_{sp}$), $\varepsilon_m \approx -\varepsilon_d$ and β ($\varepsilon_m + \varepsilon_d \to 0$) tends to infinity. By using equation (2.19) and putting $\omega = \omega_{sp}$ and $\varepsilon_m = -\varepsilon_d$, the surface plasmon frequency ω_{sp} can be computed:

$$\omega_{sp} = \frac{\omega_p}{\sqrt{1+\varepsilon_d}} \tag{2.21}$$

2.1.2 Plasmonic Multilayer System

The plasmonic multilayer system is a combination of dielectric and metal layers which contains more than one plasmonic (metal-dielectric) interfaces. If the plasmonic interfaces are close enough, they affect each other and cause coupling from one plasmonic interface to the adjacent interface. For simplicity, the plasmonic multilayer is considered as a three-layer structure in two cases:

- MIM: a dielectric (insulator) layer is placed between two metal layers.;
- IMI: a metal layer is placed between two dielectric (insulator) layers.

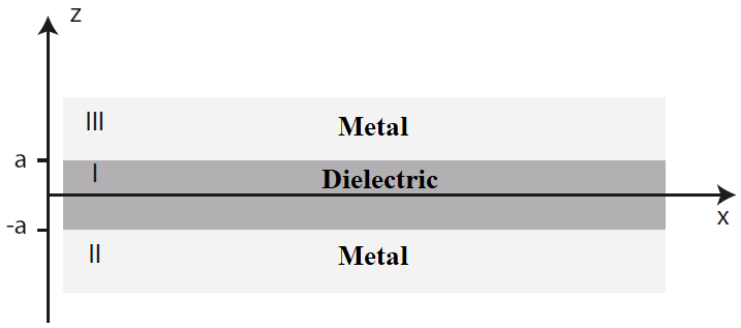

Fig. 2.4 Geometry of MIM system[13].

Since the MIM system is more compatible than the IMI system with the desired plasmonic modulators, the TM set equations is solved for the MIM system only (Fig. 2.4)[13]. In the metals, the solution is similar to single interface and the fields decay exponentially. In the dielectric middle layer, solutions can be an even or odd mode (even mode means even H_y and E_z and odd E_x; odd mode means odd H_y and E_z and even E_x). For the even mode we have:

$$H_y = \begin{cases} Ae^{i\beta_e x}e^{k_1 z}, & z < -a \\ Be^{i\beta_e x}\cosh(k_2 z), & -a < z < a \\ Ae^{i\beta_e x}e^{-k_1 z}, & z > a \end{cases} \tag{2.22}$$

$$E_x = \begin{cases} -iA\frac{1}{\omega\varepsilon_0\varepsilon_1}k_1 e^{i\beta_e x}e^{k_1 z}, & z < -a \\ -iB\frac{1}{\omega\varepsilon_0\varepsilon_1}k_2 e^{i\beta_e x}\sinh(k_2 z), & -a < z < a \\ iA\frac{1}{\omega\varepsilon_0\varepsilon_1}k_1 e^{i\beta_e x}e^{-k_1 z}, & z > a \end{cases} \tag{2.23}$$

$$E_z = \begin{cases} -A\frac{\beta_e}{\omega\varepsilon_0\varepsilon_1}e^{i\beta_e x}e^{k_1 z}, & z < -a \\ -B\frac{\beta_e}{\omega\varepsilon_0\varepsilon_1}e^{i\beta_e x}\cosh(k_2 z), & -a < z < a \\ -A\frac{\beta_e}{\omega\varepsilon_0\varepsilon_1}e^{i\beta_e x}e^{-k_1 z}, & z > a \end{cases} \tag{2.24}$$

For the the odd mode:

$$H_y = \begin{cases} Ae^{i\beta_o x}e^{k_1 z}, & z < -a \\ Be^{i\beta_o x}\sinh(k_2 z), & -a < z < a \\ -Ae^{i\beta_o x}e^{-k_1 z}, & z > a \end{cases} \tag{2.25}$$

$$E_x = \begin{cases} -iA\frac{1}{\omega\varepsilon_0\varepsilon_1}k_1 e^{i\beta_o x}e^{k_1 z}, & z < -a \\ iB\frac{1}{\omega\varepsilon_0\varepsilon_1}k_2 e^{i\beta_o x}\cosh(k_2 z), & -a < z < a \\ -iA\frac{1}{\omega\varepsilon_0\varepsilon_1}k_1 e^{i\beta_o x}e^{-k_1 z}, & z > a \end{cases} \tag{2.26}$$

$$E_z = \begin{cases} -A\frac{\beta_o}{\omega\varepsilon_0\varepsilon_1}e^{i\beta_o x}e^{k_1 z}, & z < -a \\ -B\frac{\beta_o}{\omega\varepsilon_0\varepsilon_1}e^{i\beta_o x}\sinh(k_2 z), & -a < z < a \\ A\frac{\beta_o}{\omega\varepsilon_0\varepsilon_1}e^{i\beta_o x}e^{-k_1 z}, & z > a \end{cases} \tag{2.27}$$

For each mode, k_1 and k_2 are the same as in equation (2.16) and (2.17). The β_e and β_o are the propagation constants for the even and odd modes, respectively, and obey to the following relation:

$$\tanh\left(a\sqrt{\beta_e^2 - k_0^2\varepsilon_d}\right) = -\frac{\varepsilon_m\sqrt{\beta_e^2 - k_0^2\varepsilon_d}}{\varepsilon_d\sqrt{\beta_e^2 - k_0^2\varepsilon_m}} \tag{2.28}$$

$$\tanh\left(a\sqrt{\beta_o^2 - k_0^2\varepsilon_d}\right) = -\frac{\varepsilon_d\sqrt{\beta_o^2 - k_0^2\varepsilon_m}}{\varepsilon_m\sqrt{\beta_o^2 - k_0^2\varepsilon_d}}. \tag{2.29}$$

2.1.3 Coupled mode theory

The coupled mode theory (CMT) is based on a perturbative solution of the Maxwell's equations [14]. In our study, CMT is used for the analysis of a directional coupler consisting of two or more coupled waveguides. According to the CMT, for a two-waveguide directional coupler, the electric field can be expressed in terms of the following equations [15]:

$$E(x,y,z) = A_1(z)E_1(x)e^{i(wt-\beta_1 z)} + A_2(z)E_2(x)e^{i(wt-\beta_2 z)} \tag{2.30}$$

$$\frac{dA_1(z)}{dz} = -iK_{11}A_1(z) - iK_{12}A_2(z)e^{i(\beta_1-\beta_2)} \tag{2.31}$$

$$\frac{dA_2(z)}{dz} = -iK_{21}A_1(z)e^{i(\beta_2-\beta_1)} - iK_{22}A_2(z) \tag{2.32}$$

$$K_{11} = \frac{1}{4}\omega\varepsilon_0\int\int \varepsilon_1^*(x)\Delta n_2^2(x,y)\varepsilon_1(x)dxdy \tag{2.33}$$

$$K_{12} = \frac{1}{4}\omega\varepsilon_0\int\int \varepsilon_1^*(x)\Delta n_1^2(x,y)\varepsilon_2(x)dxdy \tag{2.34}$$

$$K_{21} = \frac{1}{4}\omega\varepsilon_0\int\int \varepsilon_2^*(x)\Delta n_2^2(x,y)\varepsilon_1(x)dxdy \tag{2.35}$$

$$K_{22} = \frac{1}{4}\omega\varepsilon_0\int\int \varepsilon_2^*(x)\Delta n_1^2(x,y)\varepsilon_2(x)dxdy \tag{2.36}$$

where $E_1(x)e^{i(wt-\beta_1 z)}$ and $E_2(x)e^{i(wt-\beta_2 z)}$ are individual propagating waves of each waveguide, assumed as uncoupled from the other one.

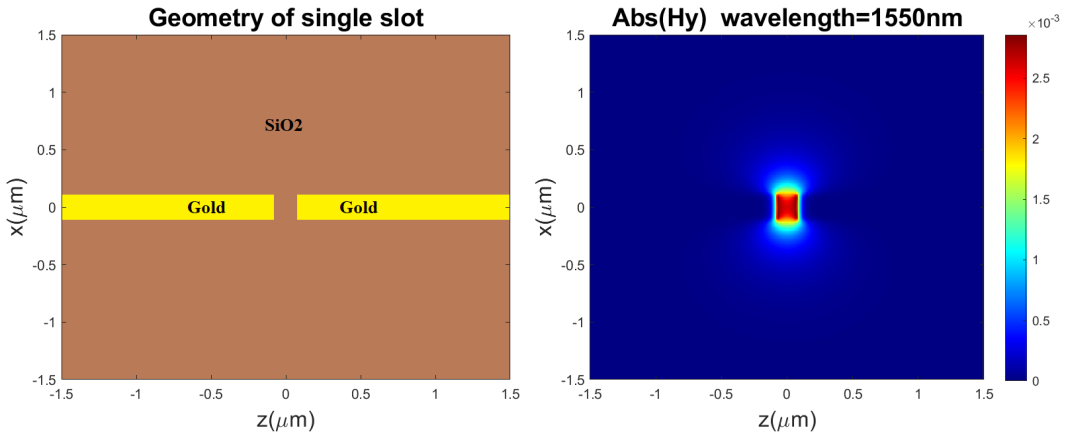

Fig. 2.5 Mode profile of FDE example.

2.2 Finite-Difference Eigenmode Method

The Finite-Difference Eigenmode (FDE) method implemented in commercial software [9] is used to analyze the propagation characteristics of the single plasmonic slot and of plasmonic coupled-slot directional coupler. The FDE is solves Maxwell's equations on a defined area (usually, the cross-section of a waveguide) and than computes the spatial profile and frequency dependence of the modes. Also, it provides a complex refractive index related to the each mode supported by the geometry, which can be easily translated into propagating constants. The method is quite fast, but it is not sufficient to derive realistic estimates of the main parameters of a modulator, such as the extinction ratio and the insertion loss. Fig. 2.5 presents the mode profile in a single plasmonic slot, simulated by the FDE method at $\lambda = 1550$ nm. Also, the propagation constant of the structure are computed (Fig. 2.6). The FDE method is also useful for analysing directional couplers. The first step consists in considering only one of the waveguides and then, by FDE, the mode profile is calculated. After that, modes existing in the presence of both wavegudes is computed, and by decomposing the mode profile into them, the propagation constant of each supported mode is estimated.

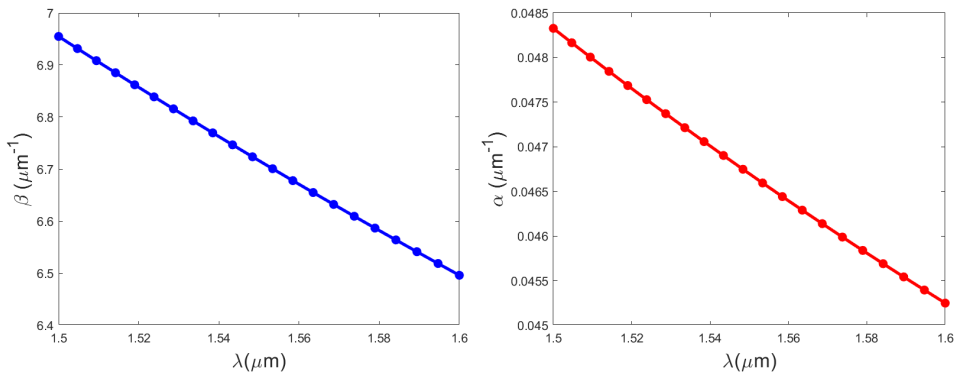

Fig. 2.6 Propagation constant of FDE example versus wavelength.

2.3 Finite-Difference Time-Domain Method

The Finite-Difference Time-Domain method (FDTD) is widely used in optical component modelling, especially for the modelling of photonic integrated circuits (PIC). This method numerically solves Maxwell's equations in the time domain on a discrete mesh in space, without any assumption or approximation [9]. The electromagnetic components are defined on a Yee cell (Fig. 2.7)[9]. The method is very accurate but it has very demanding memory requirements. Since it is a time-domain technique, it is possible to obtain broadband frequency-domain results from single time-domain simulation. The FDTD is mainly used when the size of the structure is of the order of a wavelength. For larger structures, other method such as ray tracing are more computationally convenient.

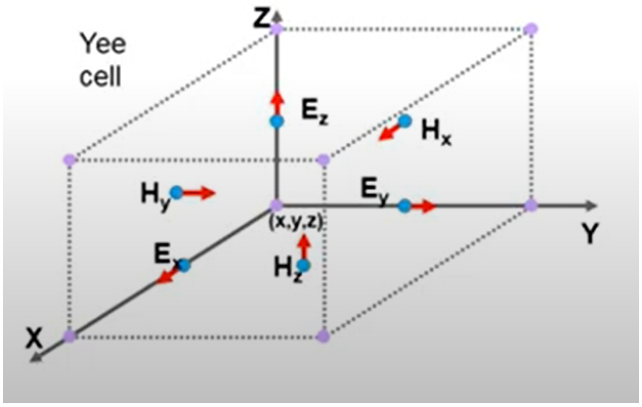

Fig. 2.7 Yee cell[9].

2.4 Finite Element Method

The finite element method (FEM) is a well know technique to numerically solve partial differential equations, and can be used in the modeling of an electro-optic structure. In our study, an in-house electromagnetic mode solver based on FEM is used [16]. Considering the plasmonic slot on Fig. 2.5, this solver can find the plasmonic mode in the slot, and also the radio frequency (RF) field excited when a voltage is applied between the left and right metal layers (Gold in this case). In this way, if the slot is filled with an electro-optic material, the refractive index variation induced by the RF field can be evaluated, and the effective index variation of the plasmonic mode can be obtained from the optical solution.

2.5 Modal-FDTD Method

In this section, the modal-FDTD method presented in [17] is reviewed. The FDTD is very accurate but it is computationally demanding in terms of memory and CPU time requirements, which makes the optimization of a structure through repeated analyses harder. To overcome the huge computational costs of FDTD, is it possible to use the modal-FDTD method. The method is much faster than FDTD (more than ten times), with the same accuracy. Even though the compact footprint of plamonic modulators makes the direct use of FDTD not impossible, it is rather prohibitive, considering that, in the simulation of the static modulator transfer characteristic, each applied voltage level requires a different FDTD simulation. In plasmonic Mach-Zehnder modulators (Fig. 1.10), by inspecting the top view of the device shown in Fig. 2.8, one can imagine to apply an intermediate modelling strategy between FDTD and waveguide-only simulations (FEM or FDE). It is possible to divide the geometry in three sections: the input splitter, two coupled waveguides (the phase shifters) as a central part, and the output combiner, that is the same structure as the input splitter, but mirrored. The modal-FDTD method exploits FDTD simulations only for the splitter/combiner and waveguide simulations for the central part. In the final stage, by using transmission line theory, the full performance of the device can be estimated, with good agreement with FDTD. Since the phase modulators consist of two (coupled) waveguides, this device resembles a bimodal Fabry-Pérot

interferometer (BFPI) [18], whose concept is sketched in the left-bottom part of Fig. 2.8.

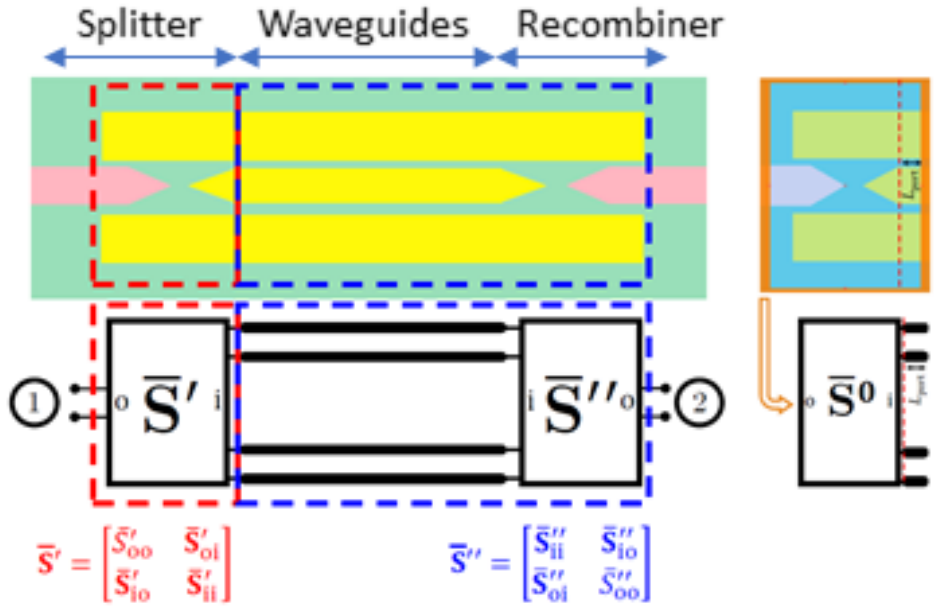

Fig. 2.8 Top-left:The view of plasmonic Mach-Zehnder modulator. Bottom-left: schematic representation of a bimodal Fabry-Pérot interferometer, indicating the correspondence with the blocks of the MZM on top. Right: top view of the 3D model of the splitter to be simulated for the Modal-FDTD strategy.

At the first step of the modal-FDTD strategy, the splitter part is simulated by FDTD at applied voltage $V = 0$. This simulation provides by itself interesting data, such as an estimate of the photonic-plasmonic coupling losses. In the following, we will discuss how to combine this simulation to the waveguide-only analysis. Considering only 2 *internal* modes to describe the modulator response, FDTD Lumerical allows to compute, through the *S-parameter* functionality, a 3×3 matrix where, *e.g.,* port 1 indicates the fundamental mode of the Si waveguide, and ports 2 and 3 the two plasmonic modes considered for the slot waveguides. This matrix can be re-arranged as:

$$\bar{\mathrm{S}}^{\mathrm{L}} = \left[\begin{array}{c|cc} \bar{\mathrm{S}}^{\mathrm{L}}_{oo} & \bar{\mathrm{S}}^{\mathrm{L}}_{oi} \\ \hline \bar{\mathrm{S}}^{\mathrm{L}}_{io} & \bar{\mathrm{S}}^{\mathrm{L}}_{ii} \end{array}\right] = \left[\begin{array}{c|cc} \bar{S}_{11} & \bar{S}_{12} & \bar{S}_{13} \\ \hline \bar{S}_{12} & \bar{S}_{22} & \bar{S}_{23} \\ \bar{S}_{13} & \bar{S}_{23} & \bar{S}_{33} \end{array}\right] \tag{2.37}$$

Coherently with Fig. 2.8 (left), the subscripts "*o*" and "*i*" are used to indicate the ports located *outside* and *inside* the modulator, respectively. In equation (3.3), the superscripts "*L*" are used to remark that the scattering matrix blocks include the transmission line segment with length L_{port} indicated in Fig. 2.8 (right). In order to obtain the final 0 volt splitter matrix $\bar{S}^0$, one should de-embed such transmission lines, defining (at $V_{RF} = 0\,\text{V}$) the phase shift matrix $\underline{\underline{E}}_{\text{port}}$ as:

$$\underline{\underline{E}}_{\text{port}} = \text{diag}_{\{i=1,2\}} \left\{ e^{(-jk_0(n_{eff,i} - j\kappa_i)L_{port})} \right\} \tag{2.38}$$

where $n_{eff,\text{i}}$, κ_i can be obtained from (possibly multiphysics) waveguide simulations. Finally, de-embedding is performed by applying:

$$\begin{aligned} \bar{\text{S}}^0_{oo} &= \bar{\text{S}}^L_{oo} \\ \bar{\text{S}}^0_{io} &= \text{E}^{-1}_{port}\, \bar{\text{S}}^L_{io} \\ \bar{\text{S}}^0_{oi} &= \bar{\text{S}}^L_{oi}\, \text{E}^{-1}_{port} \\ \bar{\text{S}}^0_{ii} &= \text{E}^{-1}_{port}\, \bar{\text{S}}^L_{ii}\, \text{E}^{-1}_{port}. \end{aligned} \tag{2.39}$$

2.6 Electro-optic Effect Model

In the electro-optic modulator, a material with nonlinear optical properties is essential. In our case, the plasmonic modulator under study is assumed contain a nonlinear organic polymer (NLO) called DLD164 [19, 20, 11], which exhibits strong Pockels effect. Fig. 2.9 shows the refractive index of NLO (n_{NLO}) versus wavelength [21]. During deposition of this material, a large poling voltage ($V_{\text{poling}} \approx 400$ V) is applied to the structure; the large resulting electric field allows, with a convenient process temperature, to rotate the active molecules (chromophores) of the NLO, making them align to the applied field. The alignment resulting from the poling process remains at ambient temperature even after that the poling voltage is removed. Imposing a now a RF electric field, the material refractive index n_{NLO} changes according to the equation:

$$\Delta n_{EO} = \frac{1}{2} r_{33} n^3_{NLO} E_{\text{RF}} \tag{2.40}$$

where Δn_{EO} is the refractive index variation, r_{33} is the electro-optic coefficient of the NLO and E_{RF} is RF electric field. If the E_{RF} has a component along the same direction as the poling field, Δn_{EO} is positive; otherwise, Δn_{EO} is negative. Also, the

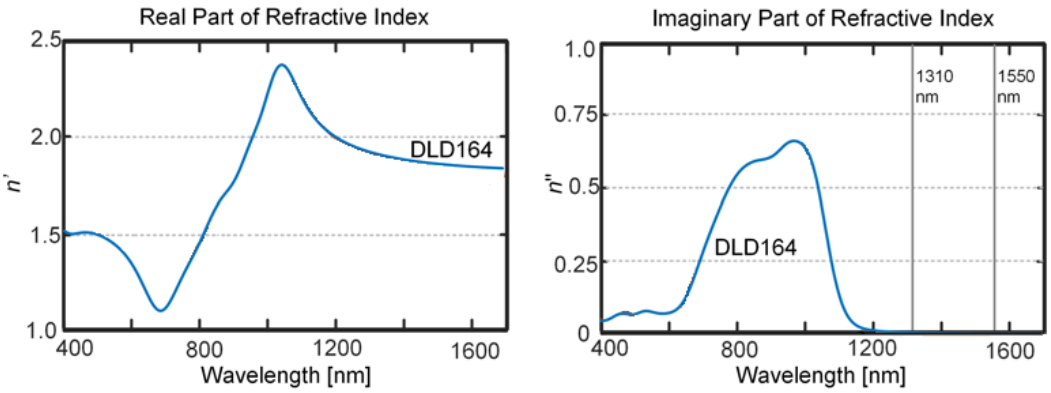

Fig. 2.9 Refractive index of NLO DLD164 polymer[21].

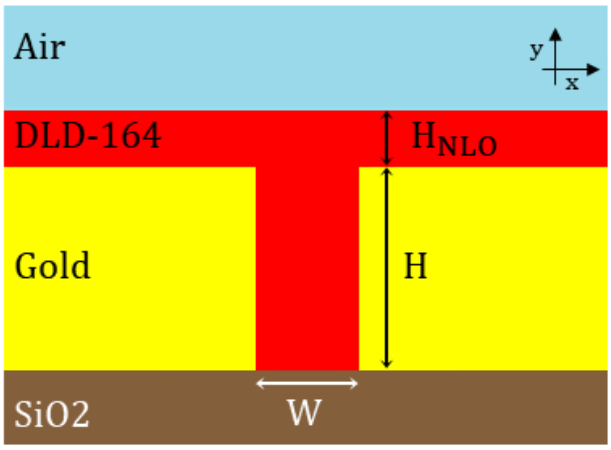

Fig. 2.10 Cross section of a plasmonic slot[12].

permittivity can be easily calculated from following equation:

$$\varepsilon_{EO} = (n_{NLO} + \Delta n_{EO})^2 \tag{2.41}$$

Considering the plasmonic phase modulator in Fig. 1.9, the cross section of the plasmonic waveguide is similar to the one in Fig. 2.10. By applying a RF voltage V_{RF} between the right and left metals, the electric field in the electro-optic material varies, thus providing the required Δn_{EO}. if the optical propagation direction is z direction, the cross section would be in the $x-y$ plan similar to Fig. 1.9. Assuming that E_{RF} has negligible z component, the E_{RF} can be decomposed to x and y direction

(E_{x} and E_{y}, respectively):

$$\Delta n_{EO} = \frac{1}{2} r_{33} n_{NLO}^3 \sqrt{\left|E_x^2 + E_y^2\right|} \tag{2.42}$$

The E_x component, much larger than E_y, is dominant. Since the width of slot (W) is small (of the order of 100 nm), E_x can be approximated by a parallel-plate approx as V_{RF}/W, leading to:

$$\Delta n_{EO} \approx \frac{1}{2} r_{33} n_{NLO}^3 E_x^2 \approx \frac{1}{2} r_{33} n_{NLO}^3 \frac{V_{\mathrm{RF}}}{W} \tag{2.43}$$

Chapter 3

Plasmonic Mach–Zehnder Modulator

This chapter is focused on the modeling of plasmonic-organic hybrid Mach-Zehnder modulators. The interest in these devices is related to their natural compatibility with silicon photonics platforms and to the non-diffraction limited characteristics of the plasmonic waveguide enable nanoscale cross-sections and microscale total lengths, which allow chip-scale integration [22, 23]. Such small cross-sections lead to very large radiofrequency (RF) electric fields with reduced driving voltages, enhancing the E/O effect and allowing for sub-THz bandwidths. These exceptional features are paid with the very strong propagation losses characterizing plasmonic modes, which are about 1 dB/μm. Nevertheless, the extremely compact achievable footprints enable an energy consumption of the order of fJ/bit, making these devices attractive for low-power communication systems [24–26].

As mentioned in previous chapters, in plasmonic modulators, the E/O material is based on chromophore molecules dispersed in a host polymer medium, which are previously oriented by a static poling electric field [19, 20, 11]. Modulation of the material refractive index is enabled by applying a RF electric field to the poled material. This material fills the phase shifters slots, which are designed to support plasmonic modes [27]. Thanks to the nanometer scale of slot widths, very large RF electric fields can be obtained with low applied voltages.

It is therefore clear how a comprehensive model should predict the E/O modulation from RF electrical simulations, whose results are used to obtain a complex, position-dependent refractive index profile as the input of the optical model.

In the last decades, the Microwave and Optoelectronics Group (MOG) of the Department of Electronics and Telecommunication (DET) of Politecnico di Torino has developed several competences in the modeling of semiconductor electro-absorption and electro-optic modulators. Starting from these foundations, the contribution developed in the framework of this chapter has been the set-up of a new simulation framework for plasmonic-organic hybrid electro-optic modulators. In this view, different simulation approaches have been developed. First, I have attacked the problem with 3D-FDTD, which is the most comprehensive optical model for these devices, capable of studying the entire geometry, paid at the price of extremely severe memory and computational requirements. Then, I have investigated the limitations of 2D modal simulations, which allowed to obtain a first estimate of the modulator static/dynamic response [28]. In an attempt to achieve results comparable to those of the 3D-FDTD with computational requirements comparable to modal simulations, I have contributed to the theoretical development, implementation and validation of the modal-FDTD method presented in this chapter.

3.1 Geometry

The plasmonic Mach-Zehnder modulatore (PMZM) under analysis, sketched in Fig. 3.1, is similar to the one presented in [12]. The structure is fabricated on a SiO_2 layer 3 μm thick, grown on a Si substrate (not shown in the figure but included in the electrical simulations). The two arms of the PMZM are the slot waveguides

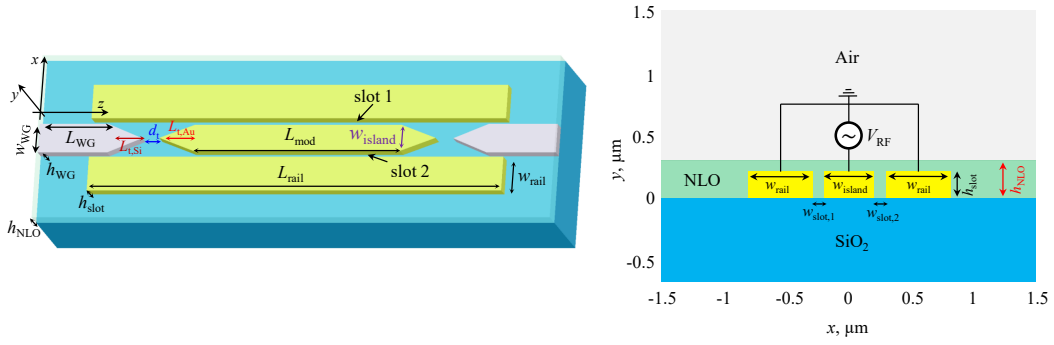

Fig. 3.1 Left: 3D representation of the device under test, including all the relevant geometrical in Tables 3.1–3.2. Right: sketch of the (x,y) cross-section of the device under test, including the RF voltage circuit.

Table 3.1 Geometrical parameters of the cross-section shown in Fig. 3.1(right).

Quantity	$w_{\text{slot,1}}$	$w_{\text{slot,2}}$	h_{slot}	h_{NLO}	w_{island}	w_{rail}
Value, unit	90 nm	100 nm	220 nm	300 nm	400 nm	520 nm

Table 3.2 Parameters of the geometry shown in Fig. 3.1(left)

Quantity	L_{mod}	L_{rail}	$L_{\text{t,Au}}$	d_{t}	$L_{\text{t,Si}}$	L_{WG}	h_{WG}	w_{WG}
Value, unit	6 μm	12 μm	1 μm	500 nm	1 μm	4 μm	200 nm	440 nm

embedded between the central gold island and the two lateral gold rails. The optical input signal is assumed to be the fundamental mode of the input (left) Si waveguide. This mode reaches a splitter, consisting of a couple of facing tapers (left in Si, right in Au), which convert the dielectric waveguide mode into the plasmonic modes supported by the slots. The device is symmetrical with respect to the central z section (the center of the gold island), so that, after propagating in the slots, the plasmonic modes are recombined and couple to the output Si waveguide. The device is immersed in the DLD-164 non-linear optic (NLO) material, with thickness h_{NLO}. Modulation is achieved through the electro/optic effect induced by the RF voltage, which is applied to the central island contact. The RF field changes the effective refractive index of the plasmonic modes in the phase shifters, leading to a voltage-dependent interference at the output combiner, which ranges from constructive (ON state) to destructive (OFF state).

The phase modulators are driven in push-pull operation by a single signal, using the coplanar ground-signal-ground transmission line sketched in Fig. 3.1(right)[29–31, 23]. This is obtained by aligning the poling field for the E/O polymer to the modulation RF field, the latter having opposite polarity in each modulator arm. By inspecting the geometrical details reported in Table 3.1, one can notice that the two slot widths are different. This comes from a precise choice, as it allows to tune the PMZM to operate around the quadrature point (where linearity is maximum) at zero bias voltage [12].

3.2 Multiphysics simulations

The simulation strategy is explained in the following subsections.

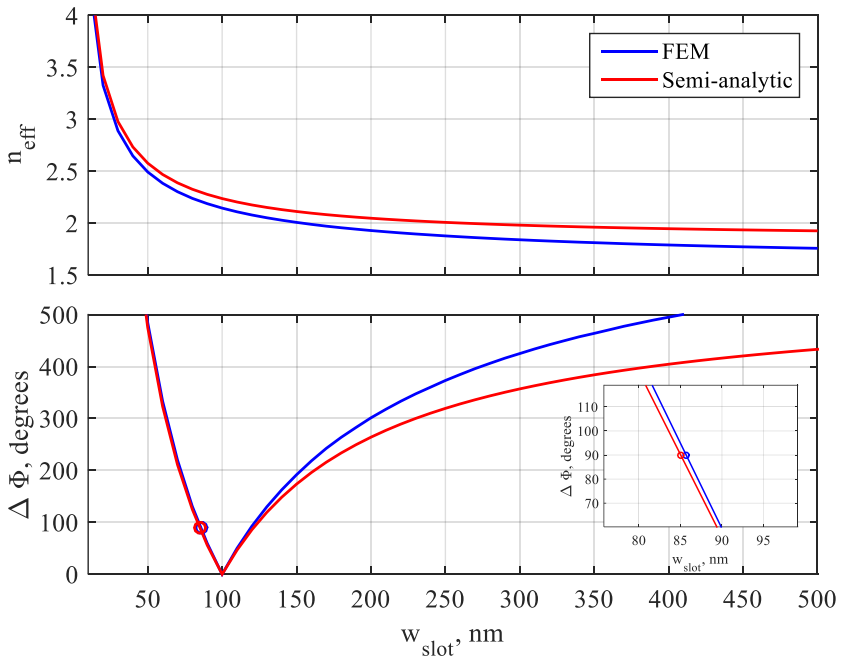

Fig. 3.2 Top: effective index of an isolated slot waveguide versus slot width performed with no E/O effect ($V_{RF} = 0\,V$). Bottom: 0 V phase shift of a PMZM with $L_{mod} = 6\,\mu m$ with one slot width fixed to 100 nm and varying the other. The simulations have been performed at $\lambda = 1.55\,\mu m$. The blue curve has been simulated with an electromagnetic mode solver based on FEM, including all the geometrical details presented in Fig. 3.1(right) for $x \geq 0$. The red curve has been obtained approximating the geometry as a metal-insulator-metal waveguide and using semi-analytical expressions.

3.2.1 Cold (zero voltage) device simulations

As a first result, Fig. 3.2(top) shows the effective index of a slot waveguide, at zero applied voltage, as a function of the slot width. Here, the results of two models are presented at $\lambda = 1.55\,\mu m$. The blue curve has been obtained by simulating the 2D cross-section of an isolated slot (*i.e.,* simulating the (x,y) cross-section shown in Fig. 3.1(right), just for $x \geq 0$). The simulation of plasmonic slot waveguides has been widely addressed in the literature, with a broad spectrum of techniques including the effective index method [32], circuit approaches [33, 34], finite difference schemes either in time [35] or in frequency [36] domains, finite elements [37], Fourier modal methods [38], and integral-equation schemes [39]. In this work, waveguide simulations have been performed with an in-house electromagnetic mode solver based on the finite element method (FEM) [16]. On the other hand, the red curve has been obtained with a much simpler and widely-available model, based on

approximating the slot geometry as a metal-insulator-metal waveguide (therefore, y-invariant) and using semi-analytical expressions from [40, Ch. 10]. From the top panel one could deduce that the simpler model, even though capturing the general trend vs. the slot width, is inadequate for design purposes. This is partially contradicted by the analysis in the bottom panel. Here, recalling that the phase shift of a single PMZM arm at 0 V applied voltage is $\Phi = k_0 n_{\text{eff}} L_{\text{mod}}$, we plot the phase difference between the two arms (where one of the arms is 100 nm wide), as a function of the width of the other arm:

$$\Delta\Phi(w_{\text{slot}}) = k_0 L_{\text{mod}} \left| n_{\text{eff}}(w_{\text{slot}}) - n_{\text{eff}}(100\,\text{nm}) \right|, \tag{3.1}$$

where $k_0 = 2\pi/\lambda$, and the phase modulator lengths are assumed to be $L_{\text{mod}} = 6\,\mu$m. Obviously, $\Delta\Phi = 0^\circ$ at $w_{\text{slot}} = 100\,$nm, which corresponds to the symmetric PMZM case. While the semi-analytic model fails to predict $\Delta\Phi$ for wider slots, it is pretty accurate for narrower cases. Targeting at $\Delta\Phi = 90^\circ$, *i.e.,* setting the half-power point at $V_{\text{RF}} = 0\,$V, both models predict $w_{\text{slot}} \simeq 85\,$nm (indicated with the blue and red open bullets), with a deviation smaller than 1 nm. Intuitively, this partial success of the semi-analytic approach could be ascribed to the slot aspect ratio ($h_{\text{slot}} = 220\,$nm). Being the slots narrow, they are quite similar to metal-insulator-metal (MIM) waveguides, justifying the partial validity of the simplification that results useful to perform preliminary optical characterizations of passive plasmonic slots before their electro-optic implementation in a PMZM [41].

3.2.2 Multiphysics-augmented waveguide simulations

The results discussed in the previous section pertain cold device operation. Because of the absence of the modulating radiofrequency field, optical-only simulations are sufficient in this case. Modulation is enabled by imposing an RF electric field, which causes the optical dielectric permittivity of the E/O material to change according to equation (2.41). We neglected the z-dependence of the electro-optic coefficient. This is acceptable in the splitter/recombiner, where the electric field profile is much weaker than in the slots. It is to be remarked that, even if the device under study is simplified (vertical slot walls, isotropic permittivity), in the transverse (x,y) plane this model can describe complex geometries, *e.g.,* including slanted walls such as in [21, Fig. 10(c)], and sophisticated electromagnetic properties, *e.g.,* position-

dependent anisotropic permittivity. On the other hand, 2.41 ignores a possible z-dependence of the poling field, which could arise for example from fluctuations of the slot width/height. The experimental characterizations (see the SEM image from [21, Fig. 10(b)]) suggest that it is reasonable to simulate an *average* slot width. With this hypothesis, the device geometry can be designed on the basis of parametric simulation campaigns, and only the final design verification could be performed by a full 3D electro-opto simulation, limiting the overall computational cost. Because the modulator length is much shorter than the RF wavelength, its frequency response can be reasonably approximated with that of a *RC* circuit, *R* being the device and driver total equivalent resistance and *C* its static capacitance. This allows to reduce the electrical analysis to a quasi-static problem in the 2D cross-section, as shown in Fig. 3.1(right), and to introduce this z-independent E/O effect only in the phase modulators. Electrical simulations lead to the position-dependent $E_{x,\mathrm{RF}}$, $E_{y,\mathrm{RF}}$ field components. They should be interpolated on the optical problem mesh to evaluate Δn_{mat} in its cross-section (the one simulated to produce Fig. 3.2), thus requiring a coupled, multiphysics approach.

In this view, Fig. 3.3 shows the effective refractive index versus the RF voltage V_{RF}. There are three groups of curves, obtained with different degrees of approximations. The green dashed curves are obtained simulating the two slot waveguides separately, treating them as isolated just like in Fig. 3.2, and the approximated E/O refractive index variation model in equation (2.43) has been adopted. These curves clearly are straight lines, intersecting at $V_{\mathrm{RF}} \simeq 4\,\mathrm{V}$, which corresponds to the PMZM ON state (that is the two slot line optical fields are in phase, having the same optical path length).

Still within the approximation (2.43), the dash-dotted red curves have been obtained simulating a cross-section including both slots. Rather than being straight lines, these curves exhibit an almost-parabolic behavior in the proximity of the ON state, and become linear far from it, with almost the same slope of the dashed green lines. Because the two n_{eff} curves are not intersecting, the corresponding phase shift is not zero, suggesting that operation at $V_{\mathrm{RF}} \simeq 4\,\mathrm{V}$ should be a *quasi-ON* state, characterized by an excess loss; this point is further discussed in Section 3.3.3. Finally, the solid blue curves have been obtained including mode coupling and the full description of the E/O effect from (2.43). Here, the RF fields have been simulated with our in-house quasi-static (QS) FEM electric solver [42]. Compared to the dash-dotted red curve, the multiphysics simulation result exhibits a higher

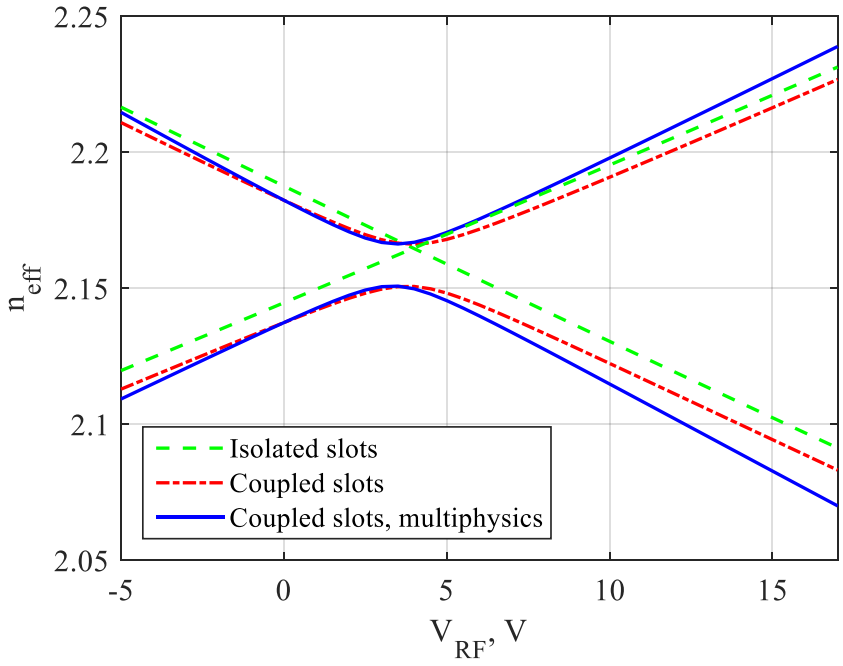

Fig. 3.3 Effective refractive index versus RF voltage V_{RF}. The green dashed curves are obtained simulating two isolated slots (just like in Fig. 3.2) and the red dash-dotted curves considering in the cross section both the slots; both these simulations have been performed under the approximation equation (2.43). The solid blue curves have been performed including mode coupling effects and the multiphysics description equation (2.42) of the E/O effect.

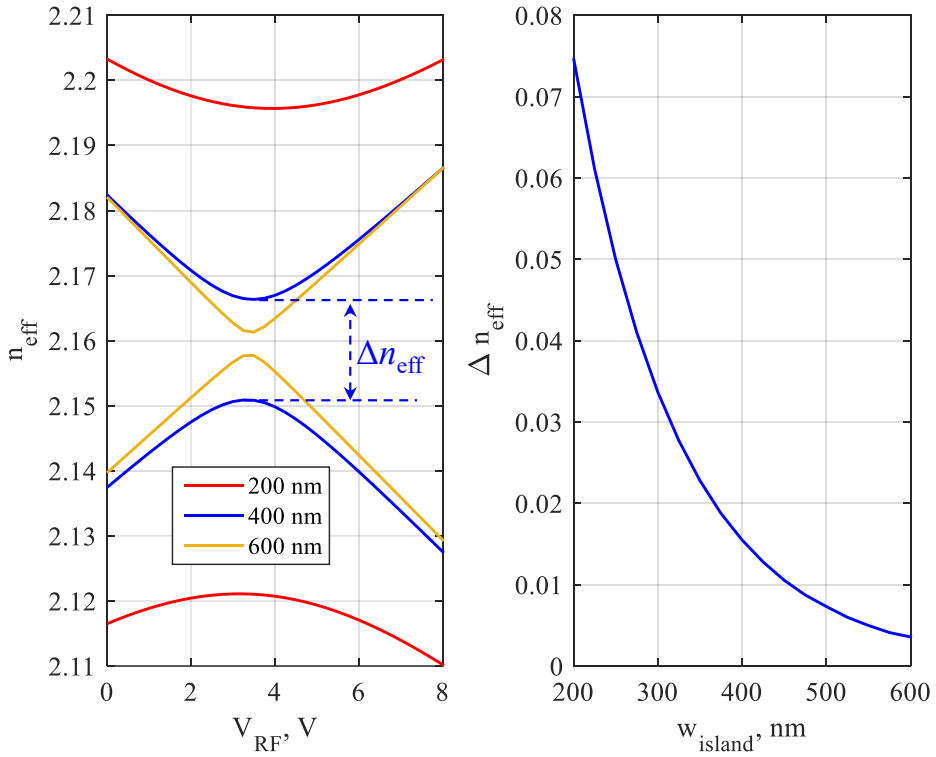

Fig. 3.4 Left: $n_{\text{eff}}(V_{\text{RF}})$ curves for the device under analysis, for different central island widths; the red, blue and orange curves are obtained for $w_{\text{island}} = 200\,\text{nm}$, 400 nm (nominal device) and 600 nm, respectively. The plot shows the definition of Δn_{eff}, *i.e.,* the difference of the effective indexes at the ON voltage V_{ON}. Right: Δn_{eff} as a function of w_{island}. These simulations have been performed with the multiphysics model.

slope, which makes the ON voltage to be shifted at about 3.5 V. In this view, it is clear that (2.43) underestimates the E/O effect.

The parabolic behaviour of the red and blue curves is caused by coupling effects between the two slot modes. Despite in the device under study the slots are quite far away, separated by the gold island, mode coupling is fostered by the surface plasmons of its top/bottom walls. Such behaviour, commonly referred to as *anticrossing*, is indicative of coupling between two modes [43]. This occurs in several EM structures, such as dielectric and photonic crystal waveguides [44, 45] and high-contrast gratings [46–48], but also in semiconductor crystals where coupling between waveparticle modes is present [49].

The strong losses of the top surface plasmonic mode make the anticrossing strongly dependent on the slot separation w_{island}. This is investigated in Fig. 3.4. In

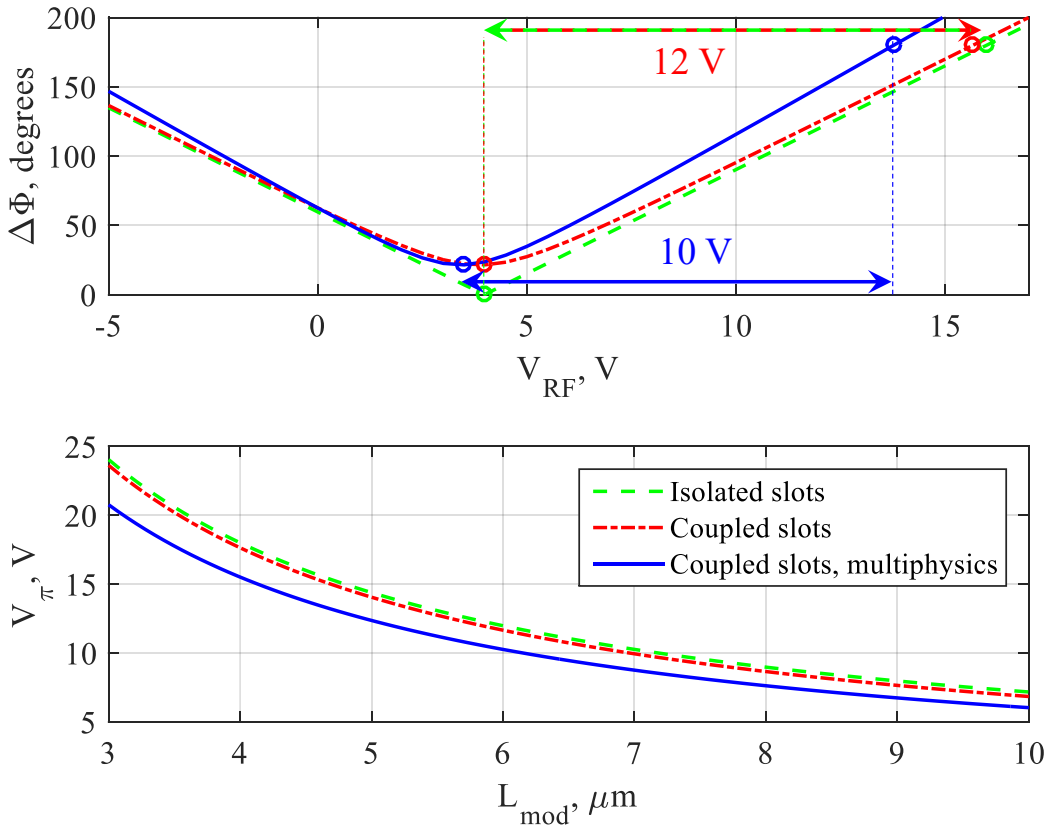

Fig. 3.5 Top: $\Delta\Phi(V_{\mathrm{RF}})$ characteristics evaluated with (3.2) using the waveguide simulations shown in Fig. 3.3, assuming $L_{\mathrm{mod}} = 6\,\mu$m. The green dashed, red dash-dotted and blue solid curves are obtained considering the slots isolated, coupled, and coupled including multiphysics effects, respectively. The horizontal arrows indicate the V_π definitions for the three simulations. Bottom: the curves show the behaviour of V_π versus L_{mod} using the definition indicated in the top panel.

particular, the left panel shows the $n_{\mathrm{eff}}(V_{\mathrm{RF}})$ characteristics curves for three different island widths. Here, the blue curve corresponds to the reference ($w_{\mathrm{island}} = 400$ nm) case reported with the same color in Fig. 3.3. Instead, the red curve ($w_{\mathrm{island}} = 200$ nm) exhibits a much broader n_{eff} splitting, Δn_{eff} (definition in the figure), as a consequence of the increased mode coupling. On the other hand, the orange curves ($w_{\mathrm{island}} = 600$ nm) are almost intersecting, therefore tending to the isolated slot case of Fig. 3.3. A more quantitative information is provided by the right panel, showing Δn_{eff} as a function of w_{island}.

Waveguide simulations can be tentatively used to perform preliminary estimates of the PMZM performance. To this aim, in Fig. 3.5, the electro/opto simulation

results from Fig. 3.3 have been used to obtain a first estimate of the modulator V_π. To this aim, the top panel shows the phase shift $\Delta\Phi(V_{\mathrm{RF}})$ between the two PMZM modes at the recombiner section computed as

$$\Delta\Phi(V_{\mathrm{RF}}) = k_0 L_{\mathrm{mod}} \left| n_{\mathrm{eff},1}(V_{\mathrm{RF}}) - n_{\mathrm{eff},2}(V_{\mathrm{RF}}) \right|, \tag{3.2}$$

where $n_{\mathrm{eff},1}$, $n_{\mathrm{eff},2}$ come from the effective index curves reported in Fig. 3.3. The V_π has been approximated as the difference between the OFF voltage, at which $\Delta\Phi(V_{\mathrm{OFF}}) = 180°$, and the ON voltage, at which $\Delta\Phi(V_{\mathrm{ON}})$ is minimum (zero, in the isolated slots case). Remarkably, the estimate obtained with the multiphysics-augmented simulation (blue curve) are very close to the experimental findings discussed in [12, 41].

To further clarify the importance of a multiphysics treatment, the bottom panel of Fig. 3.5 shows V_π as a function of the modulator length L_{mod}, evaluated as in the top panel. From these results it is not possible to appreciate significant differences between the isolated (green dashed) and coupled (red dash-dotted) slot cases. Instead, it appears that the multiphysics simulation might lead to relevant variations of V_π, which can reach almost 4 V for short modulators. These differences can be understood by analyzing the results reported in Fig. 3.6(left), showing the magnitude of the electric field simulated the QS solver.

The slots can be identified as the regions where the electric field is stronger (tending to red). Moreover, it could be noticed that the field level is slightly higher in the left slot (*i.e.,* the narrower one). The electric field is non-vanishing also out of the slots, which cannot be taken into account by (2.43). This can be better appreciated in Fig. 3.6(right), which shows field cuts performed in the slot center (blue, $y = 110$ nm), at the slot top (red, $y = 220$ nm), and the end of the NLO material (orange, $y = 300$ nm). From the blue curves it can be seen that the estimate (2.43) is very accurate inside the slot (considering $V_{\mathrm{RF}} = 1$ V, the left slot field is 11.1 V/cm, the right one is 10 V/cm). Looking at the red curve, one could notice that the optical field diverges at the slot corners [50, 51]. However, the most relevant effect in this context is the non-vanishing field corresponding to the island, which is related to a residual y field component associated to the island surface plasmons. This is even more evident at the end of the NLO material.

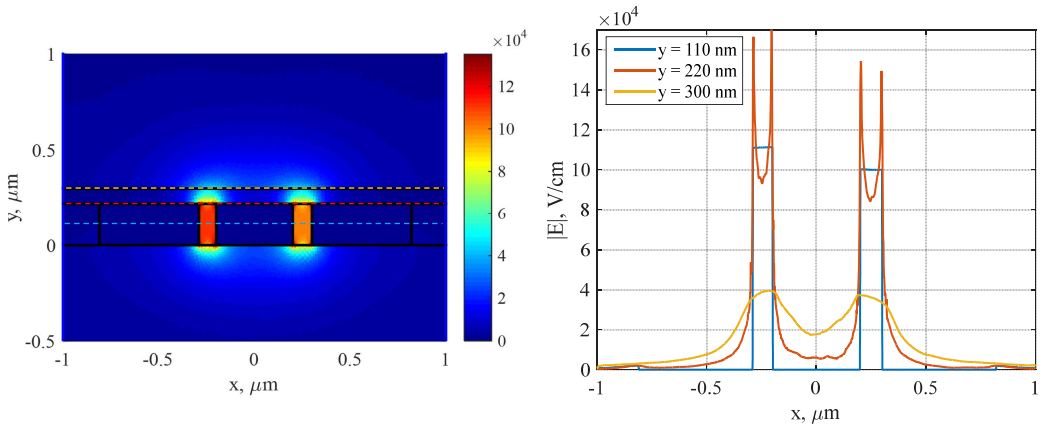

Fig. 3.6 Left: RF electric field map simulated with the QS solver. The black lines are used to indicate the device geometry, to assist the direct comparison with Fig. 3.1(right). The three dashed horizontal lines intersect the slot center (blue, $y = 110\,\text{nm}$), the slot top (red, $y = 220\,\text{nm}$), the end of the NLO material (orange, $y = 300\,\text{nm}$). Right: cuts of the maps on the left (the small oscillations result from the interpolation of the different meshes, necessary to perform the multiphysics coupling (2.42)). The three cuts correspond to the horizontal lines intersecting the slot center (blue, $y = 110\,\text{nm}$), the slot top (red, $y = 220\,\text{nm}$), the end of the NLO material (orange, $y = 300\,\text{nm}$).

3.3 Efficient comprehensive 3D simulation

In the previous section, the V_π voltage has been estimated only on the basis of the effective refractive indexes obtained from waveguide simulations, emphasizing how a multiphysics-augmented framework is instrumental to reproduce the experimental findings. Simple system-level models for the slot optical fields interference at the output combiners, also accounting for the plasmonic loss in each slot (see, *e.g.,* [28, Sect. 6.4]), are customarily exploited to provide an estimate of other important device figures of merit, as the modulator insertion loss (IL) and extinction ratio (ER). However, such simple models neglect a number of effects related to both slot mode coupling and the detailed description of the splitter and recombiner sections, which feed the plasmonic phase modulators and extract the signal from it.

From this viewpoint, the maximum realism is provided by 3D full-wave simulations of the entire device, which in principle can be carried out by commercially-available electromagnetic simulators implementing the finite-difference time-domain method (FDTD), such as RSoft FullWave [52] and Lumerical FDTD Solutions [9] (all the 3D-FDTD simulations used in this work have been performed with the latter). Lumerical, starting from a defined input field source (in this case the Si waveguide

mode in the input splitter), returns the position-resolved 3D profile of the vector electromagnetic field on the entire device. The PMZM response can be defined by post-processing this information. Because the modulator is embedded within a complex optical system featuring grating couplers and other components which can filter out spurious contributions, it is reasonable to base this definition on the fundamental mode of the output waveguide. By projecting the total (3D) field on it, a mode transmission coefficient S_{21} can be defined, whose absolute value squared can be interpreted as a $P_{\text{out}}/P_{\text{in}}$.

3.3.1 *Mixed modal-FDTD* simulation and cold splitter characterization

Even if the compact footprint of POH MZMs makes such an *all-in-one* approach not impossible, it is rather prohibitive, considering that each RF voltage level requires a different 3D-FDTD simulation. For example, Fig. 3.7 shows a top view (xz plane) of the magnitude of the optical electric field in a PMZM in the OFF (top) and ON (bottom) states. This information is completed by Fig. 3.8, which reports, in the same conditions, the magnitude of the optical electric field in the output dielectric waveguide. Both figures clearly show that at V_{ON} the fields at the recombiner are in phase and interfere constructively while, at V_{OFF}, destructive interference lead to the extinction of the output field.

Fig. 3.7 shows a. This information is completed by Fig. 3.8, which reports, in the same conditions,

By inspecting the top view of the device in Fig. 2.8, one can imagine an intermediate strategy between *all-in-one* 3D-FDTD and waveguide-only simulations: instead of modeling numerically the entire device, it is possible to focus the 3D-FDTD simulations only on the splitter/recombiner (which are actually equal, just mirrored), and the central part by means of waveguide simulations and transmission line theory. Since the phase modulators consist of two waveguides, this device resembles a bimodal Fabry-Pérot interferometer (BFPI) [18]. Here, the cavity transmission lines describe the plasmonic modes supported by the PMZM, whose voltage-dependent dispersion properties have been presented in Section 3.2.1 and now are be re-used to avoid to simulate by 3D-FDTD the phase modulators, minimizing the simulation number and cost, and are coupled mutually and to the outer ports (fundamental

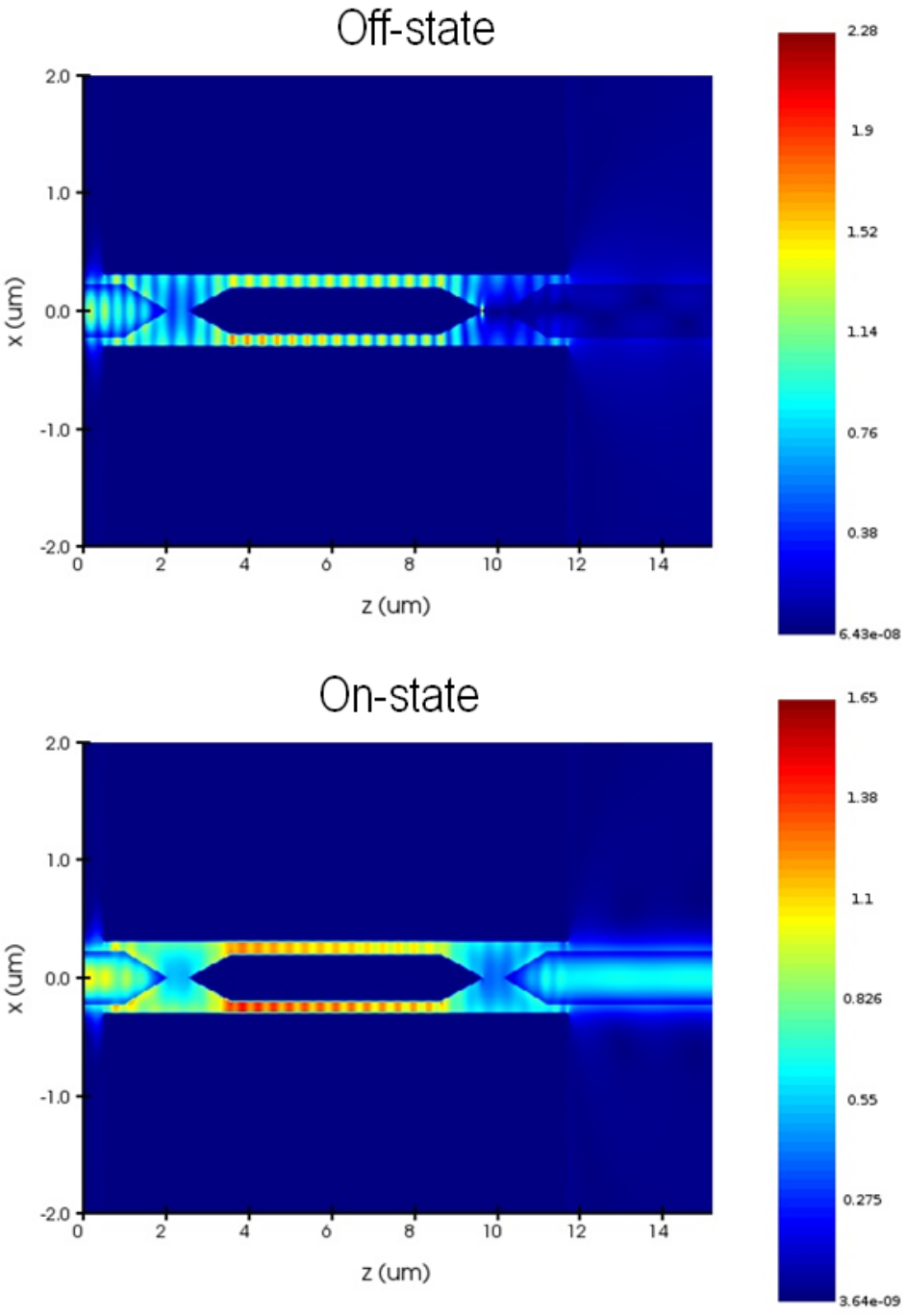

Fig. 3.7 Top view (*xz* plane) of the magnitude of the optical electric field in a PMZM for OFF and ON states.

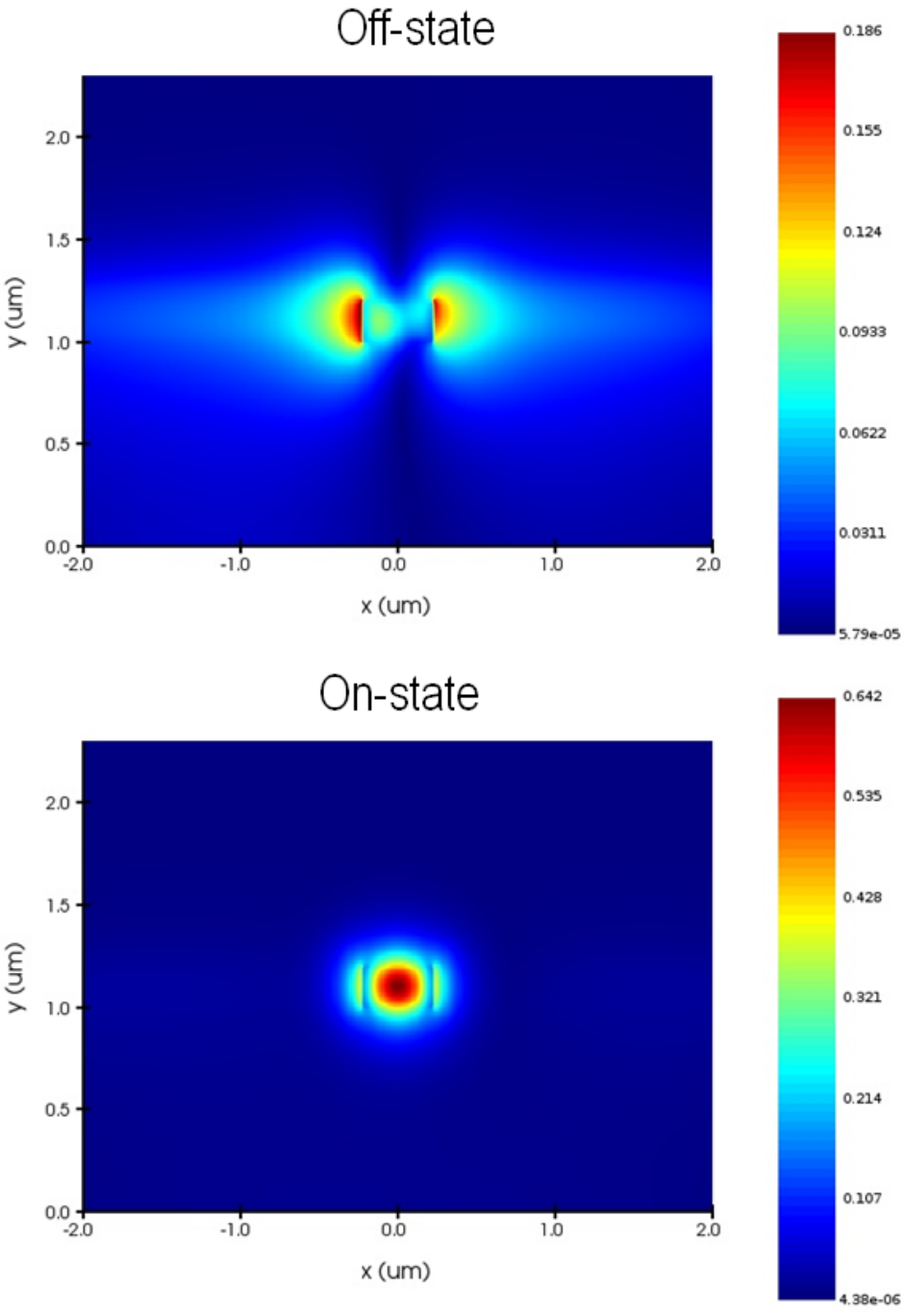

Fig. 3.8 The magnitude of the optical electric field in the output dielectric waveguide in a PMZM in for OFF and ON states.

Si waveguide modes) by the scattering matrices describing the splitter/recombiner. Then, the device response can be computed as the cascade of the splitter, cavity and recombiner transmission matrices.

The first step of this mixed modal-FDTD (MFDTD) strategy requires simulating, with the 3D-FDTD, only the section sketched in Fig. 2.8(right), at $V_{\mathrm{RF}} = 0\,\mathrm{V}$. This starts from the input waveguide, and is terminated after a length L_{port} from the splitter end, as indicated by the dashed vertical line; this transmission line segment is introduced just to avoid problems that originate from terminating the device too close to metal corners. This simulation provides by itself interesting data, such as an estimate of the coupling losses due to photonic-plasmonic interference (PPI) (see [41, Fig. 11]). Considering only 2 *internal* modes to describe the modulator response, Lumerical allows to compute, through the *S-parameter sweep* functionality, a 3×3 matrix where, *e.g.,* port 1 indicates the fundamental mode of the Si waveguide, and ports 2 and 3 the two plasmonic modes considered for the slot waveguides. This matrix can be re-arranged as

$$\overline{\mathbf{S}}^{\mathrm{L}} = \left[\begin{array}{c|c} \overline{S}^{\mathrm{L}}_{\mathrm{oo}} & \overline{\mathbf{S}}^{\mathrm{L}}_{\mathrm{oi}} \\ \hline \overline{\mathbf{S}}^{\mathrm{L}}_{\mathrm{io}} & \overline{\mathbf{S}}^{\mathrm{L}}_{\mathrm{ii}} \end{array}\right] = \left[\begin{array}{c|cc} \overline{S}_{11} & \overline{S}_{12} & \overline{S}_{13} \\ \hline \overline{S}_{12} & \overline{S}_{22} & \overline{S}_{23} \\ \overline{S}_{13} & \overline{S}_{23} & \overline{S}_{33} \end{array}\right]. \tag{3.3}$$

Coherently with Fig. **??**(left), the subscripts "o" and "i" are used to indicate the ports located *outside* and *inside* the modulator cavity, respectively. In (3.3), the superscripts "L" are used to remark that the scattering matrix blocks include the transmission line segment long L_{port} indicated in Fig. **??**(right). In order to obtain the final 0 volt splitter matrix $\overline{\mathbf{S}}^{0}$, one should de-embed such transmission lines, requires defining (at $V_{\mathrm{RF}} = 0\,\mathrm{V}$) the phase shift matrix $\mathbf{E}_{\mathrm{port}}$ as:

$$\mathbf{E}_{\mathrm{port}} = \underset{i=1,2}{\mathrm{diag}} \left\{ \exp\left(-\mathrm{j}k_0(n_{\mathrm{eff},i} - \mathrm{j}\kappa_i)L_{\mathrm{port}}\right) \right\},$$

where $n_{\mathrm{eff},i}$, κ_i can be obtained from (possibly multiphysics) waveguide simulations analogous to those shown in Fig. 3.3. Finally, de-embedding is performed by

applying:

$$\begin{aligned}
\overline{S}^{0}_{\mathrm{oo}} &= \overline{S}^{\mathrm{L}}_{\mathrm{oo}} \\
\overline{\mathbf{S}}^{0}_{\mathrm{io}} &= \mathbf{E}^{-1}_{\mathrm{port}}\,\overline{\mathbf{S}}^{\mathrm{L}}_{\mathrm{io}} \\
\overline{\mathbf{S}}^{0}_{\mathrm{oi}} &= \overline{\mathbf{S}}^{\mathrm{L}}_{\mathrm{oi}}\,\mathbf{E}^{-1}_{\mathrm{port}} \\
\overline{\mathbf{S}}^{0}_{\mathrm{ii}} &= \mathbf{E}^{-1}_{\mathrm{port}}\,\overline{\mathbf{S}}^{\mathrm{L}}_{\mathrm{ii}}\,\mathbf{E}^{-1}_{\mathrm{port}}.
\end{aligned} \tag{3.4}$$

3.3.2 Voltage-dependent mode coupling effects

The superscript "0" in (3.4) indicates that the matrices (3.4) are computed and valid only for $V_{\mathrm{RF}} = 0$ V. Even under the hypothesis of introducing the E/O effect in the phase modulators only, the splitter/recombiner scattering matrix depends on voltage, since the ports and transmission line parameters are defined starting from modal basis of the phase modulators, whose elements are voltage-dependent.

This is shown in Fig. 2.8, which reports the cuts of the real part of E_x in the slot center ($y = 110$ nm) for the two modes. Invoking the molecular orbital taxonomy, the coupled slots supermodes 1 and 2 are antibonding- and bonding-like, respectively. Three V_{RF} values are considered: 0 V (green dash-dotted curves: cold regime), $V_{\mathrm{ON}} = 3.5$ V (blue dashed curves), and 8 V (red solid curves). The mode topographies are clearly voltage-dependent. In fact, at $V_{\mathrm{RF}} = 0$ V modes are mostly localized in the left and right slots, respectively. At $V_{\mathrm{RF}} = 8$ V, modes are still localized, but with switched order. Instead, at V_{ON} modes tend to assume odd and even parities. This is a signature of mode coupling, just like the parabolic-like behaviour of $n_{\mathrm{eff}}(V_{\mathrm{RF}})$ in Fig. 3.3: coupling is strongest at V_{ON} and decreases at smaller or lower applied voltages. For this reason, the matrix $\overline{\mathbf{S}}^{0}$ from (3.4) differs from the $\overline{\mathbf{S}}'_{\mathrm{ii}}$ indicated in Fig. 2.8, as it does not take into account such mode coupling. Therefore, obtaining the voltage-dependent $\overline{\mathbf{S}}'$ from $\overline{\mathbf{S}}^{0}$ still requires a change of basis matrix $\mathbf{W}(V_{\mathrm{RF}})$ from the modes computed for the cold device to those with a non-zero E/O effect:

$$\begin{aligned}
\overline{S}'_{\mathrm{oo}}(V_{\mathrm{RF}}) &= \overline{S}^{0}_{\mathrm{oo}} \\
\overline{\mathbf{S}}'_{\mathrm{io}}(V_{\mathrm{RF}}) &= \mathbf{W}^{\mathrm{H}}(V_{\mathrm{RF}})\,\overline{\mathbf{S}}^{0}_{\mathrm{io}} \\
\overline{\mathbf{S}}'_{\mathrm{oi}}(V_{\mathrm{RF}}) &= \overline{\mathbf{S}}^{0}_{\mathrm{oi}}\,\mathbf{W}(V_{\mathrm{RF}}) \\
\overline{\mathbf{S}}'_{\mathrm{ii}}(V_{\mathrm{RF}}) &= \mathbf{W}^{\mathrm{H}}(V_{\mathrm{RF}})\,\overline{\mathbf{S}}^{0}_{\mathrm{ii}}\,\mathbf{W}(V_{\mathrm{RF}}),
\end{aligned} \tag{3.5}$$

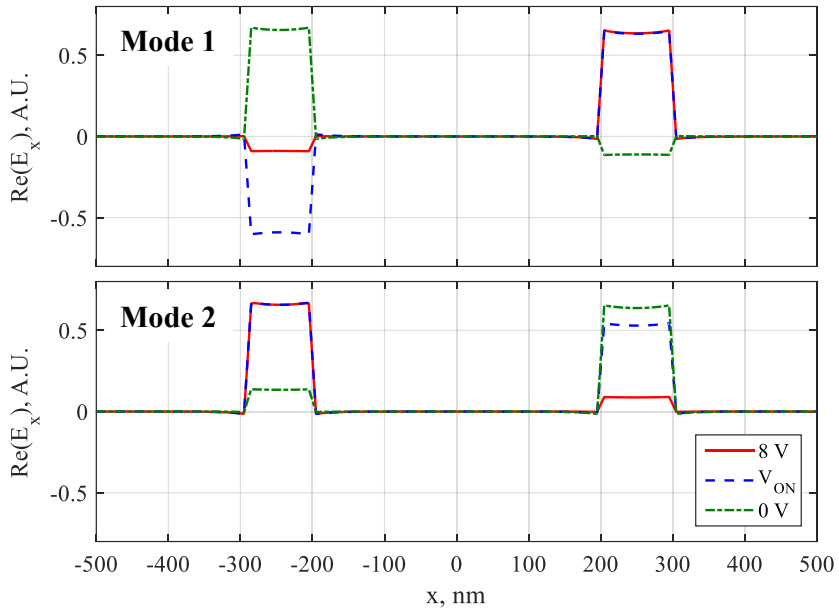

Fig. 3.9 Cuts of the real part of E_x in the slot center ($y = 110$ nm) reported for the two modes. The top and bottom panels show mode 1 (antibonding-like) and mode 2 (bonding-like), respectively, for three V_{RF} values: 0 V (green dash-dotted curves: cold regime), $V_{\mathrm{ON}} = 3.5$ V (blue dashed curves), and 8 V (red solid curves)

Computing the 2×2 change of basis matrix $\mathbf{W}(V_{\mathrm{RF}})$ in principle requires a mode-matching technique, where the field continuity at the interface between cold and biased waveguide sections should be performed including the complete mode spectrum. This is the case occurring, *e.g.,* in high-contrast gratings: even if their operation can be described just by 3×3 scattering matrices, computing their entries requires a mode-matching with a large number of modes to expand/project the fields at the bar-air discontinuities [53]. In the case of dielectric waveguides this is even more troublesome, since the electromagnetic problem is theoretically unbounded, and one should include also the continuum part of the mode spectrum. A possibility is mimicking free-space by closing the problem within a very large computational box, whose modal expansion is known analytically [54]. A handier, still very general approach is through 3D-FDTD simulations of a discontinuity between a plasmonic slot without/with E/O effect. In practice, this could be achieved by simulating two short transmission line segments, and then de-embedding the lines in a similar fashion to (3.4).

As it could be appreciated in the cuts reported in Fig. 3.9, the mode topographies are very localized, which is a signature of their plasmonic character. Moreover,

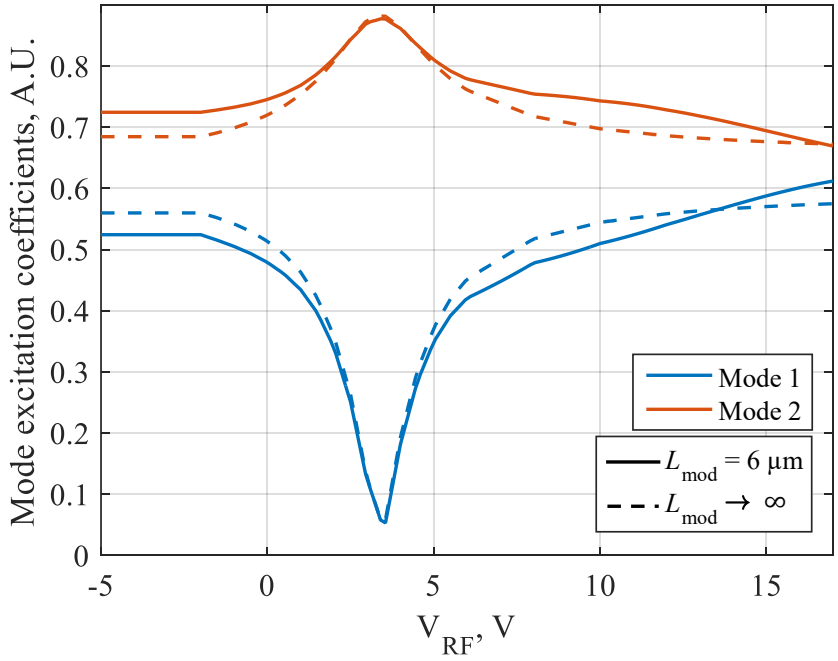

Fig. 3.10 Excitation coefficients at the onset of the modulator section (end of the splitter) versus voltage; the solid and dashed curves are obtained for $L_{\mathrm{mod}} = 6\,\mu$m and for a very long modulator ($L_{\mathrm{mod}} > 40\,\mu$m).

voltage introduces just a mild dielectric discontinuity within the slots, without introducing any other significant change in the geometry. This explains why the mode topographies without/with voltage are so similar. In this view, in these devices, one can approximate the mode basis at a given voltage as a linear combination of the elements of the basis at a different voltage. This consideration allows the matrix $\mathbf{W}(V_{\mathrm{RF}})$ to be derived from the coefficients of this linear combination, which can be obtained solving a least-squares problem, whose formulation is reported in Appendix B. It has been verified that the change-of-basis matrices obtained with the two methods agree well, enabling to use both approaches with similar results.

The effect of the voltage-dependent mode coupling on the plasmonic modulator feed can be appreciated in Fig. 3.10. Here, the dashed curves are obtained plotting $\overline{\mathbf{S}}'_{\mathrm{oi}}(V_{\mathrm{RF}})$, which corresponds to the case of a very long modulator ($L_{\mathrm{mod}} \geq 40\,\mu$m). The solid curves are obtained plotting $(\mathbf{I} - \overline{\mathbf{S}}'_{\mathrm{ii}}\overline{\mathbf{S}}''_{\mathrm{ii}})^{-1}\overline{\mathbf{S}}'_{\mathrm{io}}$ for $L_{\mathrm{mod}} = 6\,\mu$m, *i.e.,* including cavity effects (which are instead negligible in long interferometers due to the high plasmonic losses). In both cases, the curves can be interpreted as the *excitation coefficients* of the modes (being, more specifically, the magnitudes of the progressive

waves) at the onset of the modulator section, with/without cavity effects. It should be noticed how two groups of curves exhibit similar trends for every V_{RF}, and are almost equal in the V_{ON} region. This suggests that in opposite to V_{OFF}, which is strongly affected by the modulator length, the V_{ON} and the corresponding mode excitation coefficients are quite independent on it.

3.3.3 Evaluating the modulator response

Once $\overline{\mathbf{S}}'$ is determined, it can be used to find the matrix $\overline{\mathbf{S}}''$ as:

$$\begin{aligned}
\overline{S}''_{\mathrm{oo}}(V_{\mathrm{RF}}, L_{\mathrm{mod}}) &= \overline{S}'_{\mathrm{oo}}(V_{\mathrm{RF}}) \\
\overline{\mathbf{S}}''_{\mathrm{io}}(V_{\mathrm{RF}}, L_{\mathrm{mod}}) &= \mathbf{E}_{\mathrm{mod}}\, \overline{\mathbf{S}}'_{\mathrm{io}}(V_{\mathrm{RF}}) \\
\overline{\mathbf{S}}''_{\mathrm{oi}}(V_{\mathrm{RF}}, L_{\mathrm{mod}}) &= \overline{\mathbf{S}}'_{\mathrm{oi}}\, \mathbf{E}_{\mathrm{mod}}(V_{\mathrm{RF}}) \\
\overline{\mathbf{S}}''_{\mathrm{ii}}(V_{\mathrm{RF}}, L_{\mathrm{mod}}) &= \mathbf{E}_{\mathrm{mod}}\, \overline{\mathbf{S}}'_{\mathrm{ii}}(V_{\mathrm{RF}})\, \mathbf{E}_{\mathrm{mod}},
\end{aligned} \tag{3.6}$$

where E_{mod} depends both on V_{RF} and on the modulator length L_{mod}:

$$\mathbf{E}_{\mathrm{mod}} = \underset{i=1,2}{\mathrm{diag}} \left\{ \exp\left(-\mathrm{j} k_0 (n_{\mathrm{eff},i}(V_{\mathrm{RF}}) - \mathrm{j}\kappa_i(V_{\mathrm{RF}})) L_{\mathrm{mod}} \right) \right\}.$$

Finally, the modulator reflection (S_{11}) and transmission (S_{21}) coefficients can be obtained by cascading the two matrices from (3.5) and (3.6):

$$\begin{aligned}
S_{11} &= \overline{S}'_{\mathrm{oo}} + \overline{\mathbf{S}}'_{\mathrm{oi}} \overline{\mathbf{S}}''_{\mathrm{ii}} (\mathbf{I} - \overline{\mathbf{S}}'_{\mathrm{ii}} \overline{\mathbf{S}}''_{\mathrm{ii}})^{-1} \overline{\mathbf{S}}'_{\mathrm{io}} \\
S_{21} &= \overline{\mathbf{S}}''_{\mathrm{oi}} (\mathbf{I} - \overline{\mathbf{S}}'_{\mathrm{ii}} \overline{\mathbf{S}}''_{\mathrm{ii}})^{-1} \overline{\mathbf{S}}'_{\mathrm{io}}.
\end{aligned} \tag{3.7}$$

The validation of the MFDTD is performed versus the *all-in-one* 3D-FDTD results, as shown in Fig. 3.11. Each of the *all-in-one* simulations (one different 3D-FDTD simulation for each RF voltage) consist of 144 millions Yee nodes, requiring about 7 hours on a HP ProLiant DL560 Gen9 computer (featuring 512 GB RAM), parallelizing on all the Intel Xeon E5-4627 v3 (10-core) four CPUs. On the other hand, MFDTD requires a single 3D-FDTD simulation performed at $V_{\mathrm{RF}} = 0\,\mathrm{V}$, involving just the splitter section (48 millions Yee nodes), which are combined to the multiphysics-augmented waveguide simulations to trace the full (voltage-dependent) modulator response.

The responses simulated with the two methods are reported with solid red and dashed black curves. The 3D-FDTD simulations (both *all-in-one* and splitter-only) have been performed using a uniform mesh (5 nm step in all directions) within the modulator section (central island, slots, part of the rails and gold tapers), and with the Lumerical *auto non-uniform* setting, with *mesh accuracy* parameter set to 5 (high accuracy). In the phase modulators, the E/O effect is evaluated from 2D quasi-static analyses (multiphysics approach) just like in Fig. 3.3, blue curve. The figure shows also the definitions of extinction ratio (ER) and insertion loss (IL), which are about 14.5 dB and 4.7 dB, agreeing qualitatively with the experimental findings from [12, 41] (measured ER is 20 dB, measured IL is 5 dB).

The remarkable agreement between the two curves, even at -18 dB levels is validating not just the MFDTD algorithm, but demonstrates also the bimodal character of the PMZM under study. It is to be remarked that the MFDTD algorithm could be extended, in a straightforward fashion, to devices whose operation involves a higher number of modes. In such cases, the rightmost matrix in (3.3) would be larger than 3×3, but it could be still possible grouping the parameters as $S^{\mathrm{L}}_{\mathrm{oo}}$, $\overline{\mathbf{S}}^{\mathrm{L}}_{\mathrm{oi}}$, $\overline{\mathbf{S}}^{\mathrm{L}}_{\mathrm{io}}$, and $\overline{\mathbf{S}}^{\mathrm{L}}_{\mathrm{ii}}$. Even though these blocks would have different dimensions, eqs. (3.4)–(3.7) could be still applicable.

This method allows parametric investigations versus the modulator length at no additional computational cost. As an example, Fig. 3.12(left) shows the modulator responses obtained for $L_{\mathrm{mod}} = 3\,\mu$m, $5\,\mu$m, and $7\,\mu$m (blue, red, and orange curves, respectively). Considering the longer modulators (smaller V_π), it appears that the curves are almost periodic. It is to be remarked that neither the orange nor the purple curves exhibit appreciable differences between the ILs evaluated at the two ON states, which instead could be expected from the waveguide simulations reported in Fig. 3.3. This could be understood from the analysis of Fig. 3.10: at the first ON voltage (about 3.5 V) the first, antibonding-like supermode, which in this case is quasi-odd (see Fig.3.9, top), is weakly excited. On the other hand, the bonding-like supermode is strongly excited. Being one supermode almost suppressed, no interference between the supermodes takes place at the recombiner, and the field propagates in both slots only according to the lower n_{eff} from Fig.3.3. This is why no excess loss can be observed. At the higher V_{ON}, the modes are strongly decoupled, *i.e.*, localized in the single slots (as one can infer from Fig.3.9), and the output power results from their constructive interference at the recombiner, which in this situation can be estimated with equation (3.2).

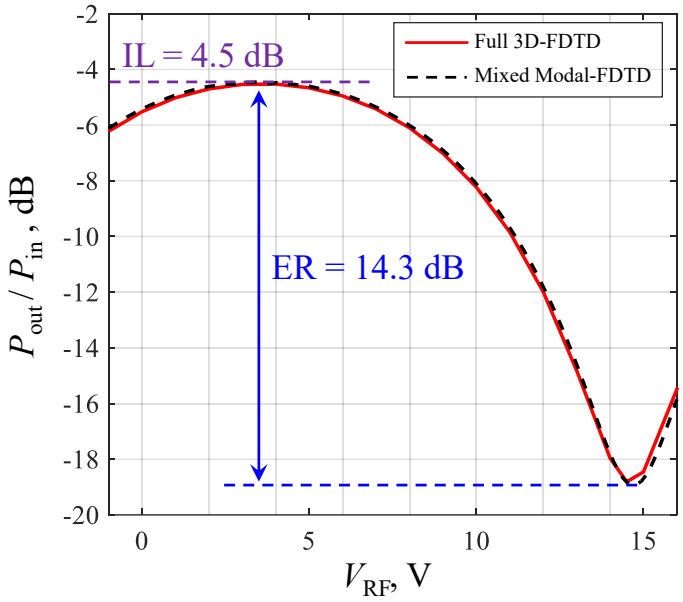

Fig. 3.11 Modulator response simulated with the *all-in-one* 3D-FDTD model (solid red curve), and with the MFDTD approach (dashed black curve). The 3D-FDTD and MFDTD curves have been evaluating $|S_{21}|^2$ from equation (3.7). The figure reports also the definitions of extinction ratio (ER) and insertion loss (IL).

A synthetic representation of the relation between the three fundamental figures of merit is reported in Fig. 3.12(right): V_π, ER, IL. Focusing on the abscissas, Fig. 3.5(bottom) suggests that it can be, in first approximation, interpreted as $1/L_{\text{mod}}$, as reported on the upper horizontal axis. (Indeed, according to a simplified modulator model, the product $V_\pi L_{\text{mod}}$ is constant). The thinner curves exhibit an oscillatory behaviour, which is particularly evident in the ER curve, whose calculation involves the logarithm (dB) of small quantities. These oscillations can be ascribed to cavity effects (also visible in the results of Fig. 3.10); as a matter of fact, their amplitude decreases at increasing L_{mod} (and therefore at increasing losses in the phase modulators). Focusing on the average trends (thicker curves), the lower plasmonic losses in shorter modulators lead to reduced insertion loss. The interpretation of the trend of the ER (generally decreasing with V_π and correspondingly increasing with L_{mod}) is less obvious. Longer modulators are characterized by lower V_π, therefore closer to V_{ON}, which is independent of L_{mod}. In this case, the excitation of the even mode at V_π increases (approaching the mode 2 peak at 3.5 V in Fig. 3.10), thus deteriorating field extinction.

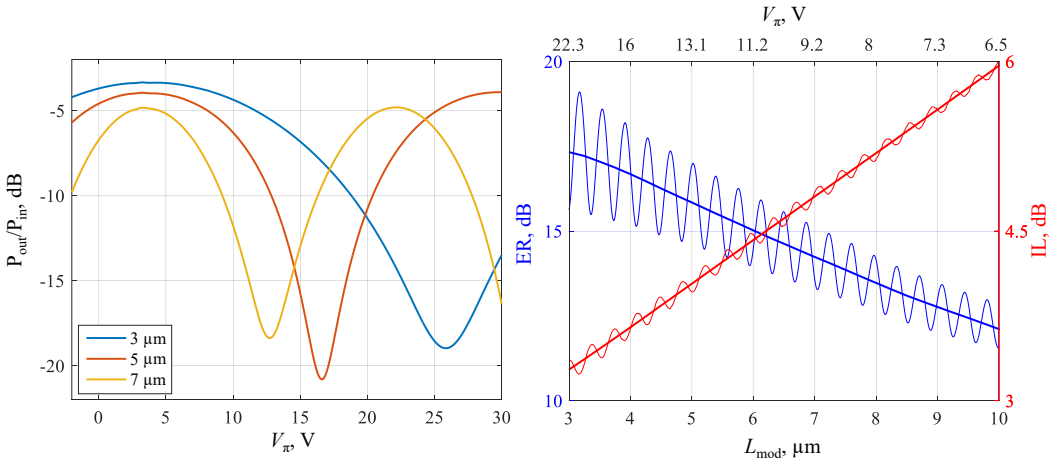

Fig. 3.12 Left: plot of the PMZM response for different modulator lengths: the blue, red, and orange curves refer to $L_{\text{mod}} = 3\,\mu$m, $5\,\mu$m, and $7\,\mu$m, respectively. Right: plot of the extinction ratio (ER, thinner blue curve, referred to the left axis) and insertion loss (IL, thinner red curve, referred to the right axis) as a function of L_{mod}, obtained from S_{21} from the simulated modulator response equation (3.7). The thicker curves are used to emphasize the average trends. The top abscissas axis shows the corresponding V_π.

This analysis provides some guidelines towards the design of these devices. In MZMs, mode coupling is a detrimental effect, impacting in particular on the ER. As suggested by Fig. 3.4, which characterizes mode coupling on the basis of Δn_{eff} at V_{ON}, better performance could be achieved for large w_{island}. As an example, the device presented in [55], exhibiting ERs greater than 20 dB, falls in this situation (slot separation of about $100\,\mu$m). In order to achieve good ERs without increasing the transverse footprint, Fig. 3.12 suggests to sacrifice V_π and design short interferometers. In this way the resulting modulator will have good IL, due to the moderate plasmonic losses, and reduced mode coupling at V_π. As a different route, one could investigate coupler modulators where, as opposite to MZMs, mode coupling is the enabling physical mechanism [56].

Chapter 4

Plasmonic Directional Coupler Modulator

One of the outcomes of the previous chapter, focused on Mach-Zehnder modulators, is that their operation is limited by the coupling of the phase modulator modes, fostered by presence of surface plasmons on the island separating the two slot waveguides. Starting from this observation, I figured that mode coupling could be exploited as an asset, proposing the plasmonic directional coupler (PDC) modulator concept. In addition to their conception, my individual contribution has been the set-up of a simulation framework for PDC modulators based on 2D FDTD and FDE, presented also in [57]. Then, I have investigated possible advantages of realizing PDC modulators based on three, rather than just two waveguides, demonstrating better modulation in terms of length of device and operating voltage. Finally, I have contributed to the theoretical development and validation of the semianalytical simulation approach presented in [58] and in this chapter.

The operation principle of plasmonic directional coupler modulators (PDCM) is similar altogether to the one of other directional coupler modulators that have been proposed as an alternative to MZ modulators both in III-V technologies [57, 58] and on lithium niobate, in concentrated [59] or traveling-wave [60] form. With respect to MZ solutions, DC modulators exhibit some interesting features, like the possibility of dual complementary output and of achieving zero or bias-tunable positive or negative chirp [61].

In what follows, after reviewing the plasmonic directional coupler behavior, a detailed study is presented on coupled-slot coplanar PDC EO modulators, whose aim is to show that a PDC modulator with interesting performance can be implemented with layout and fabrication processes similar altogether to those presented in [12, 41, 21] for the realization of POH coupled-slot MZ modulators.

4.1 Plasmonic Directional Coupler

The directional coupler consists of two (or more) waveguides which are close together enough to allow optical power to couple between them. Fig. 4.1 top illustrates a common directional coupler in Silicon foundry [ipkiss]. A common application of directional coupler is as an optical power splitter and the separation between waveguides (d) plays an essential role in the coupling efficiency. As seen in the FDTD simulations (Fig. 4.1 bottom), for large separation distance, $d = 2\mu m$, the optical signal remains in one waveguide and does not interact with the other waveguide. Conversely, for low separation distance, $d = 200nm$, after propagating for a certain interaction (coupling) length (L_c), the optical signal is transferred to the other waveguide. If directional coupler lenght is large enough, the power coupling periodically repeats over L_c.

Because of the interaction between waveguides, two supermodes are present, where one of them is even and another one is odd. By using FDE, the computed even and odd supermodes for ($d = 2\mu m$) are presented in Fig. 4.2. When the optical signal is only in the right waveguide, it can be represented by adding supermodes; conversely, when the optical signal is only in the left waveguide, this can be represented by mode subtraction (Fig. 4.2 bottom-right and bottom-left, respectively). If the signal exists between the right and left waveguides, it will a superposition, with complex amplitude coefficients, of the supermodes. A FDE simulation shows that, for large d, the effective refractive index of the even supermode (n_{even}) and the effective refractive index of the odd supermode (n_{odd}) are the same, and by decreasing d, their values increasingly differ. For instance, at $d = 2\mu m$ the effective refractive index for both supermodes are equal to $n_{even} = n_{odd} = 2.4452$; while at $d = 200nm$ they are different $n_{even} = 2.4565$ and $n_{odd} = 2.4361$. This variation of the effective refractive index can be related to L_c. The CMT method can be used to prove that the coupling length L_c depends on the difference between the propagation

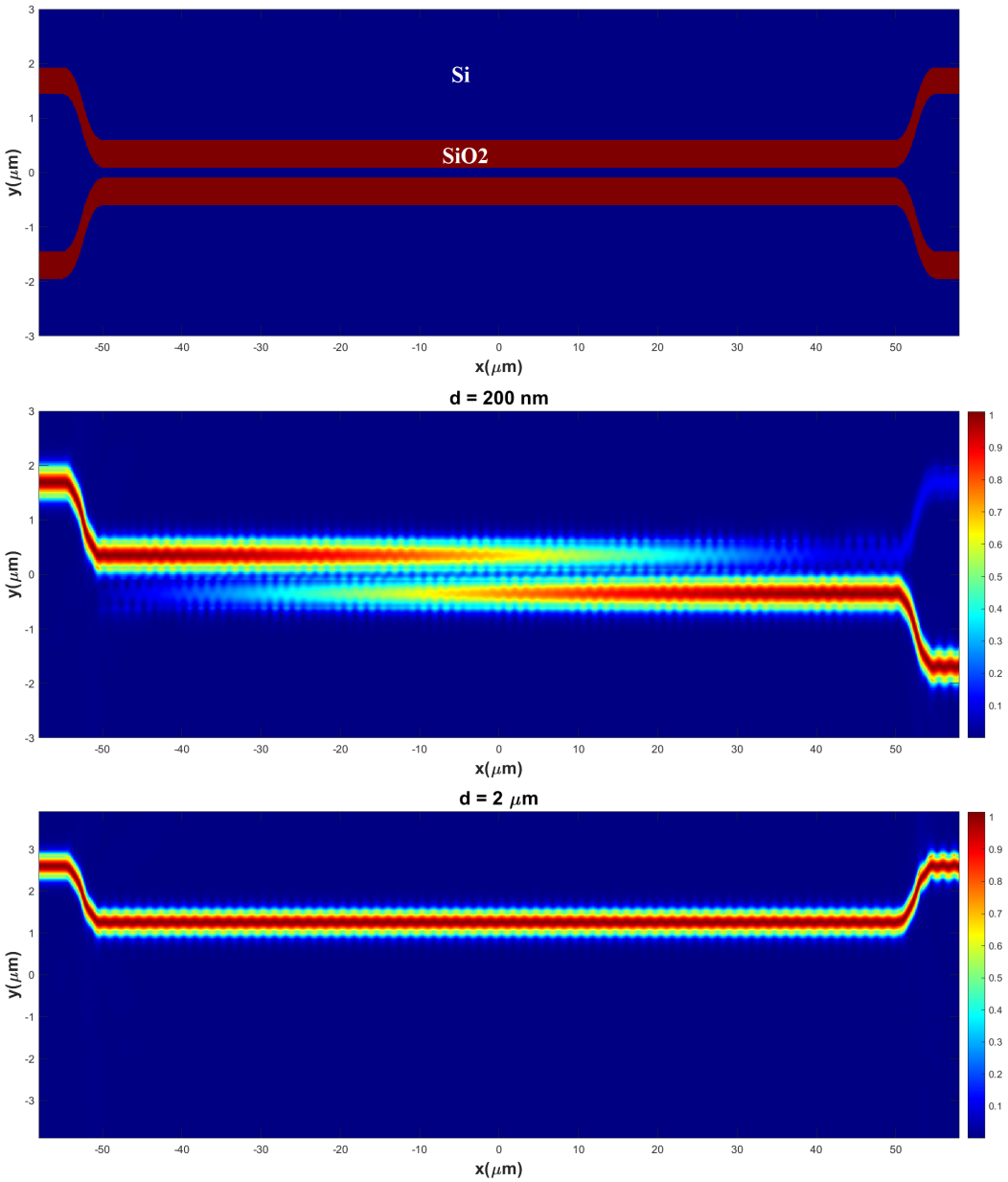

Fig. 4.1 Top: geometry of a silicon direction coupler. Middle: electric field FDTD simulation for $d = 200nm$. Bottom: electric field FDTD simulation for $d = 2\mu m$.

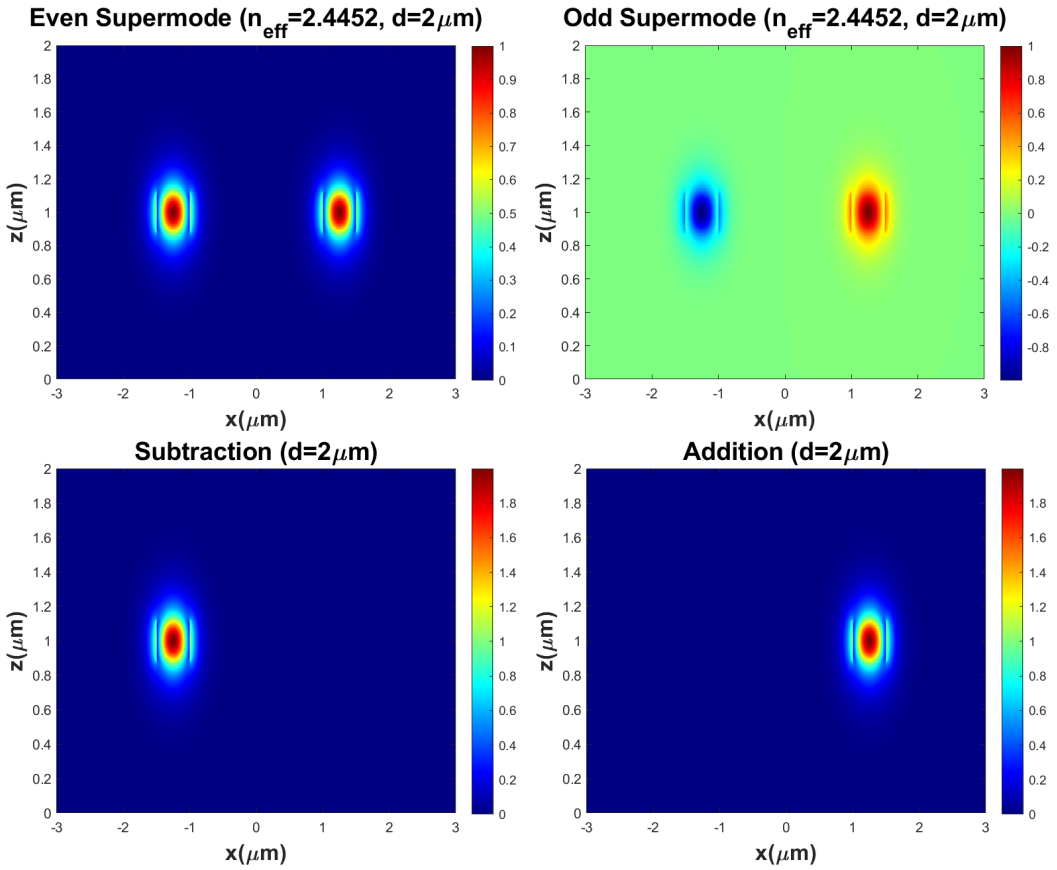

Fig. 4.2 Top-left: The even supermode for a direction coupler with $d = 2\mu m$. Top-right: The odd supermode. Bottom-left: subtraction of supermodes. Bottom-right: Addition of supermodes.

constants of the supermodes (β_{even} and β_{odd}) according to [**?**]:

$$L_c = \frac{\pi}{\beta_{even} - \beta_{odd}} = \frac{\lambda}{2(n_{even} - n_{odd})} \tag{4.1}$$

The β_{even} and β_{odd} are computed over d (Fig. 4.3). Also, according to equation (4.1), the L_c is estimated from them(Fig. 4.4). The L_c has strong sensitivity to d. For instance, $L_c = 76.19\ \mu m$ at $d = 200nm$, and dramatically increases to $1025.24\ \mu m$ for $d = 500nm$.

Similar to the silicon directional coupler, the plasmonic directional coupler can be implemented by implementing two plasmonic waveguides close together. If the waveguides are close enough, the power can couple between them. Fig. 4.5 shows the cross section of a plasmonic directional coupler with 2 slot waveguide (PDC2).

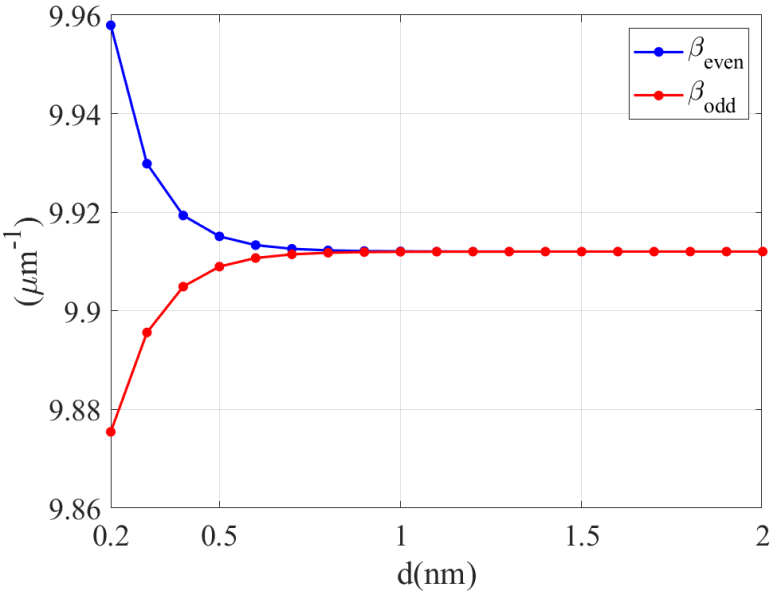

Fig. 4.3 The propagation constant of even and odd supermodes in a Silicon directional coupler versus d.

The propagation constant of the even and odd supermode are calculated by using FDE method (Fig. 4.5 bottom) for different values of d.

Considering equation(4.1), when d larger than 700 nm, $\beta_{even} \approx \beta_{odd}$ and L_c tends to a very large value (of the order of hundred mm); which means that negligible or no power coupling occurs. The waveguides are not interacting with each other. For d smaller than 700 nm, β_{even} and β_{odd} exhibit an increasing difference for decreasing d , leading to a decrease of L_c (of the order of a few μm); which means waveguides interact and the optical waves are coupled from one waveguide to the other one.

Let us now suppose that the plasmonic slots are filled by an electro-optic material (e.g., by the DLD-164 polymer). If a voltage is applied to the metals, due to the electro-optic effect of DLD-164, the refractive index of DLD-164 is changed, thus affecting the propagation parameters β_{even} and β_{odd}, which leads to the change of L_c. In a suitable geometry, a modulator can be implemented based on controlling the coupling length L_c of PDC. In the other words, the idea behind plasmonic directional coupler modulator is changing L_c of the directional coupler by applying a voltage and thus controlling the power in the output (coupled) waveguide. This will be explained in detail in the next section.

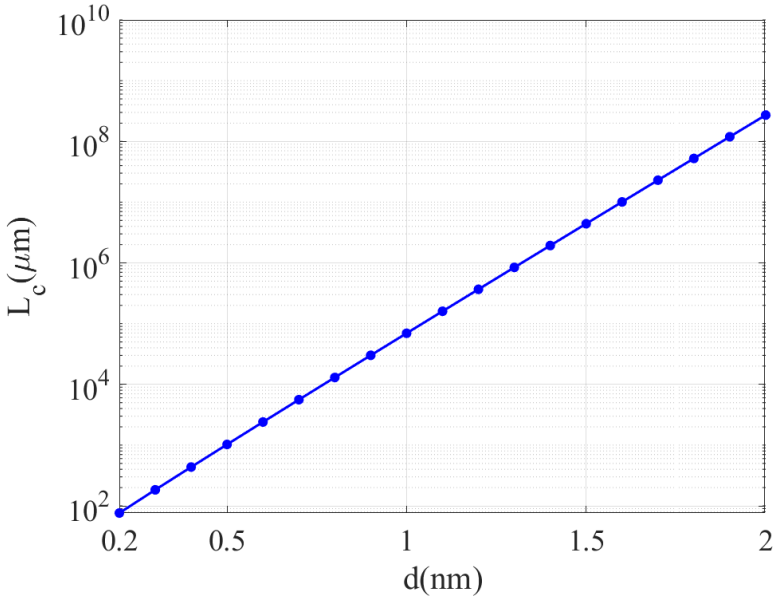

Fig. 4.4 The L_C versus d.

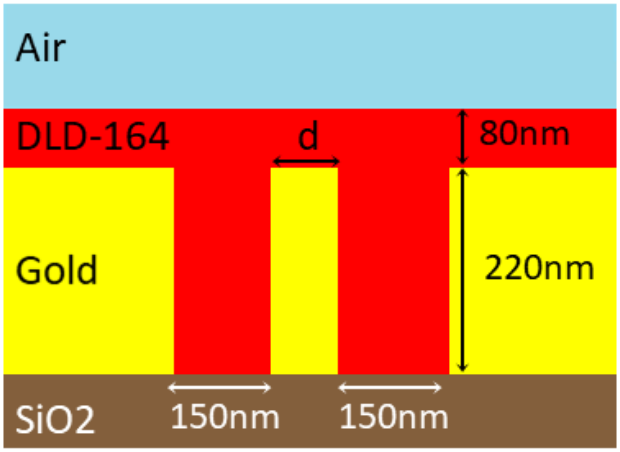

Fig. 4.5 Cross section of a PDC2.

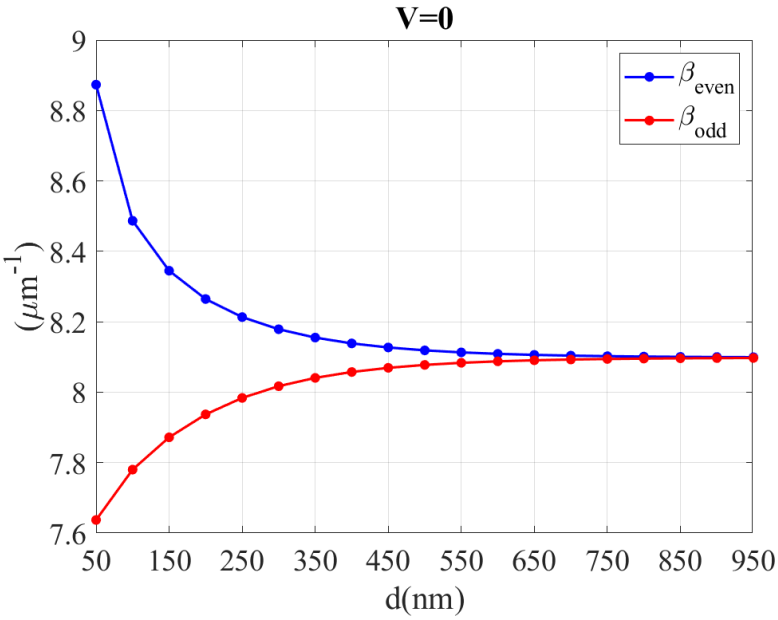

Fig. 4.6 The propagation constant of even and odd supermode of PDC2 versus d.

4.2 PDC2 Modulator

Directional coupler modulators generally exploit two coupled optical waveguides, where coupling can be controlled externally. In the implementation described in this paper, coupling is controlled through the electro-optic effect, by varying the refractive index in the slot waveguides through the application of an electric field, induced by the input voltage. In principle, the device has two input and two output ports, since it allows both *through* and *cross-coupling* transmission to the output port. For the sake of definiteness, we will mainly focus on the *through* configuration, where the input and output ports are located on the same plasmonic slot; the performance of the cross-coupling configuration, which is complementary as far as the EO response is concerned, but with different chirp [61], will also be mentioned.

The layout of the PDC2 modulator under investigation is shown in Fig. 4.7. Each color indicates a different material. The main figure reports a top view of the device, with an inset representing the xy cross-section indicated by the red dashed line. As shown in the inset, the device is fabricated on a SiO_2 layer, grown on a Si substrate (omitted in the figure). On top of the SiO_2 layer, three parallel Au pads are deposited, one connected to the input voltage source, comprising the radiofrequency (RF) modulating signal and the DC bias, the other two connected to ground. The

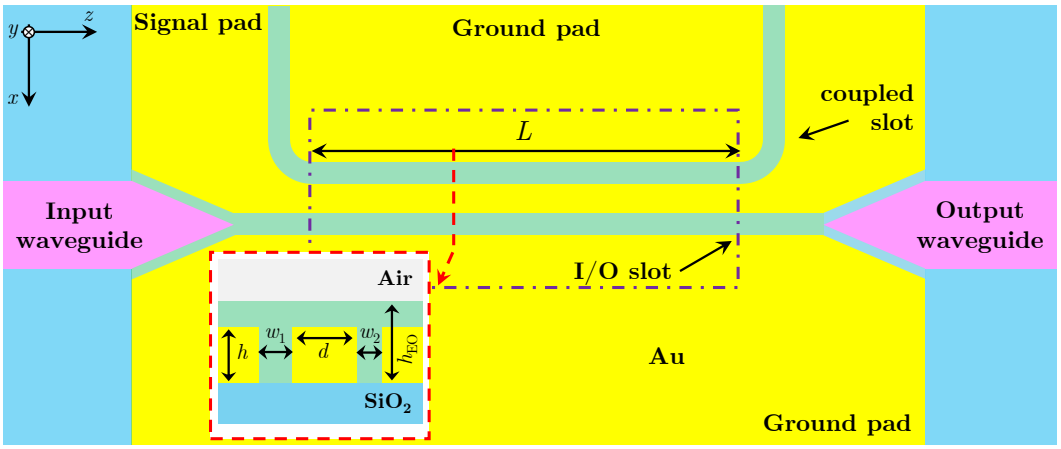

Fig. 4.7 Geometry of the device under investigation. The main figure reports the *xz* top view for *y* corresponding to the slot center. The inset reports the *xy* cross-section indicated by the red dashed line. Each color indicates a different material: the NLO polymer DLD-164 is green, air is gray, Au is yellow, SiO_2 is dark blue, Si is lilac. The DLD-164 layer only extends to the straight portion of the device of length L marked by the dash-dotted rectangle.

shape of these contacts is designed in such a way as to obtain two single-mode plasmonic slot waveguides between them. As shown in Fig. 4.7, which is a *y*-cut with *y* corresponding to the middle of the slot, the plasmonic slot waveguide having width w_2 is denoted as the *I/O slot*, since it is connected to two dielectric (photonic) waveguides, from which the input signal is provided (left) and the output signal is extracted (right) at the *through* port. The slot having width w_1 is referred to as the *coupled slot*, that is assumed to be matched at the output (*cross-coupled*) port.

The two slots, both having height h, are separated by a gold ridge having width d, and are designed to be parallel for the length L. The plasmonic slots are filled by the DLD-164 EO material [20, 21], having thickness h_{EO} measured from the surface of the SiO_2 layer. Table 4.1 reports the geometry parameters that are not going to be changed in this investigation. In particular, the average slot width $\bar{w} = (w_1 + w_2)/2$ is chosen as 100 nm (following [12, 41, 55, 62]) in order to obtain a strong EO effect already at low applied voltage while keeping the structure feasible from a fabrication standpoint, and h has been designed to be 220 nm to guarantee that each slot, considered individually, exhibits only the fundamental plasmonic mode along the vertical direction.

As already suggested in the simulation study [63] for a different coupled-slot plasmonic modulator structure, the device in Fig. 4.7 can be properly designed to

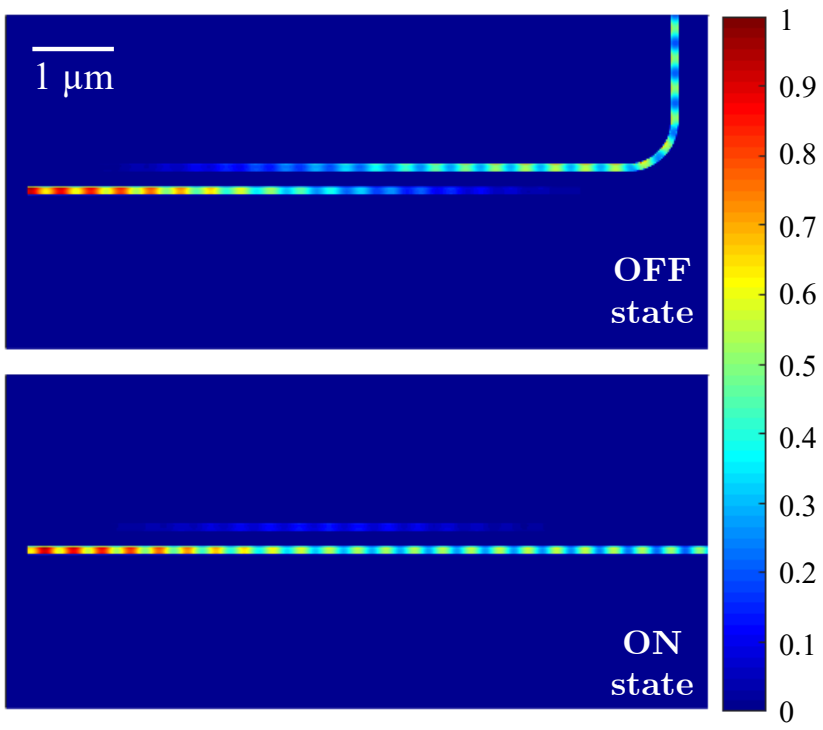

Fig. 4.8 Squared magnitude of the optical electric field (in arbitrary units, where blue corresponds to zero field), for the xz top view for y corresponding to the slot center, of a symmetric PDC modulator simulated with 3D-FDTD. The top and bottom plots are obtained in the OFF and ON states, respectively. For a cross-coupling modulator configuration, the OFF and ON states will be exchanged.

operate as an EO amplitude modulator. To demonstrate its principle, Fig. 4.8 presents the squared magnitude of the electric field for an example of a properly designed modulator, simulated with the 3D FDTD, in OFF (top) and ON (bottom) conditions. The two conditions differ due to the variation of the slot refractive index induced by the input voltage V_{in}, defined as the sum of the DC bias point V_{DC} and the RF signal V_{RF}, which controls the slot coupling. At V_{OFF}, all the input power is coupled to the *coupled slot*, thus extinguishing the power in the output section of the *I/O slot*. For the same modulator, Fig. 4.9 reports the electro-optic response, evaluated as the of output-to-input power ratio at the modulator *through* output port. The figure reports two curves, which have been obtained with two different choices of the I/O terminations in the 3D-FDTD simulation. The blue curve is obtained simulating the entire device, including a silicon input waveguide, with x- and y-widths $W_x = 450$ nm, $W_y = 200$ nm, and photonic-plasmonic converters (PPCs) consisting in triangular tapers extended 200 nm in the z direction and designed in such a way as to keep a

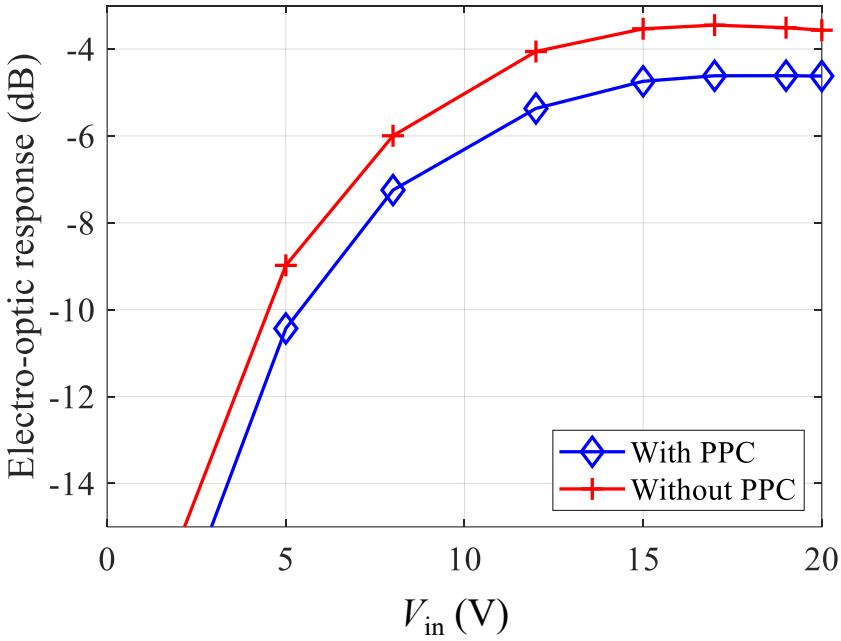

Fig. 4.9 Normalized EO response of the PDC2 modulator of Fig. 4.8. The blue and red curves are obtained with two different sets of 3D-FDTD simulations including and neglecting the PPC section, respectively (details in the text).

constant distance of 50 nm from the corresponding oblique taper in the dielectric waveguide [56]. The red curve is obtained launching directly the plasmonic mode into the input of the plasmonic *I/O slot* and measuring the power at its output, *i.e.*, neglecting the PPC section and the corresponding losses. It is to be noted that the blue and red curves are almost parallel in logarithmic scales, suggesting that the overall (input and output) coupling losses amount to ≈ 1 dB.

For a symmetric PDC2 modulator, as in the case of Fig. 4.9, the OFF state, corresponding to maximum coupling, is achieved at $V_{OFF} = 0$, provided that the length L is chosen properly. Conversely, at V_{ON}, coupling to the *coupled slot* is suppressed due to the refractive index asymmetry induced by the applied field, and the power remains in the *I/O slot*, thus reaching its output section (ON state). An asymmetric design allows to shift, virtually without any change, the EO response along the input voltage axis, *e.g.,* in such a way as to place the half-power state at zero input voltage. An example of EO response for a symmetric modulator is shown in Fig. 4.10; the complementarity of the through port and cross-coupled port responses is clearly visible. Contrarily to the MZ case, the EO response is not periodic in the

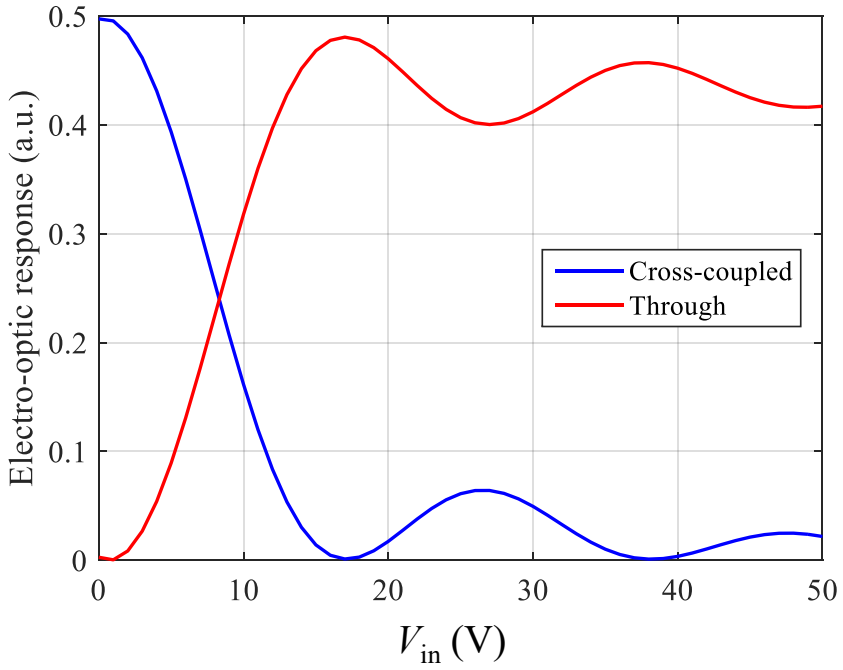

Fig. 4.10 Normalized EO response of PDC modulator for positive applied voltage: through port (red line); cross-coupled port (blue line). The modulator slot widths w_1 and w_2 are both 100 nm, with $d = 150$ nm, and length $L = 6.8\,\mu$m.

input voltage, since for $|V_{in}| > |V_{OFF}|$ coupling is increasingly suppressed, leading to ripples in the response only.

The modulation principle of this device is therefore completely different from that of the plasmonic MZ modulator described in the previous chapter. In such modulators, a two-slot plasmonic waveguide is excited with an even input optical field. If the structure is symmetrical and no voltage is applied, the even-mode excitation travels to the output combiner, where positive interference allows for the excitation of the output Si photonic waveguide (ON state). The ON-state insertion loss (IL) is due to both the attenuation of the plasmonic mode and to the coupling losses of the input divider and the output combiner.

At an applied voltage equal to V_π, the phase difference between the fields excited into the two MZ slots leads, in the output combiner, to destructive interference, *i.e.,* to the OFF state with (ideally) zero output optical power. However, the ON/OFF power ratio (extinction ratio, ER) is affected both by the slot asymmetry (that can be useful in shifting the half-power bias value to zero bias, see [12], but may lead to a different optical power being carried by the two slots), and by the coupling

between the two slots. A laterally compact design like the one in [12, 41], with a comparatively narrow ridge between the two slots, leads to modal coupling and to a decrease of the ER, as discussed in [17, Sec. 3.2]. Notice that the effect of mode coupling is always present, also in a MZ with symmetrical slots. In fact, while for zero applied voltage the structure is strictly symmetrical and the coupled slots host an even and an odd mode, only the even one being excited at the MZ input, the application of an input voltage causes the refractive index of the EO material to be different in the two slots, thus leading to an increased mode localization in each slot, and therefore to quasi-even and quasi-odd mode input excitation. As a result, in the OFF state the input even excitation can be decomposed in two modes whose superposition at the modulator output slots includes an odd part (to be radiated at the combiner) but also an even part (that is transmitted to the output photonic waveguide). Under this respect, slot coupling, while allowing for a more compact layout of the modulator, leads in principle to a worse ER. Decreasing coupling, as done in the wide-ridge layout in [55],[1] allows for an improvement of the ER but at the same time increases the length and therefore the losses in the splitter and combiner. Representative values for such coupling losses can be found in [41, Fig. 11], where two splitter and combiner solutions are discussed for slots separated by a narrow ridge, with loss of approximately 3 dB and 1 dB, respectively (leading to a total coupling loss of 6 dB and 2 dB), while in [55], where a wide ridge is introduced separating the two slots, the losses in feeding waveguides and PPCs are estimated as 3 dB. Conversely, as already mentioned, 3D simulated values of total PPC losses for the PDC modulator are as low as 1 dB.

With respect to MZ solutions, coupled-slot based modulators follow a different design criterion, since slot coupling is essential for their operation, and therefore a laterally-compact layout is indispensable. Moreover, they may achieve a better output signal extinction in the OFF state, which is not negatively affected by slot asymmetry, and exploit a simpler input and output PPC structure. The simulation study presented in the following sections aims at presenting design criteria for the PDC EO modulator, with result that support the above preliminary conclusions.

[1] In [12] an experimental value ER $= 6$ dB for a ± 3 V swing is reported for a narrow-ridge asymmetric slot MZ [12] while in [55] a DC ER > 25 dB is quoted for a wide-ridge symmetric MZ.

Table 4.1 Fixed geometrical parameters.

Quantity	$\overline{w}$	h	h_{EO}
Value, unit	100 nm	220 nm	300 nm

4.2.1 Modeling strategy

To model the EO response of PDC2 modulators, two simulation steps are required for each V_{in}. The first is the evaluation of the modulating field, which changes the optical dielectric permittivity of the electro-optic material. In the calculations presented $r = 180$ pm/V is used [21]; in RF simulations, Au is treated as an impedance boundary condition, with conductivity $\sigma_{Au,RF} = 410$ kS/cm [64]. The second step requires to perform an optical simulation of the modulator, including the voltage-dependent Δn_{EO} evaluated according to equation (2.43). The voltage-dependent modulator EO response is then evaluated as a post-processing of the optical simulation.

As suggested by Fig. 4.9, the PPC losses do not depend significantly on V_{in}, hence they can be included *a posteriori*. Moreover, mode coupling, which is at the basis of the PDC modulation mechanism, only occurs when the slot waveguides are parallel, *i.e.,* in the length L indicated in Fig. 4.7. It is therefore possible to reduce the problem to a 2D problem. The results presented here after have been obtained following this strategy. First, this requires to neglect the z-dependence in (2.41), which, however, could arise only from second-order effects such as fluctuations of the slot width/height. Under this assumption, the RF field can be evaluated in the xy cross-section through a 2D solver [42]. As an example, the top panel of Fig. 4.11 reports the x-component, which is dominating in the slot, of the simulated RF field profile for a geometry with $w_1 = w_2 = 100$ nm, spaced by $d = 100$ nm. It is to be remarked that, inside the slots, the simulations fit quite well the approximate formula $E_x = V_{in}/w$, w being the slot width. This result is used to evaluate $\Delta n_{EO}(V_{in}, x, y)$ and finally used as an input of the 2D optical FDE solver [16]. The center and bottom panels of Fig. 4.11 report, for the same device of the top panel and in the case $V_{\text{in}} = 0$, the real part of the x-components of the optical mode field profiles, which, in this case, are odd and even, respectively. The imaginary part, not reported here, exhibits the same behavior. The figure allows to appreciate how, thanks to the localized nature of the plasmonic modes, the overlap with the RF field is excellent, maximizing the electro-optic interaction. The numerical approaches in [42] and [16] have been implemented in MATLAB [65]. First, the RF field is evaluated on

proper RF discretization mesh, and $\Delta n_{EO}(x,y)$ derived from (2.43) and (2.41) is interpolated on a denser (optical) mesh required to accurately compute the plasmonic modes. All simulations presented in this section, except the ones in Figs. 4.8 and 4.9, have been performed with this modeling strategy.

In addition to the plasmonic mode profiles, the optical simulations allow to evaluate the complex propagation constants $k_i = \beta_i - \mathrm{j}\alpha_i$, $\beta_i = k_0 n_{effi}$ and α_i being the propagation and attenuation constants for the i-th mode ($i = 1$ or 2), and the corresponding voltage-dependent mode profiles $|V_i\rangle$. The idea is to express the input field of the modulator, $|I\rangle$, as a linear combination of the voltage-dependent plasmonic modes. In coupler modulators, $|I\rangle$ is the mode of the *I/O* waveguide considered as isolated from the rest of the device. So, we have

$$|I\rangle = c_1^{(\mathrm{I})} |V_1\rangle + c_2^{(\mathrm{I})} |V_2\rangle , \tag{4.2}$$

where the coefficients $c_i^{(\mathrm{I})}$ of the linear combination can be evaluated through the projection-based method described in Appendix C. Having expressed the input field in terms of the natural modes of the cross-section, the field at the modulator end, $|O\rangle$, can be evaluated by propagating the coefficients with the appropriate complex propagation constants:

$$|O\rangle = c_1^{(\mathrm{I})} \exp(-\mathrm{j}k_1 L) |V_1\rangle + c_2^{(\mathrm{I})} \exp(-\mathrm{j}k_2 L) |V_2\rangle . \tag{4.3}$$

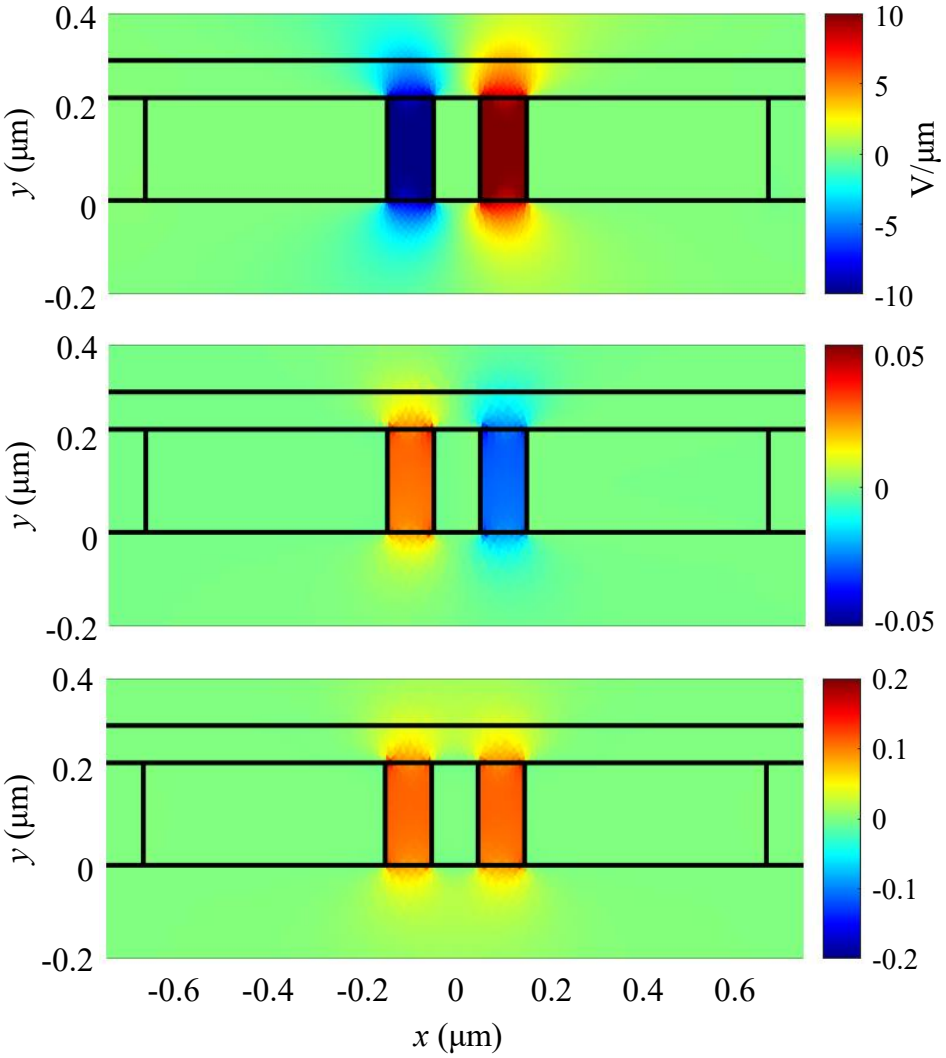

Fig. 4.11 Examples of x-components of electric field profiles. The top panel reports the RF electric field (units V/μm) for $V_{in} = 1$ V. The center and bottom panels report the real parts of the odd and even optical mode profiles (arbitrary units), respectively.

Considering that the input and output sections of the modulator have the same cross section, the modulator response can be evaluated as the fraction of $|O\rangle$ overlapping with the input field $|I\rangle$. In particular, through another projection, $|O\rangle$ can be represented as

$$|O\rangle = c_1^{(\mathrm{O})} |I\rangle + c_2^{(\mathrm{O})} |C\rangle , \tag{4.4}$$

where $|C\rangle$ indicates the mode of the *coupled slot* waveguide shown in Fig. 4.7 but considered isolated from the rest of the device. We may note that this approach, described here for PDC modulators, applies also to MZ modulators. The only

difference is that, in MZ modulators, the splitter excites the two slots in the same measure, so that $|I\rangle$ and $|C\rangle$ are quasi-even and quasi-odd modes (including possible slot asymmetries). Then, the output response has the physical meaning of the even fraction of $|O\rangle$, that is the only part that is not radiated after reaching the output combiner.

4.2.2 Symmetric and asymmetric modulators

Having already fixed the height and the average width of the slots, the remaining design parameters for the cross-section are the asymmetry between the slot widths, $\Delta w = w_2 - w_1$, and the width of the ridge, d, which separates the slots. As a first investigation, in Fig. 4.12 we present the voltage-dependent effective refractive indices, $n_{\text{eff}1,2}(V_{\text{in}})$, resulting from two groups of parametric simulations.

In particular, Fig. 4.12(a) reports the results of a symmetric modulator, *i.e.,* $\Delta w = 0$, for different ridge widths. All curves show similar trends. For $V_{\text{in}} \to 0$, they exhibit stationary points. These are a signature of coupling between the two waveguide modes. Indeed, in absence of mode coupling, the curves would be perfectly straight lines and cross at 0 V. Instead, the linear behaviour appears only for larger voltages, where the two n_{eff} exhibit linear asymptotes. The ridge width d impacts the mode coupling strength: for small d the slots are closer, hence more coupled, as indicated by the larger $\Delta n_{\text{eff}}(0) = n_{\text{eff}1}(0) - n_{\text{eff}2}(0)$. Instead, for distant slots, the effective indices reach the linear regime even for very small voltages. Fig. 4.12(b) reports the results of simulations performed with $d = 300\,\text{nm}$, for different width asymmetries. The only effect of the asymmetry appears to be a translation of the curves on the V_{in} axis proportional to Δw, with no visible impact on the mode coupling strength.

By inspecting Fig. 4.8, it is clear that, in these devices, the extinction mechanism is based on mode coupling. In this view, it it possible to define the OFF state voltage V_{OFF} as the state where $\Delta n_{\text{eff}}(V_{\text{OFF}})$ is minimum. This is represented in Fig. 4.13(a), which reports $V_{\text{OFF}}(\Delta w)$. The curve is a straight line, further demonstrating the proportionality of the horizontal shift of the curves of Fig. 4.12(b) to Δw. This plot presents also a green shading, which corresponds to varying the ridge width d as a parameter: this shows that V_{OFF} exhibits a weak dependence on it. In this view, Δw can be chosen according to the targeted OFF-state voltage.

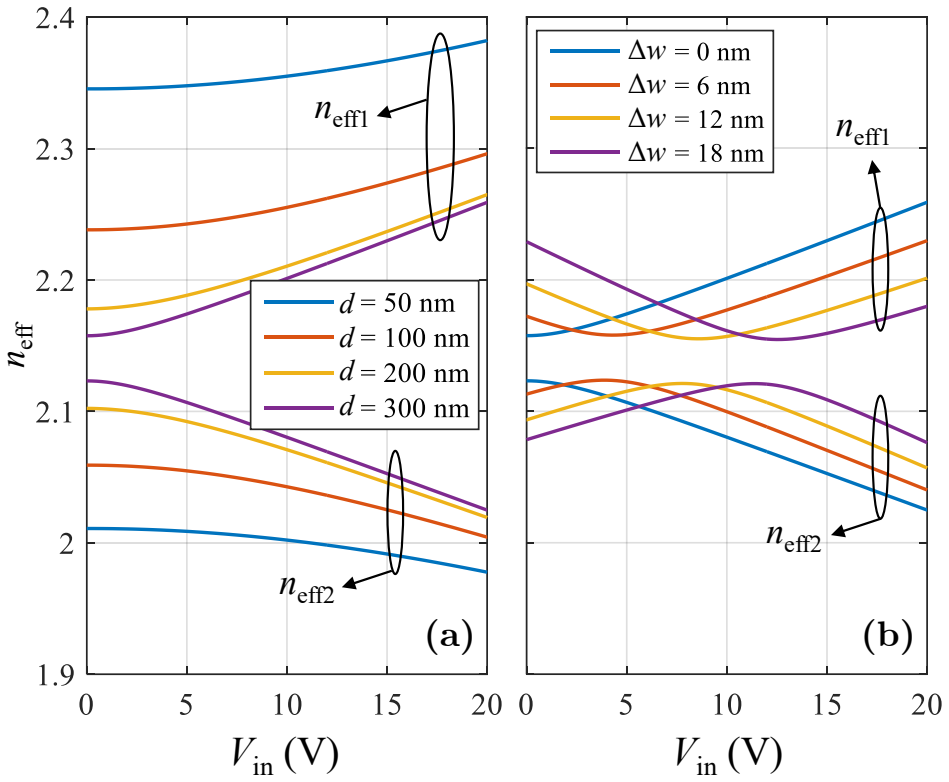

Fig. 4.12 Voltage-dependent effective refractive indices. Each pair of top and bottom curve with the same color indicates n_{eff1} and n_{eff2}, respectively. The left (a) panel results from a parametric investigation for fixed slot asymmetry $\Delta w = 0$ and changing the ridge width d. The right (b) panel is obtained results from a parametric investigation for fixed $d = 300\,\text{nm}$ ridge width and changing the slot asymmetry Δw.

There are two parameters left to complete the modulator design: the ridge width d, and the modulator length L. However, the two parameters are related, as the red curve in Fig. 4.13(b) clearly suggests. This behaviour can be better understood by considering the modal field distributions in the coupled slots. To this aim, Fig. 4.14 shows cuts, at y corresponding to the slot center, of $|V_1\rangle$, $|V_2\rangle$, $|I\rangle$, and $|O\rangle$, for a symmetric modulator with $d = 150\,\text{nm}$, at $V_{\text{in}} = 0$, where mode coupling is strongest (so that $V_{\text{OFF}} = 0$). The $|V_1\rangle$ and $|V_2\rangle$ plots in Fig. 4.14 stress another signature of mode coupling, *i.e.,* the fact that the mode profiles at $V_{\text{in}} = 0$ are odd ($|V_1\rangle$) and even ($|V_2\rangle$). (On the other hand, for large V_{in}, it could be seen that the mode profiles tend to be localized in either slot.) These modes are sorted in decreasing order by their energy, $|V_1\rangle$ being the mode with larger effective refractive index. From a careful inspection of the top-right panel of Fig. 4.14, one could notice a small spurious field in the left waveguide. This is related to the fact that the coefficients $c_i^{(\text{I})}$ of the linear

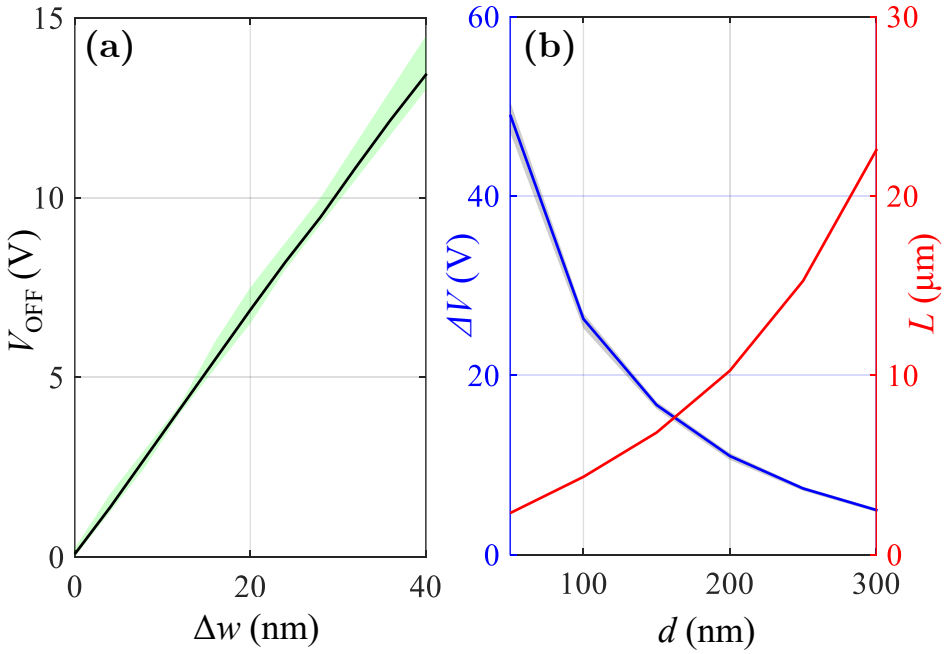

Fig. 4.13 Design plots for coupler modulators. Left (a) panel: OFF state voltage V_{OFF} versus the slot asymmetry Δw; the green shading indicates the sensitivity of V_{OFF} to the ridge width d, varied in the range $[50 \div 300]$ nm. Right (b) panel: ON-OFF state swing ΔV (blue curve and shading) and L (red curve and shading) versus d, varying Δw as a parameter in the range $[0 \div 40]$ nm. The red shading is almost invisible, demonstrating the very weak dependence of L on the slot asymmetry.

combination defining $|I\rangle$ in (4.2) are obtained with a 2×2 least-squares optimization performed over the entire cross-section (see Appendix C), so minor local errors are in order. The very low ER achievable with this method (see, *e.g.,* Figs. 4.9 and 4.15) suggests that this artifact should not affect significantly the predictions.

On the top-right panel $|I\rangle$ is reported, represented as a linear combination of $|V_1\rangle$ and $|V_2\rangle$ as in (4.2). Due to the aforementioned symmetries, it is understood that $|I\rangle$ excites $|V_1\rangle$ and $|V_2\rangle$ with the same magnitude. At the output section, *i.e.,* after the two modes propagate for a length L, the relative phase-shift:

$$\Delta\phi(V_{in}) = k_0 L \Delta n_{eff}(V_{in}), \tag{4.5}$$

is introduced. If $\Delta\phi(V_{OFF}) = \pi$, then, at the output section, the excitation coefficients have opposite sign with respect to the input section, leading to a field localized in the left slot only. This is the case of the bottom-right plot of Fig. 4.14, resulting in a

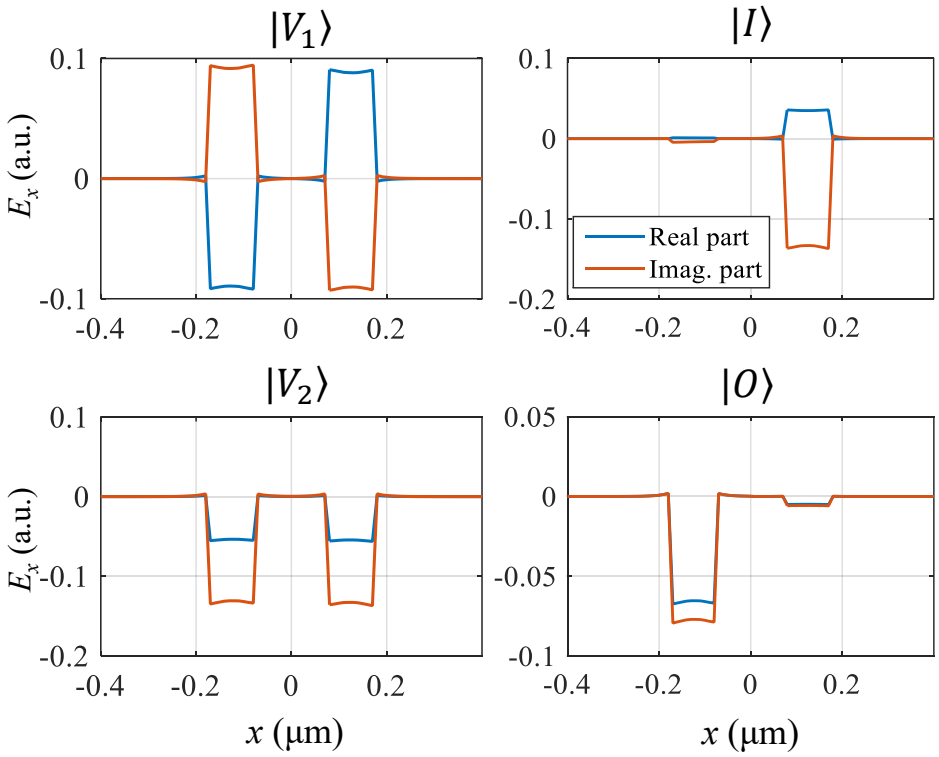

Fig. 4.14 Cuts of the optical field component E_x performed at y corresponding to the slot center, of the waveguide modes $|V_1\rangle$ and $|V_2\rangle$, input field $|I\rangle$, and output field $|O\rangle$, for a symmetric modulator with $d = 150\,\text{nm}$ and $L = 6.8\,\mu\text{m}$ at the OFF state voltage $V_{\text{in}} = 0$. Blue and red curves indicate the real and imaginary parts of the field profiles. The small spurious field in the left waveguide is indeed a numerical artifact; it has been verified that it does not affect the final results.

modulator length designed as

$$L = \frac{\pi}{k_0 L \Delta n_{\text{eff}}(V_{\text{OFF}})}. \tag{4.6}$$

With the data in Fig. 4.14, we obtain $L = 6.8\,\mu\text{m}$. Obviously, the L value in (4.6) could be generalized using an odd multiple of π, *i.e.,* $(2n+1)\pi$, but this choice is not convenient, since it would lead to longer modulators and to higher ON-state losses.

Equation (4.6) allows to obtain the relation $L(V_{\text{OFF}})$ shown in Fig. 4.13(b). Just like the left panel, this is a parametric plot on Δw; yet, the impact of Δw is negligible. Fig. 4.13(b) also includes (blue curve), the voltage swing required $\Delta V = |V_{\text{ON}} - V_{\text{OFF}}|$. V_{ON} is defined as the voltage at which the modes excited in the input section recombine in phase at the output section, *i.e.,* such that the phase shift (4.5) is equal

to 2π (notice that the definition is not critical, since for $|V_{\text{in}}| > |V_{\text{ON}}|$ the modulator practically remains in the ON state). Also in this case, the dependence on the parameter Δw (shown as a blue shading) is quite weak. This demonstrates that Δw and d are virtually orthogonal in determining V_{OFF} and the set $[\Delta V, L]$, respectively. The opposite trends of ΔV and L vs. d in Fig. 4.13(b) suggest that the design results from a trade-off. Indeed, modulators with strong mode coupling (small d) are characterized by large $\Delta n_{\text{eff}}(V_{\text{OFF}})$, but also by a weaker dependence of $\Delta n_{\text{eff}}(V_{\text{in}})$. This has a positive impact on L, which can be shorter, but results also in a larger ΔV.

As discussed at the end of Section 4.2.1, the modulator EO response simply is the coefficient $c_1^{(\text{O})}$ from (4.4). As an example, Fig. 4.15 reports the EO response of the symmetric modulator presented in Fig. 4.14. From the blue curve, the insertion loss (IL, about 4 dB) can be obtained as the EO response at the ON state, corresponding to a voltage 15 V; the computed ER (*i.e.,* the ratio of the OFF and ON responses, the former occurring at $V_{\text{in}} = V_{\text{OFF}} = 0$ V) is in excess of 25 dB. On the other hand, it can be shown (by means of calculations similar to those described in Sec. 4.2.1) that the ER of a POH MZ modulator varies almost linearly from 0 dB to 25 dB for d increasing from 100 nm to 500 nm (the upper limit of this interval is consistent with the value $d = 410$ nm reported in [12, Table S 1]). Indeed, as discussed in [17, Sec. 3.3], mode coupling is a detrimental effect in MZ modulators, impacting in particular on the ER, while the PDC modulator shows a computed ER well in excess of 25 dB on the whole d interval.

The EO response has been simulated over a broad V_{in} range (extending well beyond $|V_{\text{ON}}|$) to emphasize some peculiar features of PDC modulators. This is shown in the inset of Fig. 4.15. As already noticed, contrarily to the MZ modulator whose EO response is periodic, only one ON state is present, with two OFF states corresponding to $V_{\text{OFF}} \pm \Delta V$. Indeed, the extinction mechanism of PDC modulators is based on mode coupling, which is strong only at V_{OFF}; for $|V_{\text{in}}| > |V_{\text{OFF}} \pm \Delta V|$, the field profiles are increasingly localized in the slots and no stationary points are encountered in the $n_{\text{eff}i}(V_{\text{in}})$ characteristics. However, since complete mode localization is only achieved for $V_{\text{in}} \to \infty$, implying that the PDC is in the ON state independent on the device length L, for finite L response maxima still imply a constructive interference of the even and odd mode components, which only occurs, for a given L, at specific values of V_{in}. The increase in localization with increasing V_{in} leads to a decrease of the amplitude in the response ripples. Finally, notice that, for the symmetric device, the maximum applied voltage is of the order of 20 V,

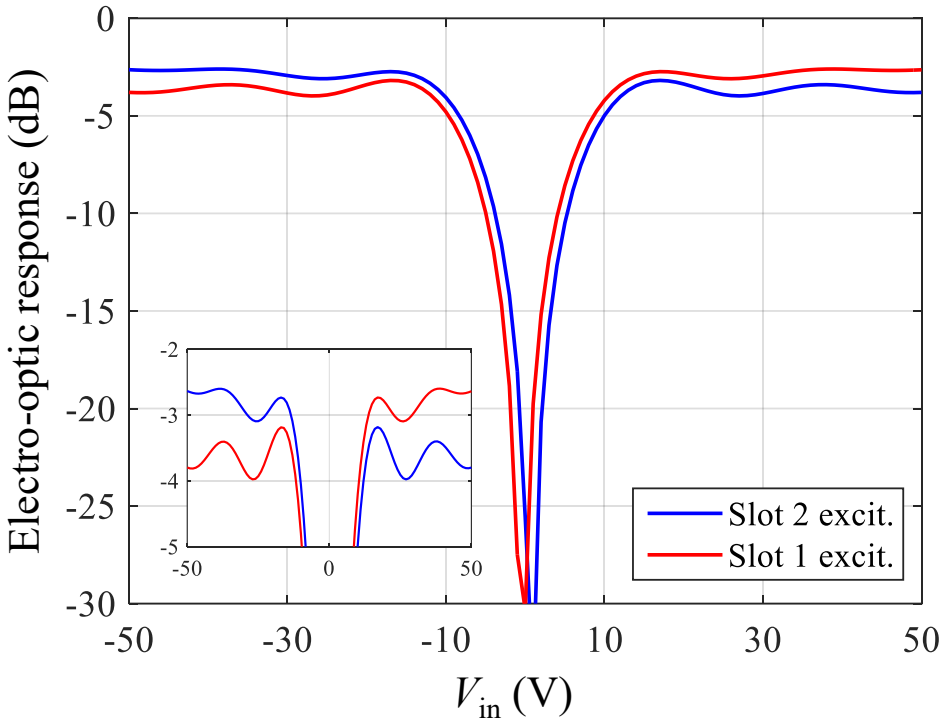

Fig. 4.15 EO response of the symmetric PDC modulator of Fig. 4.14 ($d = 150\,\text{nm}$, $\Delta w = 0$, $L = 6.8\,\mu\text{m}$), evaluated as the coefficient $c_1^{(\text{O})}$ from (4.4). The blue curve refers to the same excitation scheme of Fig. 4.14. The red curve is obtained exciting the left slot, *i.e.,* by exchanging the *I/O* and *coupled* slots.

corresponding to a maximum field in the DLD-164 polymer of the order of 200 V/μm, still compatible with the material breakdown field, which exceeds 250 V/μm in DC, see [25, Fig. 2]. The V_{ON} and V_{OFF} ranges discussed here are also compatible with those of experimentally realized POH MZ modulators [12, 41]. Moreover, an asymmetric coupler design allows to shift to $V_{\text{DC}} = 0$ the half-amplitude bias point, thus reducing by a factor of 2 the maximum electric field in the slot.

Another peculiarity of PDC modulators are the asymmetries arising for $V_{\text{in}} \gtrless V_{\text{OFF}}$. Consider for instance the blue curve in Fig. 4.15, corresponding to excitation in the right slot as presented in Fig. 4.14: the IL for $V_{\text{in}} > V_{\text{OFF}}$ is about 1 dB larger than that for $V_{\text{in}} < V_{\text{OFF}}$. Even if the slots are symmetric, *i.e.,* $\Delta w = 0$, the device is not symmetric due to the fact that one slot only is excited at the input. In this view, positive or negative voltages lead to opposite EO effect, leading to different group velocity, losses and mode profiles. The red curve, corresponding to left-slot

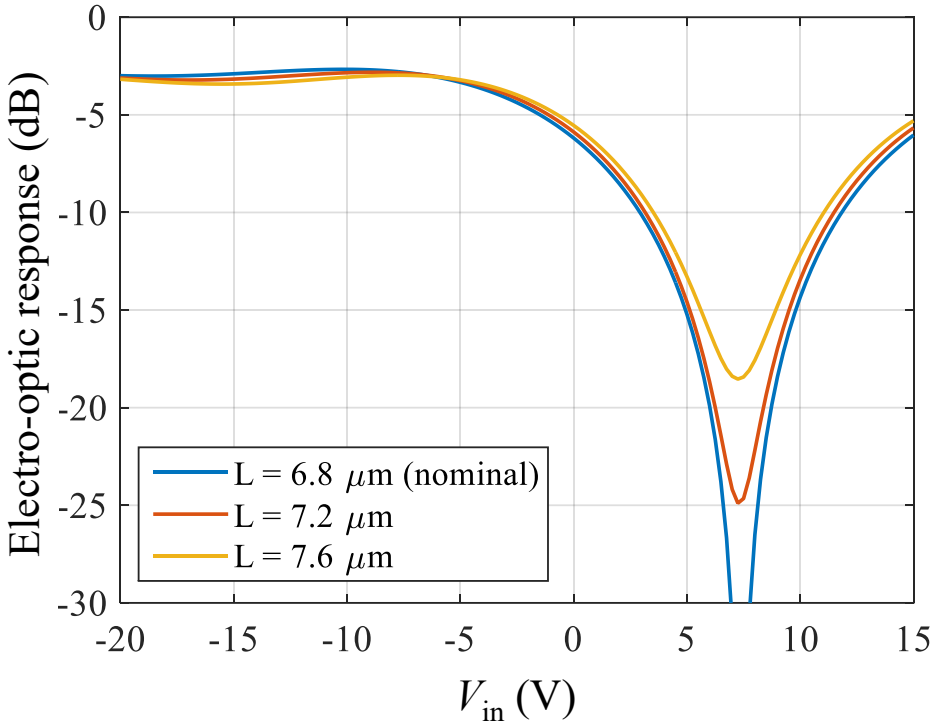

Fig. 4.16 EO response of the coupler modulator with $d = 150\,\text{nm}$ and $\Delta w = 20\,\text{nm}$, for different length L. The solid blue curve, referring to $L = 6.8\,\mu\text{m}$, is the reference design following (4.6).

excitation, exhibits an opposite behaviour. This points out that there is an optimum excited slot, to be chosen coherently with the modulator bias voltage.

4.2.3 Parametric sensitivity and optical bandwidth

In MZ modulators, extinction is obtained through destructive interference at the output of the phase shifters, and the $V_\pi L$ product depends on the cross-section geometrical parameters. This implies that the OFF state can be always obtained (albeit with non-ideal extinction), independent of L, with a suitable V_π. On the other hand, in PDC modulators, L has to be designed according to (4.6) and/or Fig. 4.13(b) to have extinction at a certain V_{OFF}.

To assess to which extent this design constraint is critical vs. variations of the modulator geometry, Fig. 4.16 presents the results of an investigation versus the parameter L. (Notice that, since the modulator length L depends on the design wavelength, the performance sensitivity with respect to L also is a limiting factor

for the optical bandwidth.) The analysis has been performed on a modulator with $d = 150\,\text{nm}$, targeted to be similar, in terms of mode coupling (hence, with the same L), to that presented in the previous section, but with a slot asymmetry $\Delta w = 20\,\text{nm}$. This choice of parameters sets the half-power point in $V_{\text{in}} = 0\,\text{V}$: the IL is about 3 dB, and the half-power bias point (corresponding to $\approx -6\,\text{dB}$ level) is at about 0 V. This is consistent with Fig. 4.13, since this choice leads to $V_{\text{OFF}} \approx 8\,\text{V}$ and $\Delta V \approx 16\,\text{V}$, the half-power point being approximately midway the OFF and ON voltages. This allows to design the PDC bias around the quadrature point (where linearity is maximum) at zero bias voltage, so that the ON-OFF condition can be reached with a halved V_{in}, with consequent advantages in terms of energy-per-bit, stability of the polymer (due to the reduced maximum field) but also simplicity of the driving electronics (since $V_{\text{DC}} = 0$ no bias-T is required). Fig. 4.16 suggests that the exact value of L is not very critical, since $-22\,\text{dB}$ levels are still possible with $\pm 400\,\text{nm}$ variations with respect to the nominal length $L = 6.8\,\mu\text{m}$ (it has been verified that similar results hold for shorter L, *i.e.*, $L = 6.4\,\mu\text{m}$ and $L = 6.0\,\mu\text{m}$).

Fabrication issues may also affect the width and height of the plasmonic slots [21]. For the widths, [55] indicates that the lateral uncertainty is $\pm 10\,\text{nm}$. Such fluctuations could either introduce asymmetries between the two slot widths, or change both widths in the same way. For the former case, Fig. 4.13 demonstrates that a slot asymmetry leads only to a change of V_{OFF}, without requiring to re-design L. This is also clear from Figs. 4.15 and 4.16, which are obtained for designs differing only for Δw. Figure 4.17 presents a sensitivity analysis for fluctuations in w_1 and w_2 having the same value (dash-dotted lines). It is apparent that, with respect to the reference device (solid blue curve), this case does not lead to any appreciable difference. Indeed, even if n_{eff1} and n_{eff2} change, their difference is almost constant in the strong mode coupling regime (*i.e.*, for V_{in} close to the V_{OFF}), at least for small variations in the individual slot widths. The dashed curves of Fig. 4.17 finally report an investigation of the sensitivity of the EO modulator response with respect to h. This suggests that this parameter does affect the ER of the device, which could be ascribed to a change of Δn_{eff}, so that the nominal L does not longer guarantee $\Delta\phi = \pi$ at the designed V_{OFF}. For a ± 10 nm variation, however, an ER in excess of 20 dB is anyway obtained.

Changes in the operating wavelength vs. the nominal (design) value lead to a variation of the L/λ ratio, with effects, as already stressed, similar to a variation in L, but also to a variation of the effective index in the plasmonic mode. The analysis

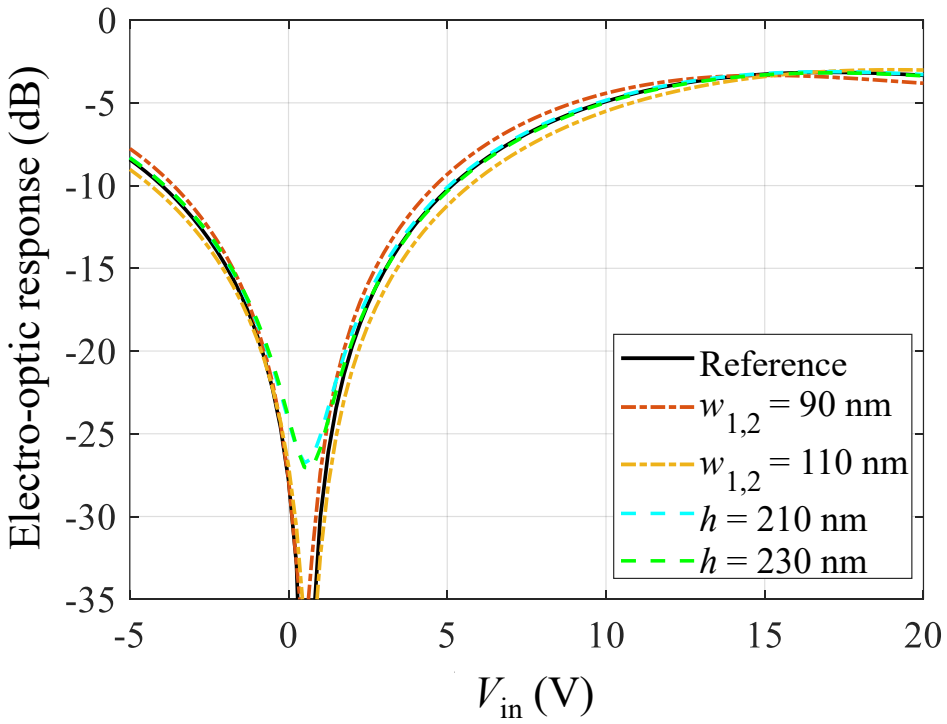

Fig. 4.17 Sensitivity investigations of the EO response of the symmetric PDC modulator of Fig. 4.14 ($d = 150$ nm, $\Delta w = 0$, $L = 6.8\,\mu$m) to $w_{1,2}$ (dash-dotted curves) and h (dashed curves). The dash-dotted curves are obtained for $w_1 = w_2$. The response of the nominal device is reported with the solid black curve for reference.

on the sensitivity versus L already suggests that the PDC modulator does not exhibit a strongly resonant behavior (as in resonant ring modulators), corresponding to a moderately broad optical bandwidth. This is confirmed by the simulations shown in Fig. 4.18, showing that the ON state behavior is practically unaffected by varying the operating wavelength, while the ER remains in excess of 27 dB on a 100 nm optical bandwidth, and in excess of 20 dB on a 200 nm optical bandwidth. These values compare favourably with those of the POH MZ modulators, which exhibit a typical optical bandwidth in excess of 100 nm [12].

4.2.4 Modulation bandwidth and energy consumption

Since the modulator length is much smaller than the RF wavelength, even assuming THz operation, the PCM frequency response can be approximated with that of the *RC* circuit shown in the inset of Fig. 4.19, R being the device and driver total equivalent resistance and C its capacitance. It has been verified, by quasi-static

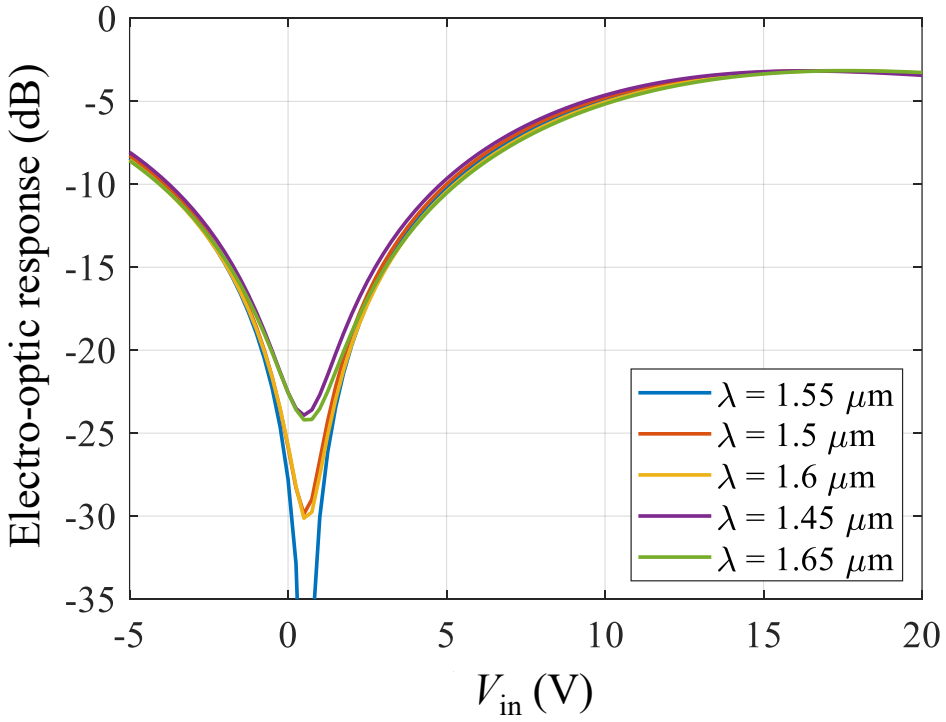

Fig. 4.18 Behaviour of the EO response for different operation wavelengths around 1550 nm for the reference structure in Fig. 4.17.

simulations [42], that the device resistance is negligible compared to the typical $R_d = 50\,\Omega$ high-frequency driver resistance, and that its capacitance is frequency-independent. More in detail, Fig. 4.19 reports a parametric study of the per-unit-length capacitance $\mathscr{C}$ (such that $C = \mathscr{C}L$) of PDC modulators for $\Delta w \in [0,40]$ nm. These results demonstrate that $\mathscr{C}$ depends weakly on Δw, and shows a moderate increase with d in the design range.

In the parameter range investigated in this work, $\mathscr{C}$ is lower than 0.28 fF/μm. Using this as an upper bound and considering a modulator length $L = 7\,\mu$m, bounds can be estimated for the intrinsic device bandwidth and energy-per-bit consumption. Starting from the former, the intrinsic cutoff frequency $f_c = 1/(2\pi\tau)$ can be evaluated from the time constant $\tau = RC$, resulting to be about 1.6 THz (net of possible parasitic capacitances external to the device). As for the POH modulator in [12], the extrinsic device bandwidth is expected to be dominated by external parasitics. For what concerns the power consumption, it can be quantified by the energy-per-bit, which

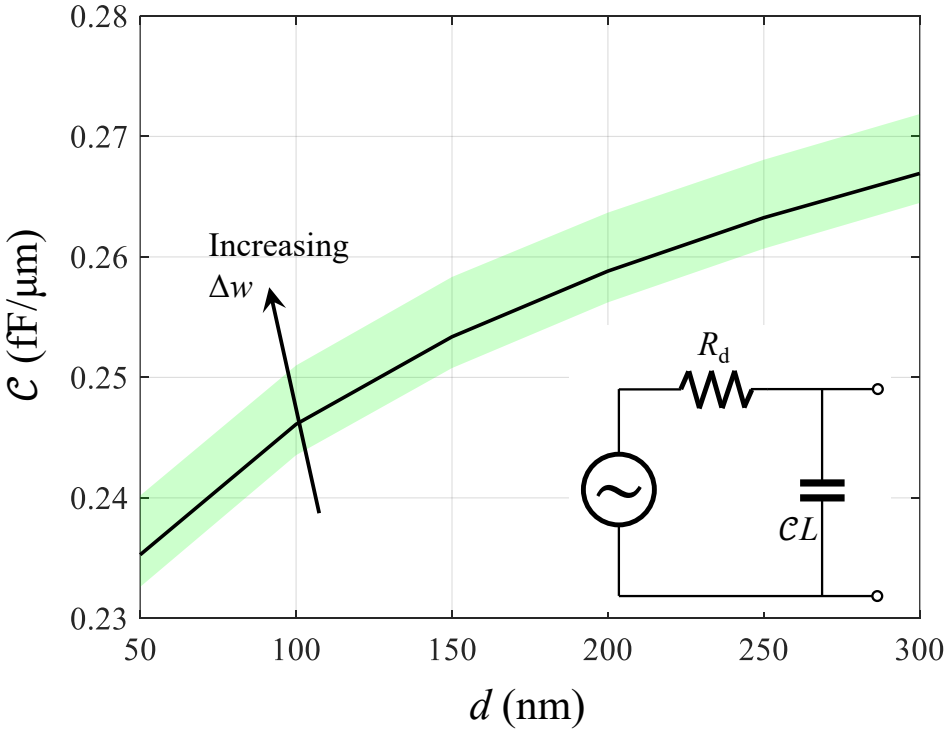

Fig. 4.19 Per-unit-length capacitance $\mathscr{C}$ of PDC modulators versus d, varying Δw as a parameter in the range $[0 \div 40]$ nm. The black curve is the average value, and the green shading indicates the sensitivity of $\mathscr{C}$ to Δw. The inset reports the *RC* circuit describing the PDC dynamics.

can be approximately estimated with the expression [66, 25]:

$$W_{\text{bit}} = \frac{1}{4} C V_{\text{RF}}^2, \tag{4.7}$$

resulting, for a $V_{\text{RF}} = \pm 3$ V peak-to-peak drive voltage swing, to be about 18 fJ/bit. This compares well with the POH MZ modulator value of 25 fJ/bit reported in [12] for the same peak-to-peak drive voltage swing.

4.2.5 Modulator chirp

The chirp performance of directional coupler based modulators is discussed in [61], where an analytical model, based on the perturbative treatment of coupling between

interacting waveguides, is provided for the Henry chirp parameter α_{H}:

$$\alpha_{\mathrm{H}}(t) = 2\frac{\dfrac{\mathrm{d}\phi(t)}{\mathrm{d}t}}{\dfrac{1}{p_{\mathrm{out}}(t)}\dfrac{\mathrm{d}p_{\mathrm{out}}(t)}{\mathrm{d}t}},$$

where $\phi(t)$ is the phase of the output optical field, $p_{\mathrm{out}}(t)$ the optical output power. In the customary bias-dependent small-signal approximation, it is:

$$\alpha_{\mathrm{H}} = 2\frac{\Delta\phi}{\dfrac{1}{P_{\mathrm{out}}}\Delta P_{\mathrm{out}}} = 2\frac{\dfrac{\Delta\phi}{\Delta V_{\mathrm{in}}}}{\dfrac{1}{P_{\mathrm{out}}}\dfrac{\Delta P_{\mathrm{out}}}{\Delta V_{\mathrm{in}}}},$$

where P_{out} is the optical output power at the modulator bias voltage V. According to [61], $\alpha_{\mathrm{H}} = 0$ identically for the cross-coupled modulator while it depends on bias for the through modulator. Values of α_{H} for the half power point in the through modulator, as shown in [61, Fig. 5], are around unity.

The numerical model presented in Sec. 4.2.1 allows for a straightforward evaluation of the small-signal α_{H}, since it directly provides the bias-dependent output field amplitude and phase both for the through output port (the one considered in the present paper, see Fig. 4.7) and the cross-coupled port. The results obtained are shown as a function of the applied voltage, for both ports, in Fig. 4.20. The PDC modulator considered is symmetrical, with $V_{\mathrm{ON}} = 0$, $V_{\mathrm{OFF}} \approx 16$ V and half-power bias around 8 V. In agreement with [61], the cross-coupled port shows very low (albeit not identically zero) chirp, while the through port α_{H} is odd with respect the bias voltage, with half-power values again around ± 1. Contrarily to MZ symmetric modulators (*e.g.,* lithium niobate X-cut modulators), where $\alpha_{\mathrm{H}} = 0$ independent on bias, see *e.g.,* [28], the present analysis confirms that PDC modulators exhibit either zero chirp (in the cross-coupled configuration) or tunable (positive or negative, according to the sign of the bias voltage) chirp, which may be interesting for dispersion compensation.

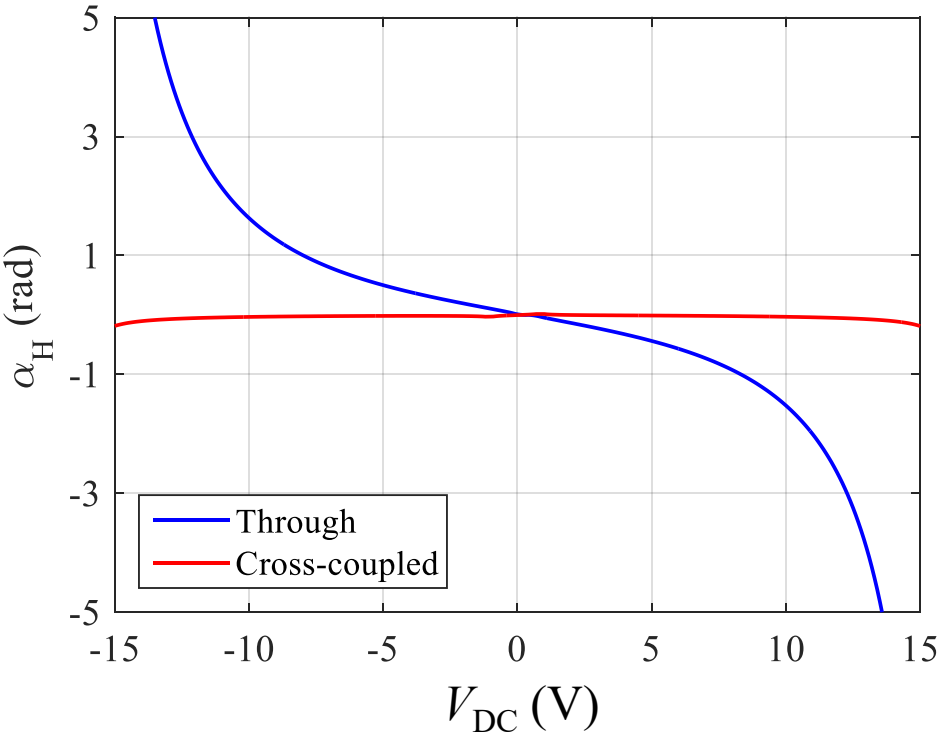

Fig. 4.20 Small-signal Henry parameter α_H as a function of the bias point for the through port (blue curve) and the cross-coupled port (red curve). The modulator geometry is that of Figs. 4.14 and 4.15.

4.3 PDC3 Modulator

The directional coupler modulator discussed so far is based on two coupled waveguides (PDC2). A similar device can be devised, based on three coupled waveguides (PDC3). In order to compare PDC2 with PDC3, by FDE method the propagating optical modes[2] are computed and shown in Fig. 4.21. The wavelength considered is 1550 nm and W is 100 nm. By applying a voltage between the signal V pad and the ground *GND* pad, the propagation constant changes. For PDC2, there are two modes with effective refractive index larger than the SiO_2 index. For the PDC3, three propagating modes exist, corresponding to globally odd and even field distributions in the coupled slots. The mode profiles of these three modes are presented in Fig. 4.22.

[2]Notice: the modes with n_{eff} higher than n_{SiO_2} are considered as propagating modes.

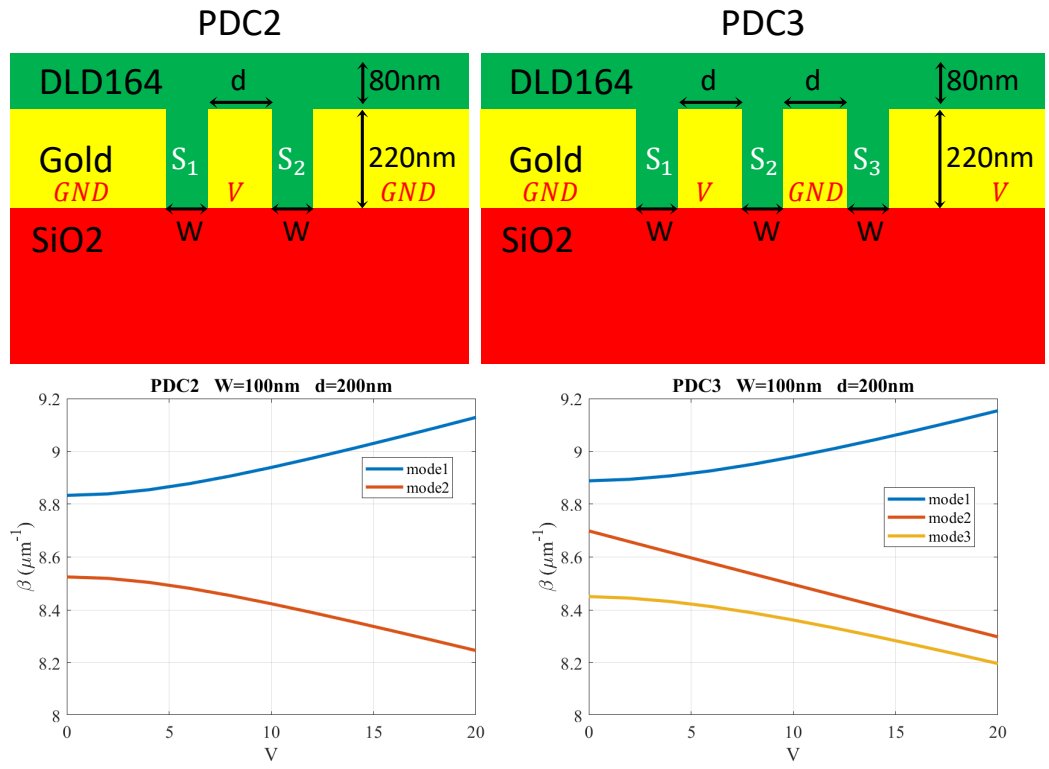

Fig. 4.21 Top: The geometry of the three-coupled slots directional coupler. Bottom: β versus applied voltage.

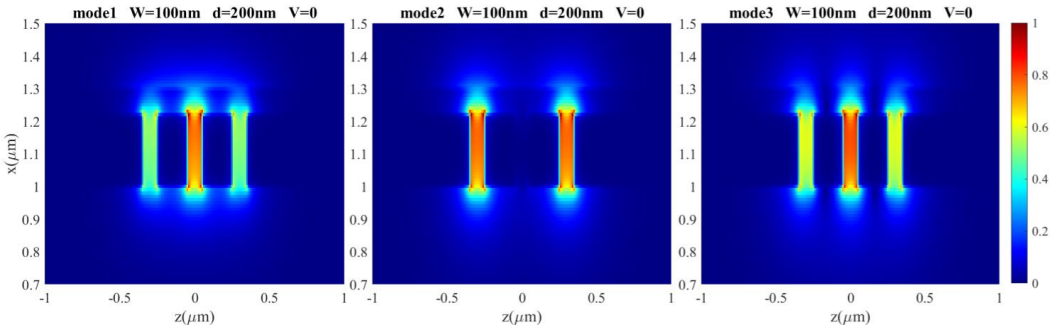

Fig. 4.22 The mode profile of propagating modes of PDC3.

If we look at the electric field resulting from the 3D-FDTD simulation along the optical path, Fig. 4.23, we can see that the coupling length L_c is smaller for PDC3 than PDC2 with the same values of d and W. This reduction is due to the presence of the middle slot waveguide, which interacts with two slots instead of one. In this way, the power in the middle slot is coupled to both sides and complete power transfer takes place sooner, thus implying a smaller coupling length L_c.

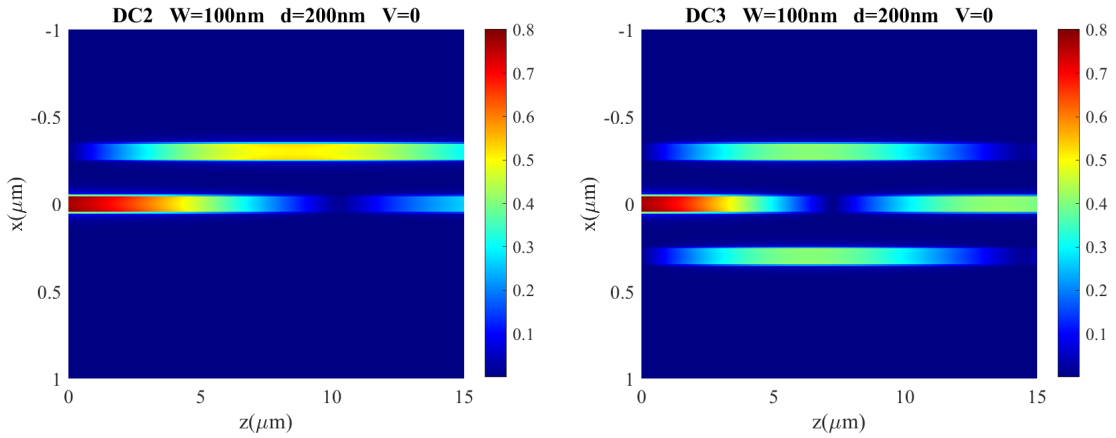

Fig. 4.23 The absolute value of electric field in PDC2 and PDC3.

4.3.1 Modeling strategy

The behavior of directional coupler can be simulated by FDTD method, which is very accurate, but very computationally intensive. In order to optimize the geometry and find the best W and d value, a faster method based on FDE are used. First, consider only the middle slot exist and then by FDE the mode profile is calculated (Fig. 4.24). After that, the modes of all slots are computed (Fig. 4.22) and by decomposing the mode profile into them, the propagation of each supported mode is estimated [9]. In this way, the simulation are 20 times faster than FDTD, with the same accuracy. Fig. 4.25 shows the normalized power in each slot versus the length and compares results from the FDE and FDTD method, showing good agreement.

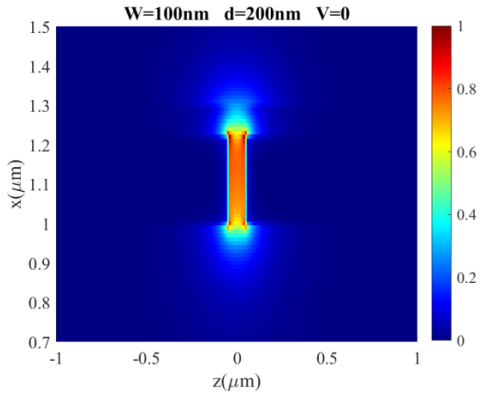

Fig. 4.24 The mode profile considering just S_2.

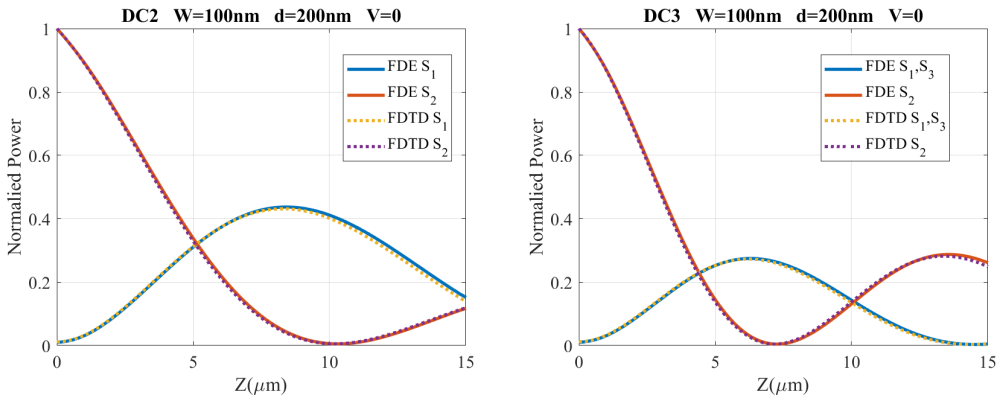

Fig. 4.25 The FDTD and FDE result comparison.

4.3.2 Proposed Geometry

Fig. 4.26 shows the proposed modulator. The optical power enters the modulator from the input Si photonic waveguide and is converted to a plasmonic mode into S_2. The optical power is then coupled to S_1 and S_3. Finally, at the end of device, the power remaining in S_2 is converted to the output Si waveguide. The device operates based on controlling the coupling length L_C. Applying a voltage, the propagation constant in DC3 is changed, thus affecting L_C. If the length of directional coupler section (L) is the same as L_C, no power remains at the end of S_2 and output waveguide. If $L = 2L_C$, the coupled power to S_1 and S_3 come back to S_2 and the power in the output waveguide is increased.

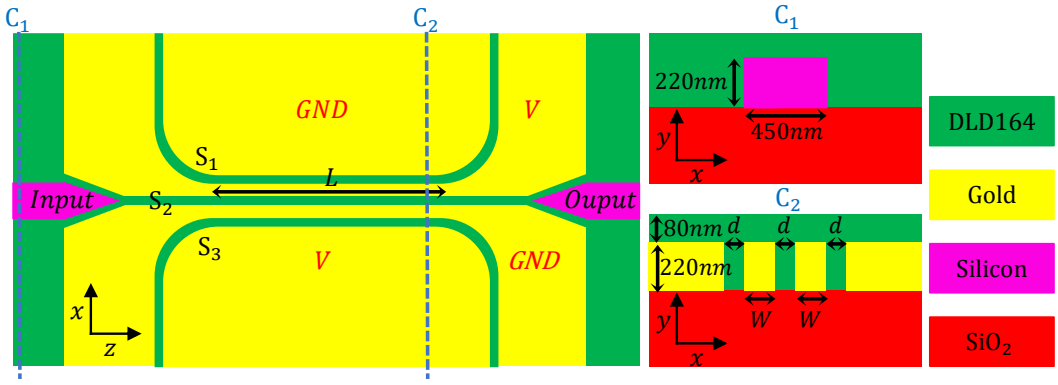

Fig. 4.26 The proposed plasmonic modulator.

4.4 Optimizing Geometry

The widths W, d and the length L are three critical parameters in the geometry. In order to find the best value for them, several simulations are done for $W = 100\,nm$ to $W = 200\,nm$ and $d = 100\,nm$ to $d = 300\,nm$ (Fig. 4.27). According to the results, in some states L_C is decreased by applying voltage which is exactly what is needed for modulation. The following formula is used to find the best state for each W and d:

$$L_C\,|_{V=0} \geq 2L_C\,|_{V=1:20} \tag{4.8}$$

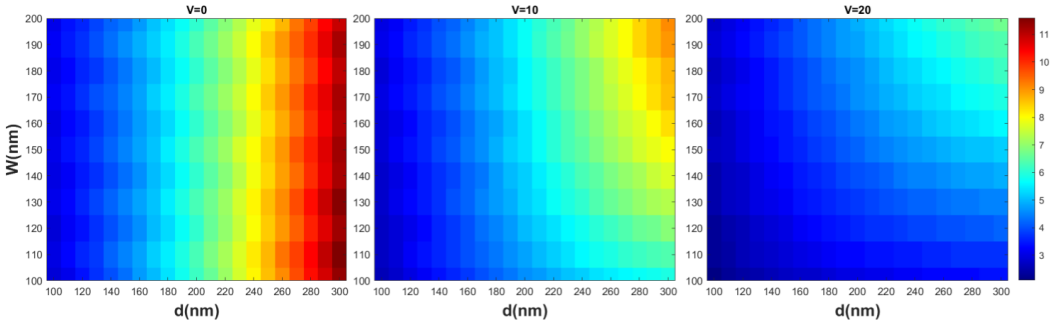

Fig. 4.27 The L_C versus W and d for different values of V.

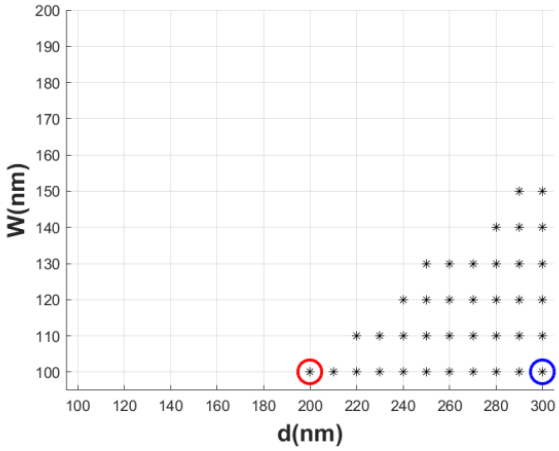

Fig. 4.28 The L_C have satisfied Eq.2 .

There are 38 states which satisfy this condition, as shown in the Fig. 4.28. Among them, one state has lowest L ($state1$) which is indicated by the red circle, and one state has lowest V_{pi} ($state2$), which is indicated by blue circle. Fig. 4.29 shows the

transmission for these two cases. The on-off voltage V_{pi} is 19 V for $state1$ and 11 V for $state2$. The extinction ratio is 18.32 dB and 8.22 dB, respectively. The optical insertion loss is 4.78 dB and 6.83 dB respectively.

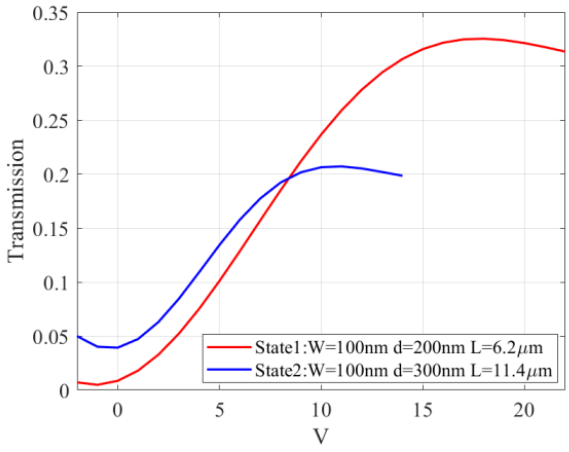

Fig. 4.29 The Transmission for $state1$ and $state2$.

Chapter 5

Conclusions and outlook

This study presents an overview of physic-based and system-oriented modeling of modulators based on plasmonic waveguides. The focus of thestudy is on two types of modulator, Mach-Zehnder and directional coupler modulators. Both of them can be implemented from plasmonic waveguides deposited on silicon substrates. The device is compatible with a silicon photonics platform and an elector-optic polymer is exploited as an active material. The polymer has Pockels effect and its refractive index is varied by the applied electric field. The proposed devices operates at 1550 nm wavelength, typical of data center or long-haul telecommunication systems.

As mentioned in chapter 2, there are several methods to simulate and analyze the behavior of plasmonic devices. For the primary investigation of modulator behavior, the finite-difference eigenmode method (FDE) and Finite Element Method (FEM) are adopted. They are waveguide-level simulation techniques, and they are quite fast (each simulation takes a couple of minutes). The more precise simulations are done by the help of Finite-Difference Time-Domain Method (FDTD). FDTD is very accurate but it is computationally demanding in terms of memory and CPU time requirements (each simulation takes a few hours), being unfeasible for computer-aided design based design approaches exploiting parametric investigation campaigns. To overcome the huge computational costs of FDTD, the modal-FDTD method is used which is much faster than FDTD (more than ten times), with the same accuracy.

For Mach-Zehnder modulators, a multiphysics method is provided which allows for eficient optimization of the geometry, without huge computational cost. For the directional coupler modulator, a new geometry is introduced. The modulator

can be optimized for different applications - this has been discussed focusing on representative symmetric and asymmetric devices. Asymmetry has been shown to affect the E/O response by a rigid shift on the V_{in} axis, thus allowing to have the half-power bias at V_{DC} = 0 V. Insertion loss is around 4 dB, the $V_{\pi} \cdot L$ product around 110 V$\cdot\mu$m, the extinction ratio is in excess of 25 dB, the intrinsic modulation bandwidth is in the THz range, with an energy consumption of the order of 20 fJ/bit and optical bandwidth in excess of 100 nm, comparable with the one of Mach-Zehnder modulators.

In summary, the performance of directional coupler modulators in terms of area, plasmonic losses, optical bandwidth, intrinsic modulation bandwidth and energy dissipation are comparable to already proposed Mach-Zehnder solutions. Yet, the present analysis suggests that directional coupler modulator may have some advantages with respect to Mach-Zehnder modulators. First, because a single slot has to be excited, the launching scheme is simpler, mitigating the photonic-plasmonic conversion losses, that we demonstrate being around 1 dB in the ON state. Secondly, in directional coupler modulators, reducing the lateral extent of the device (and hence its footprint and capacitance) does not introduce any extinction ratio penalty. Also, the insertion loss is lower in directional coupler modulator since some part of power transfer to adjacent waveguide instead of dissipating in the middle island of Mach-Zehnder modulator.

The focus of this Dissertation has been placed on the physics-based modeling of standalone devices. Having at our disposal mature device-level models capable of reproducing experimental results, a possible follow-up of this Ph.D. program could be assessing the impact of novel devices within system-level simulations on the entire optical telecommunication chain (Tx/fiber/Rx). To this aim, rather than inserting directly physics-based models in the simulation flow, a possible alternative could be to use behavioural models based, *e.g.,* on neural networks trained by the models developed within this Thesis.

References

[1] Bahaa E. A. Saleh and Malvin Carl Teich. *Fundamentals of Photonics*. 2007.

[2] P. A. Franken, A. E. Hill, C. W. Peters, and G. Weinreich. Generation of optical harmonics. *Physical Review Letters*, 7(4):118–119, 8 1961.

[3] Richard A. Soref and Brian R. Bennett. Kramers-kronig analysis of electro-optical switching in silicon. Cambridge Symposium-Fiber/LASE '86, SPIE, 3 1987.

[4] D. A. B. Miller, D. S. Chemla, and S. Schmitt-Rink. Relation between electroabsorption in bulk semiconductors and in quantum wells: The quantum-confined franz-keldysh effect. *Physical Review B*, 33(10):6976–6982, 5 1986.

[5] Tetsuya Takeuchi, Shigetoshi Sota, Maki Katsuragawa, Miho Komori, Hideo Takeuchi, Hiroshi Amano, and Isamu Akasaki. Quantum-confined stark effect due to piezoelectric fields in gainn strained quantum wells. *Japanese Journal of Applied Physics*, 36(Part 2, No. 4A):L382–L385, 4 1997.

[6] Ali W. Elshaari, Iman Esmaeil Zadeh, Klaus D. Jons, and Val Zwiller. Thermo-optic characterization of silicon nitride resonators for cryogenic photonic circuits. *IEEE Photonics Journal*, 8(3):1–9, 6 2016.

[7] Adil Masood, Marianna Pantouvaki, Guy Lepage, Peter Verheyen, Joris Van Campenhout, Philippe Absil, Dries Van Thourhout, and Wim Bogaerts. Comparison of heater architectures for thermal control of silicon photonic circuits. 2013 IEEE 10th International Conference on Group IV Photonics (GFP), IEEE, 8 2013.

[8] Guoliang Li, Xuezhe Zheng, Jin Yao, Hiren Thacker, Ivan Shubin, Ying Luo, Kannan Raj, John E. Cunningham, and Ashok V. Krishnamoorthy. 25gb/s 1v-driving cmos ring modulator with integrated thermal tuning. *Optics Express*, 19(21):20435, 10 2011.

[9] Lumerical Inc. *FDTD: 3D Electromagnetic Simulator*. 2019.

[10] Melissa Ziebell, Delphine Marris-Morini, Gilles Rasigade, Jean-Marc Fédéli, Paul Crozat, Eric Cassan, David Bouville, and Laurent Vivien. 40 gbit/s low-loss silicon optical modulator based on a pipin diode. *Optics Express*, 20(10):10591, 4 2012.

[11] Christian Haffner, Wolfgang Heni, Delwin L. Elder, Yuriy Fedoryshyn, Nikola Đorđević, Daniel Chelladurai, Ueli Koch, Kevin Portner, Maurizio Burla, Bruce Robinson, Larry R. Dalton, and Juerg Leuthold. Harnessing nonlinearities near material absorption resonances for reducing losses in plasmonic modulators (1). *Optical Materials Express*, 7(7):2168, 6 2017.

[12] C. Haffner, W. Heni, Y. Fedoryshyn, J. Niegemann, A. Melikyan, D. L. Elder, B. Baeuerle, Y. Salamin, A. Josten, U. Koch, C. Hoessbacher, F. Ducry, L. Juchli, A. Emboras, D. Hillerkuss, M. Kohl, L. R. Dalton, C. Hafner, and J. Leuthold. All-plasmonic mach–zehnder modulator enabling optical high-speed communication at the microscale. *Nature Photonics*, 9(8):525–528, 7 2015.

[13] Stefan Alexander Maier. *Plasmonics*. Springer London, Limited, 2007.

[14] Amnon Yariv. *Optical waves in crystals*. John Wiley and Sons, 2003.

[15] Mohammadamin Ghomashi, Hassan Kaatuzian, and Mohammad Danaie. Design and simulation of normally open and normally closed all-optical switches based on photonic crystal triple-waveguide directional coupler. *Optical and Quantum Electronics*, 48(1), 12.

[16] F. Bertazzi, O.A. Peverini, M. Goano, G. Ghione, R. Orta, and R. Tascone. A fast reduced-order model for the full-wave fem analysis of lossy inhomogeneous anisotropic waveguides. *IEEE Transactions on Microwave Theory and Techniques*, 50(9):2108–2114, 9 2002.

[17] Alberto Tibaldi, Mohammadamin Ghomashi, Francesco Bertazzi, Michele Goano, Marco Vallone, and Giovanni Ghione. Plasmonic-organic hybrid electro/optic mach-zehnder modulators: from waveguide to multiphysics modal-fdtd modeling. *Optics Express*, 28(20):29253, 9 2020.

[18] Renato Orta, Alberto Tibaldi, and Pierluigi Debernardi. Bimodal resonance phenomena—part i: Generalized fabry–pérot interferometers. *IEEE Journal of Quantum Electronics*, 52(12):1–8, 12 2016.

[19] Larry R. Dalton, Philip A. Sullivan, and Denise H. Bale. Electric field poled organic electro-optic materials: State of the art and future prospects. *Chemical Reviews*, 110(1):25–55, 10 2009.

[20] Delwin L. Elder, Stephanie J. Benight, Jinsheng Song, Bruce H. Robinson, and Larry R. Dalton. Matrix-assisted poling of monolithic bridge-disubstituted organic nlo chromophores. *Chemistry of Materials*, 26(2):872–874, 1 2014.

[21] Wolfgang Heni, Christian Haffner, Delwin L. Elder, Andreas F. Tillack, Yuriy Fedoryshyn, Raphael Cottier, Yannick Salamin, Claudia Hoessbacher, Ueli Koch, Bojun Cheng, Bruce Robinson, Larry R. Dalton, and Juerg Leuthold. Nonlinearities of organic electro-optic materials in nanoscale slots and implications for the optimum modulator design. *Optics Express*, 25(3):2627, 2 2017.

[22] C. Koos, J. Leuthold, W. Freude, M. Kohl, L. R. Dalton, W. Bogaerts, A.-L. Giesecke, M. Lauermann, A. Melikyan, S. Koeber, S. Wolf, C. Weimann, S. Muehlbrandt, K. Koehnle, J. Pfeifle, R. Palmer, D. Korn, L. Alloatti, D. L. Elder, T. Wahlbrink, and J. Bolten. Silicon-organic hybrid (soh) and plasmonic-organic hybrid (poh) integration. Optical Fiber Communication Conference, OSA, 2015.

[23] Wolfgang Heni, Yasar Kutuvantavida, Christian Haffner, Heiner Zwickel, Clemens Kieninger, Stefan Wolf, Matthias Lauermann, Yuriy Fedoryshyn, Andreas F. Tillack, Lewis E. Johnson, Delwin L. Elder, Bruce H. Robinson, Wolfgang Freude, Christian Koos, Juerg Leuthold, and Larry R. Dalton. Silicon–organic and plasmonic–organic hybrid photonics. *ACS Photonics*, 4(7):1576–1590, 2017.

[24] Wenshan Cai, Justin S. White, and Mark L. Brongersma. Compact, high-speed and power-efficient electrooptic plasmonic modulators. *Nano Letters*, 9(12):4403–4411, 10 2009.

[25] Sebastian Koeber, Robert Palmer, Matthias Lauermann, Wolfgang Heni, Delwin L Elder, Dietmar Korn, Markus Woessner, Luca Alloatti, Swen Koenig, Philipp C Schindler, Hui Yu, Wim Bogaerts, Larry R Dalton, Wolfgang Freude, Juerg Leuthold, and Christian Koos. Femtojoule electro-optic modulation using a silicon–organic hybrid device (1). *Light: Science Applications*, 4(2):e255–e255, 2 2015.

[26] Fariborz Mirlou and Hadi Soofi. Hybrid plasmonic–photonic–organic modulators with low insertion loss and high modulation depth. *Journal of Lightwave Technology*, 36(12):2471–2477, 6 2018.

[27] Alexandros Emboras, Claudia Hoessbacher, Christian Haffner, Wolfgang Heni, Ueli Koch, Ping Ma, Yuriy Fedoryshyn, Jens Niegemann, Christian Hafner, and Jurg Leuthold. Electrically controlled plasmonic switches and modulators. *IEEE Journal of Selected Topics in Quantum Electronics*, 21(4):276–283, 7 2015.

[28] Giovanni Ghione. Semiconductor devices for high-speed optoelectronics. 10 2009.

[29] Bartos Chmielak, Michael Waldow, Christopher Matheisen, Christian Ripperda, Jens Bolten, Thorsten Wahlbrink, Michael Nagel, Florian Merget, and Heinrich Kurz. Pockels effect based fully integrated, strained silicon electro-optic modulator. *Optics Express*, 19(18):17212, 8 2011.

[30] Long Chen, Christopher R. Doerr, Po Dong, and Young-kai Chen. Monolithic silicon chip with 10 modulator channels at 25 gbps and 100-ghz spacing. European Conference and Exposition on Optical Communications, OSA, 2011.

[31] Po Dong, Long Chen, and Young-kai Chen. High-speed low-voltage single-drive push-pull silicon mach-zehnder modulators. *Optics Express*, 20(6):6163, 2 2012.

[32] Sergey I. Bozhevolnyi. Effective-index modeling of channel plasmon polaritons. *Optics Express*, 14(20):9467, 2006.

[33] Pavel Ginzburg and Meir Orenstein. Plasmonic transmission lines: from micro to nano scale with /4 impedance matching. *Optics Express*, 15(11):6762, 2007.

[34] Hamid Nejati and Ahmad Beirami. Theoretical analysis of the characteristic impedance in metal–insulator–metal plasmonic transmission lines. *Optics Letters*, 37(6):1050, 3 2012.

[35] Liu Liu, Zhanghua Han, and Sailing He. Novel surface plasmon waveguide for high integration. *Optics Express*, 13(17):6645, 2005.

[36] Georgios Veronis and Shanhui Fan. Modes of subwavelength plasmonic slot waveguides. *Journal of Lightwave Technology*, 25(9):2511–2521, 9 2007.

[37] Youqiao Ma, Jinhua Li, and Hiroshi Maeda. Polarization-independent hybrid plasmonic coupler based on t-shaped slot waveguide. *AIP Advances*, 10(3):035121, 3 2020.

[38] Alireza Taghizadeh and Thomas Garm Pedersen. Plasmons in ultra-thin gold slabs with quantum spill-out: Fourier modal method, perturbative approach, and analytical model. *Optics Express*, 27(25):36941, 12 2019.

[39] Alireza Taghizadeh and Thomas Garm Pedersen. Plasmons in ultra-thin gold slabs with quantum spill-out: Fourier modal method, perturbative approach, and analytical model. *Optics Express*, 27(25):36941, 12 2019.

[40] Sophocles J. Orfanidis. *Electromagnetic waves and antennas*. 2016.

[41] Christian Haffner, Wolfgang Heni, Yuriy Fedoryshyn, Arne Josten, Benedikt Baeuerle, Claudia Hoessbacher, Yannick Salamin, Ueli Koch, Nikola Dordevic, Pol Mousel, Romain Bonjour, Alexandros Emboras, David Hillerkuss, Pascal Leuchtmann, Delwin L. Elder, Larry R. Dalton, Christian Hafner, and Juerg Leuthold. Plasmonic organic hybrid modulators—scaling highest speed photonics to the microscale. *Proceedings of the IEEE*, 104(12):2362–2379, 12 2016.

[42] F. Bertazzi, G. Ghione, and M. Goano. Efficient quasi-tem frequency-dependent analysis of lossy multiconductor lines through a fast reduced-order fem model. *IEEE Transactions on Microwave Theory and Techniques*, 51(9):2029–2035, 9 2003.

[43] H. Kogelnik and C. V. Shank. Coupled-wave theory of distributed feedback lasers. *Journal of Applied Physics*, 43(5):2327–2335, 5 1972.

[44] Wei-Ping Huang. Coupled-mode theory for optical waveguides: an overview. *Journal of the Optical Society of America A*, 11(3):963, 3 1994.

[45] Segolene Olivier, H. Benisty, C. Weisbuch, C. Smith, T. Krauss, and R. Houdre. Coupled-mode theory and propagation losses in photonic crystal waveguides. *Optics Express*, 11(13):1490, 6 2003.

[46] Connie J. Chang-Hasnain and Weijian Yang. High-contrast gratings for integrated optoelectronics. *Advances in Optics and Photonics*, 4(3):379, 9 2012.

[47] Renato Orta, Alberto Tibaldi, and Pierluigi Debernardi. Bimodal resonance phenomena—part ii: High/low-contrast grating resonators. *IEEE Journal of Quantum Electronics*, 52(12):1–8, 12 2016.

[48] Alberto Tibaldi, Pierluigi Debernardi, and Renato Orta. Bimodal resonance phenomena—part iii: High-contrast grating reflectors. *IEEE Journal of Quantum Electronics*, 54(6):1–8, 12 2018.

[49] W. Shan, W. Walukiewicz, J. W. Ager, E. E. Haller, J. F. Geisz, D. J. Friedman, J. M. Olson, and S. R. Kurtz. Band anticrossing in gainnas alloys. *Physical Review Letters*, 82(6):1221–1224, 2 1999.

[50] Jean G. Van Bladel. *Singular Electromagnetic Fields and Sources*. IEEE, 1996.

[51] J. Meixner. The behavior of electromagnetic fields at edges. *IEEE Transactions on Antennas and Propagation*, 20(4):442–446, 7 1972.

[52] Enrico Gregorio. Installing tex live 2010 on ubuntu. *TUGboat*, 32(1):56–61, 2011.

[53] Alberto Tibaldi, Pierluigi Debernardi, and Renato Orta. High-contrast gratings performance issues in tunable vcsels. *IEEE Journal of Quantum Electronics*, 51(12):1–7, 12 2015.

[54] R. Mittra, Y. Hou, and V. Jamnejad. Analysis of open dielectric waveguides using mode-matching technique and variational methods. 3 1979.

[55] W. Heni, C. Haffner, B. Baeuerle, Y. Fedoryshyn, A. Josten, D. Hillerkuss, J. Niegemann, A. Melikyan, M. Kohl, D. L. Elder, L. R. Dalton, C. Hafner, and J. Leuthold. 108 gbit/s plasmonic mach–zehnder modulator with > 70-ghz electrical bandwidth. *Journal of Lightwave Technology*, 34(2):393–400, 1 2016.

[56] Mohammadamin Ghomashi, Alberto Tibaldi, Francesco Bertazzi, Marco Vallone, Michele Goano, and Giovanni Ghione. Simulation of electro optic modulators based on plasmonic directional couplers. *2020 International Conference on Numerical Simulation of Optoelectronic Devices (NUSOD)*, 9 2020.

[57] Kunio TADA and Keikichi HIROSE. A new light modulator using perturbation of synchronism between two coupled guides. *Extended Abstracts of the 1974 Conference on Solid State Devices*, 1974.

[58] J. C. Campbell, F. A. Blum, D. W. Shaw, and K. L. Lawley. Gaas electro-optic directional-coupler switch. *Applied Physics Letters*, 27(4):202–205, 8 1975.

[59] M. Papuchon, Y. Combemale, X. Mathieu, D. Ostrowsky, L. Reiber, A. Roy, B. Sejourne, and M. Werner. Electrically switched optical directional coupler: Cobra. *IEEE Journal of Quantum Electronics*, 11(9):921–922, 9 1975.

[60] R. C. Alferness, C. H. Joyner, and L. L. Buhl. High-speed traveling-wave directional coupler modulator for $\lambda = 1.32$ m. *Optical Fiber Communication*, 1983.

[61] F. Koyama and K. Oga. Frequency chirping in external modulators. *Journal of Lightwave Technology*, 6(1):87–93, 1988.

[62] Melikyan, A and Alloatti, L and Muslija, A and Hillerkuss, D and Schindler, PC and Li, J and Palmer, R and Korn, D and Muehlbrandt, S and Van Thourhout, Dries and Chen, B and Dinu, R and Sommer, M and Koos, C and Kohl, M and Freude, W and Leuthold, J. High-speed plasmonic phase modulators. *NATURE PHOTONICS*, 8(3):229–233, 2014.

[63] M. Y. Abdelatty, A. O. Zaki, and M. A. Swillam. Hybrid silicon plasmonic organic directional coupler-based modulator. *Applied Physics A*, 123(1), 12 2016.

[64] Raymond A. Serway and John W. Jewett. *Principles of Physics*. Brooks/Cole Publishing Company, 3 2012.

[65] MATLAB version 9.11.0.1837725 (R2021b) Update 2. 2021.

[66] David A. B. Miller. Energy consumption in optical modulators for interconnects. *Optics Express*, 20(S2):A293, 3 2012.

Appendix A

Material parameters

This appendix provides details about the material parameter used in this work. The refractive indexes adopted in the simulations, mostly coming from typical literature values, are listed in Table A.1. In particular, Au in the electrical simulation is treated as an impedance boundary condition, with conductivity $\sigma = 4.1 \times 10^7$ S/m. Even though not visible in Fig. 3.1(right), the Si substrate has been included in the electrical simulations. The complex dielectric constant used for Au has been taken from [12], valid at $\lambda = 1.55\,\mu$. Also the DLD-164 polymer optical refractive index has been taken from the same reference. However, to the best of our knowledge no information is provided about its radiofrequency response (all the details we have found come from [21, Fig. 4]), so we assumed $n_{\mathrm{NLO}} = 1.83$, with no dielectric losses, also in the quasi-static RF problem.

Table A.1 Refractive indexes used in the simulations.

Material	$n_{\mathrm{electrical}}$	n_{optical}
Au	–	$0.2524 - \mathrm{j}10.4386$
Si	3.42	3.5
SiO_2	1.97	1.44
DLD-164	1.83	1.83

Appendix B

Voltage-dependent change of basis

The approach described in this appendix could be seen as a mode-matching technique, where only two modes are used to represent the transverse field at the discontinuity. In other words, the modes of a waveguide subjected to E/O effect, $|V_1\rangle$, $|V_2\rangle$, are expressed as a linear combination of the zero-voltage modes $|Z_1\rangle$, $|Z_2\rangle$ (the situation at which the splitter 3D-FDTD is simulated):

$$\begin{aligned} |V_1\rangle &= W_{11}\,|Z_1\rangle + W_{12}\,|Z_2\rangle \\ |V_2\rangle &= W_{21}\,|Z_1\rangle + W_{22}\,|Z_2\rangle\,. \end{aligned} \tag{B.1}$$

Because this equation involves four coefficients W_{ij}, their determination requires formulating a 4×4 linear system, which is obtained projecting these two equations on two functions. In standard mode-matching techniques great attention is put on the projectors' definitions. In this case, being the system quite small, it is sufficient that the projecting modes are independent. For this reason, the equations are projected on $\langle Z_1|$ and $\langle Z_2|$, leading to:

$$\begin{aligned} \langle Z_1|V_1\rangle &= W_{11}\,\langle Z_1|Z_1\rangle + W_{12}\,\langle Z_1|Z_2\rangle \\ \langle Z_2|V_1\rangle &= W_{11}\,\langle Z_2|Z_1\rangle + W_{12}\,\langle Z_2|Z_2\rangle \\ \langle Z_1|V_2\rangle &= W_{21}\,\langle Z_1|Z_1\rangle + W_{22}\,\langle Z_1|Z_2\rangle \\ \langle Z_2|V_2\rangle &= W_{21}\,\langle Z_2|Z_1\rangle + W_{22}\,\langle Z_2|Z_2\rangle \end{aligned}, \tag{B.2}$$

where the bra-ket notation indicates the dot product:

$$\langle A|B\rangle = \int_S \mathbf{A}_\mathrm{t} \cdot \mathbf{B}_\mathrm{t}^* \, \mathrm{d}\sigma,$$

where, as in the standard mode-matching, S is the (x,y) cross-section of the waveguide discontinuity, the star superscript indicates complex conjugation, and $\mathbf{A}_\mathrm{t}$, $\mathbf{B}_\mathrm{t}$ are the transverse fields, which must be continuous to satisfy the boundary conditions of Maxwell's equations.

It can be noticed that the first and last groups of two equations are independent, leading to two uncoupled linear systems:

$$\begin{bmatrix} \langle Z_1|Z_1\rangle & \langle Z_1|Z_2\rangle \\ \langle Z_2|Z_1\rangle & \langle Z_2|Z_2\rangle \end{bmatrix} \begin{bmatrix} W_{11} \\ W_{12} \end{bmatrix} = \begin{bmatrix} \langle Z_1|V_1\rangle \\ \langle Z_2|V_1\rangle \end{bmatrix}, \tag{B.3}$$

$$\begin{bmatrix} \langle Z_1|Z_1\rangle & \langle Z_1|Z_2\rangle \\ \langle Z_2|Z_1\rangle & \langle Z_2|Z_2\rangle \end{bmatrix} \begin{bmatrix} W_{21} \\ W_{22} \end{bmatrix} = \begin{bmatrix} \langle Z_1|V_2\rangle \\ \langle Z_2|V_2\rangle \end{bmatrix}. \tag{B.4}$$

The solutions of the systems (B.3), (B.4) are the elements of the matrix $\mathbf{W}$ in (3.5).

Appendix C

Evaluation of the field expansion coefficients

The purpose of this Appendix is to provide additional details on the numerical approach summarized by (4.2)–(4.4). The first step regards the evaluation of the coefficients $c_i^{(\mathrm{I})}$. These coefficients are obtained by projecting (4.2) on the voltage-dependent mode profiles $|V_i\rangle$. This leads to the following system of equations:

$$\underbrace{\begin{bmatrix} \langle V_1|V_1\rangle & \langle V_1|V_2\rangle \\ \langle V_2|V_1\rangle & \langle V_2|V_2\rangle \end{bmatrix}}_{\underline{\underline{A}}^{(\mathrm{I})}} \underbrace{\begin{bmatrix} c_1^{(\mathrm{I})} \\ c_2^{(\mathrm{I})} \end{bmatrix}}_{\underline{c}^{(\mathrm{I})}} = \underbrace{\begin{bmatrix} \langle V_1|I\rangle \\ \langle V_2|I\rangle \end{bmatrix}}_{\underline{b}^{(\mathrm{I})}} \tag{C.1}$$

where projections are based on the bra-ket product $\langle V_j|V_i\rangle$ defined as

$$\langle V_j|V_i\rangle = \iint \underline{E}_j^*(V_{\mathrm{in}}) \cdot \underline{E}_i(V_{\mathrm{in}})\,\mathrm{d}x\,\mathrm{d}y, \tag{C.2}$$

and the scalar product (performed over the cross-section simulated with the FEM mode solver) involves the transverse (x and y) components of the electric field. The evaluation of the right-hand side is similar, but it involves the projection of the input field $|I\rangle$, which is voltage-independent. Representing the input field as a linear combination of the voltage-dependent modes is advantageous because it allows to evaluate the output field $|O\rangle$, for each V_{in}, by propagating these coefficients with propagation constants evaluated with the voltage-dependent effective refractive indices, with (4.3). Assuming that the output field has the same profile of the

excitation field, which is the case of both MZ (even mode) and PDC (I/O waveguide mode) modulators, the modulator EO response is evaluated as the fraction of $|I\rangle$ in $|O\rangle$, *i.e.,* the coefficient $c_2^{(\mathrm{O})}$ in (4.4). These coefficients can be estimated with a procedure similar to that of (C.1), *i.e.,* by projecting the output field on the fields $|I\rangle$ and $|C\rangle$, leading to the system:

$$\underbrace{\begin{bmatrix} \langle I|I\rangle & \langle I|C\rangle \\ \langle C|I\rangle & \langle C|C\rangle \end{bmatrix}}_{\underline{\underline{A}}^{(\mathrm{I})}} \underbrace{\begin{bmatrix} c_1^{(\mathrm{O})} \\ c_2^{(\mathrm{O})} \end{bmatrix}}_{\underline{c}^{(\mathrm{O})}} = \underbrace{\begin{bmatrix} \langle I|O\rangle \\ \langle C|O\rangle \end{bmatrix}}_{\underline{b}^{(\mathrm{O})}} \tag{C.3}$$

from whose solution $c_1^{(\mathrm{O})}$ and $c_2^{(\mathrm{O})}$ are obtained.